Field induced assembly of paramagnetic colloidal particles

Colin P. Reynolds

Lincoln College
University of Oxford

Supervisors: Roel P. A. Dullens and Dirk G. A. L. Aarts

A thesis submitted for the degree of
Doctor of Philosophy

Trinity 2016

Abstract

The assembly of paramagnetic colloidal particles in the presence of an external magnetic field is studied with optical video microscopy. The first half of this thesis concerns chain formation, which occurs at relatively low surface coverages, and the second half concerns network formation, happening at relatively high surface coverages. First, we study the irreversible aggregation kinetics of two-dimensional paramagnetic colloidal particles in the presence of an in-plane magnetic field at low packing fractions. In particular, we study the packing fraction and field dependence of the mean cluster size. We compare experimental results to the predicted scalings for diffusion limited and deterministic aggregation respectively. It is shown that the aggregation kinetics for our experimental system is consistent with a deterministic mechanism. Next, we establish a direct relation between the distribution of coordination numbers of particles and the mean cluster size using simple statistical considerations. Empirically, a shifted geometric distribution of cluster sizes is observed, consistent with a discrete compound Poisson growth process. This is corroborated by simulations in which the initial spatial distribution of particles is controlled. The generality of our approach is demonstrated by applying it to a more complex clustering processes in two dimensions. Then we investigate the structural properties of magnetorheological networks. The size distributions, orientational ordering and spatial distribution of voids is investigated and compared to random fiber theory. In the fiber phase, the segment length distribution is characterised, as well as the distributions of fiber widths and orientations. These network properties are interrelated such that the entire growth process of fibrous networks can be summarised in terms of a single length scale. We follow this length scale in time for a range of fields and concentrations, investigating the dynamics of the network coarsening. Finally, we propose a link between random fiber theory and the coordination number statistics of particles that make up the network. We show that the fraction of particles with a coordination number less than 6 is key in quantitatively predicting the area of voids. Additionally, we show that clusters of 2 and 4 coordinate particles correspond to segments of the network, 6 coordinate particles represent a population of filled voids, and that singly coordinated particles are a sensitive diagnostic tool to probe the initial aggregation mechanism.

Declaration

This thesis is submitted for the degree of Doctor of Philosophy in Physical and Theoretical Chemistry at the University of Oxford. No part of this thesis has been accepted or is currently being submitted for any degree, diploma, certificate or other qualification in this University or elsewhere. This thesis is wholly my own work, except where indicated.

Contents

Chapter 1

Introduction

People have known about naturally occurring magnets for millennia, although the science that underpins them was not known until much more recently. References to lodestones, pieces of magnetite which have a magnetic moment, date back to as early as 800 BC in Greek writing [1]. Lodestone literally means "way-stone" and they have been used to magnetise sailor's compass needles for over a thousand years aiding the exploration of continents and the expansion of human understanding.

Until the work of Gilbert in the 1600s, superstition dominated with regard to lodestones and magnetism [2]. Since then the understanding of magnetism has advanced greatly with the work of many great and famous scientists. Our knowledge of the origins of naturally occurring magnets has also advanced greatly. For a magnetic moment to be fixed into the iron ore as it is formed, there needs to be an external magnetic field to align the domains of magnetite [3]. As a result of this response to the external field in which the rock is formed, records of the history of earths magnetic field are stored in the lava flows around fault lines. As, over hundreds of thousands of years, the earth's magnetic field varies in strength and polarity, so too does the magnetic moment of the rock that is being formed [3]. The strongest lodestones, however, require a stronger magnetic field stronger than that the earths to form and it is believed that these are formed by the intense magnetic field around lightning strikes [4].

Nature provides another source of magnetite through bacteria that anaerobically consume non magnetic ferric oxide to produce crystals of magnetite with sizes in the range of 10 nm to 50 nm [5]. Another class of bacteria, magnetotactic bacteria, incorporating chains of magnetite

particles travel along field lines as a strategy for finding sediments suitable for their growth [6]. Superparamagnetic magnetite particles, as well as single domain magnetite, have been found in many other animals including the nerve cells and beaks of birds, possibly for the purpose of magnetoreception [7], although this remains an open question. We find then that physics and biology developed tuneable self-assembly and found applications for it long before humans.

The central importance of magnetism to technological and scientific advancement is now a long standing tradition [8]. Magnetism is so fundamentally entwined with technology that it is almost impossible to conceive of a modern society that does not have it at its core. Even today the development of new technologies based on this age old phenomena are being developed. For example modern MRI scanners [9], Maglev trains [10], and fusion reactors [11] all rely very directly on the property of magnetism.

1.1 Field induced assembly

The magnetisation of iron ore, discussed above, is a simple naturally occurring example of self-assembly. Self-assembly is an umbrella term for how components build and arrange into more complex structures, of which the most famous example is probably the DNA double helix [12]. There is an extensive field of research in trying to mimic or utilize the design principles employed by nature to create complex materials [13]. One particular strategy towards a general self-assembly is that of directed self-assembly in which components are guided by an external impetus such as patterned substrates [14], temperature gradients [15] or external magnetic or electric fields [16].

In particular, externally imposed magnetic fields and electric fields have long been known to induce structural changes in suspensions of colloidal particles [17–20]. For magnetically responsive systems in particular there have been several experimental realizations, including magnetic holes in ferro-fluid carriers [20] and magnetic particles in aqueous solvents [21, 22]. This structure formation can produce large changes in the physical and optical properties of the magnetorheological fluid [23, 24]. Practical applications include civil engineering solutions for seismic shock absorbers and bridge stabilizers, advanced prosthetics, and in the auto-motives industry [25–27].

The formation of chains, clusters and networks is responsible for the observed changes in physical parameters [24]. The precise mechanism of structure formation affects the magnitude of the response and the dynamics, which in turn affect the response profile of a device based on these materials [28]. In the presence of a static field, at low concentration, chains of particles are observed and grow continuously in time [21, 22]. Or, if the applied magnetic field is weaker, chains may reach an equilibrium length [29]. In the presence of rotating magnetic fields, at low concentrations, islands of particles are observed [30,31]. If the particles are at a fluid interface, in the presence of time dependent magnetic fields, induced flows lead to many dynamic structures such as snakes and asters [32].

At high concentrations, system spanning networks of particles are formed in both electrorheological and magnetorheological systems [33, 34]. This network structure is a kinetically arrested state, the thermodynamic state can only be accessed with pulsed fields that allow the structure to rearrange into the minimum energy structure [35–39]. Other time dependent fields lead to a range of other structures including foams and other cellular structures [32]. Fibrous networks are of great general importance in their own right and have found myriad applications in filtration, composite materials, catalysis and in biomedical applications [40–45]. Fibrous networks made of magnetic particles, therefore, potentially share many of these applications.

1.2 Colloidal systems

Magnetorheological suspensions are, by their very nature, colloidal suspensions. Colloids are often defined as suspensions of particles with at least on lengthscale in the range of 10 nm to 10 μm [46]. At this scale, colloidal particles are small enough that the perpetual bombardment by solvent molecules causes them to exhibit Brownian motion. This thermal agitation causes them to mimic atomic systems in many respects [47]. For example, colloidal spheres exhibit phase behaviour analogous to atomic systems [48]. One of the key advantages of colloids is the bridging of length scales. On the one hand colloids are small enough to be subjected to thermal motion, while on the other hand they are large enough that they interact with visible light, making them apt for studying with optical microscopy techniques.

Colloidal particles exist in many myriad shapes beyond simple spheres [49] including dumbells [50], cubes [51], rods [52], lock and keys [53], polyhedra [54], and even Mickey Mouse

shaped [55]. Often particles are made of more that one type of material leading to a two faced nature, janus particles [56]. In a similar vain portions of the surfaces of particles are often modified to induce directional interactions between particles [57]. In addition to interactions inherent to a particle's geometry, the interaction may be tuned by controlling the salt concentration, modifying the electrostatics, or by the introduction polymer, inducing depletion interaction [58]. In addition, induced interactions such as control by external fields [59] are a powerful means of directing self-assembly.

Due to the range of different interactions and competing driving forces, controlling self-assembly remains a formidable challenge [60–64]. Colloids, however, are an excellent experimental model system used to address this. The development of useful materials and tunable devices requires a deep understanding of the fundamental structural and dynamical processes that lead to self-assembly. The coordination number of a constituent entity is a central quantity in self-assembling systems as this characterises the local structure around that entity [65–71]. Indeed, the geometry of molecules and hence their directional interactions result in highly specific self-assembled structures [72].

1.3 Scope of the thesis

In this thesis, we aim to use a model colloidal system of paramagnetic particles to investigate two dimensional structure formation, and in particular network formation, in the presence of an in-plane external magnetic field. The field-induced assembly of paramagnetic particles is studied with optical video microscopy. The first half of this thesis concerns chain formation, which occurs at relatively low surface coverages. The second half concerns network formation, which occurs at relatively high surface coverages. Chapters 3 and 5 concern structures created by many particles, respectively these properties are cluster sizes and network properties such as void area and segment length. Chapters 4 and 6 link the microscopic property of particle coordination numbers to the larger scale structures presented in chapters 3 and 5.

First, we introduce colloids as model systems, outlining their characteristic properties and interactions. The interactions of pairs of magnetic dipoles and the interaction of chains of magnetic dipoles are introduced. Then we show how quantitative measurements are acquired from our experimental system by coupling optical video microscopy with novel image and data

analysis techniques.

In chapter 3, we study the irreversible aggregation kinetics of two-dimensional paramagnetic colloidal particles in the presence of an in-plane magnetic field at low packing fractions. In particular, we study the packing fraction and field dependence of the mean cluster size and compare experimental results to the predicted scalings for diffusion limited and deterministic aggregation. It is shown that the aggregation kinetics for our experimental system is consistent with a deterministic mechanism, which thus shows that the contribution of diffusion is negligible.

In chapter 4, we establish a direct relation between the distribution of coordination numbers of particles and the mean cluster size using simple statistical considerations. Empirically, a shifted geometric distribution of cluster sizes is observed, consistent with a discrete compound Poisson growth process. To corroborate the compound Poisson nature of this process, experimental results are compared to simulations in which the initial spatial distribution of particles is controlled. The generality of our approach is demonstrated using another clustering processes in two dimensions as a model system.

In chapter 5, we investigate the structural properties of magnetorheological networks. The size distributions, orientational ordering and spatial distribution of the void phase is investigated and compared to random fiber theory. In the fiber phase, the segment length distribution is characterised, as well as the distributions of fiber widths and orientations. These network properties are interrelated such that the entire growth process of fibrous networks can be summarised in terms of a single length scale. We follow this length scale in time for a range of fields and concentrations, investigating the dynamics of the network coarsening and its dependence on magnetic field strength and surface coverage.

Finally, we propose a link between random fiber theory and the coordination number statistics of particles that make up a magnetorheological network. We show that the fraction of particles in the network with a coordination number less than 6 is key in quantitatively predicting the area of voids. Also, we show that clusters of 2 and 4 coordinate particles correspond to segments in a random fiber interpretation of the network, while clusters of 6 coordinate particles represent a population of filled voids. Additionally, we show that singly coordinated particles are a sensitive diagnostic tool to probe the initial aggregation mechanism.

Chapter 2

Background and experimental methods

ABSTRACT

In this chapter we introduce colloids as model systems, outlining the characteristic properties and interactions. We detail the interactions of pairs of magnetic dipoles and the interaction of chains of magnetic dipoles. Finally, we show how quantitative measurements are acquired from our experimental system by coupling optical video microscopy with novel image and data analysis techniques.

2.1 Colloidal regime - length scales and time scales

Colloids were defined in the introduction as particles with a length scale in the range of nanometers to micrometers [46]. We will first consider some of the implications of this on the typical timescales in colloidal systems. After that the typical interactions of colloids are introduced.

Colloidal particles are small enough that the constant bombardment of a particle by solvent molecules leads to Brownian motion [73]. This causes particles to diffuse with a random walk. The mean squared displacement of a particle in two dimensions, in the limit of infinite dilution,

is [74]

$$\langle r^2 \rangle = \frac{4k_B T t}{\zeta} = 4Dt, \tag{2.1}$$

where r is the displacement, k_B the Boltzmann constant, T the temperature, t the time, ζ the drag coefficient, and D the diffusion coefficient.

The Brownian time, t_B, is defined as the time it takes for a particle to diffuse over a distance equal to its diameter and is given by [75]

$$t_B = \frac{a^2}{D} = \frac{6\pi\eta a^3}{k_\mathrm{B} T}, \tag{2.2}$$

where a is the particle radius and η is the solvent's viscosity. For a colloidal particle with a radius of 1 µm, suspended in water, t_B is on the order of seconds.

In colloidal systems, thermal energy and gravitational potential energy are in constant competition. This balance is quantified by the gravitation height, h_g, which is the height that one $k_B T$ worth of energy can raise a particle. It is given by [75]

$$h_g = \frac{3k_\mathrm{B} T}{4\pi a^3 \Delta\rho g}, \tag{2.3}$$

where $\Delta\rho$ is the mass density difference between the solvent and the particle, and g the acceleration due to gravity. When $h_g \ll 2a$ the particles will be confined to a plane at the bottom surface of the sample cell they are contained in.

2.2 Interactions of colloidal particles

2.2.1 DLVO

The interactions between charge stabilised colloidal particles is described by the DLVO (Derjaguin, Landau, Verwey and Overbeek) theory [76, 77]. The DLVO potential is the sum of the van der Waals potential and the electrostatic repulsion,

$$U_{\mathbf{DLVO}} = U_{vdW} + U_e. \tag{2.4}$$

For colloidal particles, van der Waals forces are always present independent of the material they are made of. The van der Waals interaction between two spherical particles of the same radius is given by [78]:

$$U_{vdW} = -\frac{Aa}{12r}, \tag{2.5}$$

where A is the Hamaker constant.

Typically, colloidal particles in suspension have a charged surface, either from the dissociation of surface groups or the adsorption of ions in suspension. A cloud of counter ions exists around a charged colloidal particle, the double layer, which leads to a repulsion of the form [79]:

$$U_e = Z^2 k_B T \lambda_B \left(\frac{e^{\kappa a}}{1+\kappa a}\right)^2 \frac{e^{-r\kappa}}{r}. \tag{2.6}$$

Here, Z is the charge number of the sphere, κ^{-1} the Debye length, and λ_B is the Bjerrum length, the separation at which the interaction of unit charges is equal to $k_B T$.

Because of the short lengthscale of the double layer compared to the particle diameters used in this thesis the superparamagnetic particles are considered to be impenetrable and, in the absence of an external magnetic field, are modeled as hard spheres [58]:

$$U_{\mathbf{HS}} = \begin{cases} \infty & r < 2a, \\ 0 & r \geq 2a. \end{cases} \tag{2.7}$$

2.2.2 Paramagnetic particles

We use paramagnetic particles as a model system to investigate field-induced assembly in dipolar systems. In addition to the typical colloidal interactions, which are discussed briefly above, paramagnetic particles acquire a dipole moment in the presence of an external magnetic field. This is due to the alignment of superparamagnetic nano-domains, typically with radii $r < 50nm$, embedded in a non-magnetic material that make up the bulk of the particle. It is these nano-domains that render the particle as a whole paramagnetic. The interaction of the induced dipoles of the particles drives their self-assembly in an external magnetic field. We will develop the equations for how collections of particles interact under the action of a magnetic field from

the equation of a point dipole.

Isolated dipolar particles

The equation for the magnetic field surrounding a dipole is given by [80]

$$\vec{B}(\vec{r}) = \frac{\mu_0}{4\pi}\left(\frac{3\vec{r}(\vec{m}\cdot\vec{r})}{r^5} - \frac{\vec{m}}{r^3}\right), \tag{2.8}$$

where $\vec{m}$ is the dipole moment, $\vec{r}$ is the vector from the dipole to the point of interest, $\vec{B}$ is the magnetic vector field, and μ_0 is the vacuum permeability. Particles acquire a dipole moment, in line with the external magnetic field, according to the Langevin magnetisation equation [81]:

$$\frac{m(B)}{m_0} = \coth(\alpha B) - 1/\alpha B. \tag{2.9}$$

Here, $m(B)$ is the magnetic moment, m_0 is the saturation moment, and α is a fitting parameter. We find by Taylor expansion that in the limit of small fields this function is linear and the magnetic moment may be written as

$$\vec{m}(\vec{B}) = \frac{m_0\alpha\vec{B}}{3} = \frac{v_p\chi_v\vec{B}}{\mu_0}. \tag{2.10}$$

Here, χ_v is the dimensionless volume susceptibility and is given by $\chi_v = (\mu_0 m_0 \alpha)/(3v_p)$, and v_p is the volume of a particle. The fields used in this thesis are within the regime of linear magnetization, as confirmed by SQUID (superconducting quantum interference device) magnetometry.

The interaction between two point dipoles

In our experiments the field experienced by a particle is dominated by the external field. The dipoles of particles align with the external field even in the presence of other particles. Consistent with this, we model the interactions of particles as the interactions of point dipoles aligned with the imposed magnetic field vector and neglect mutual induction effects. In this limiting case, the total interaction energy is the sum of all pairs of interactions considered in isolation, known as pairwise additivity. The interaction potential, U, of a dipole moment with a field is given

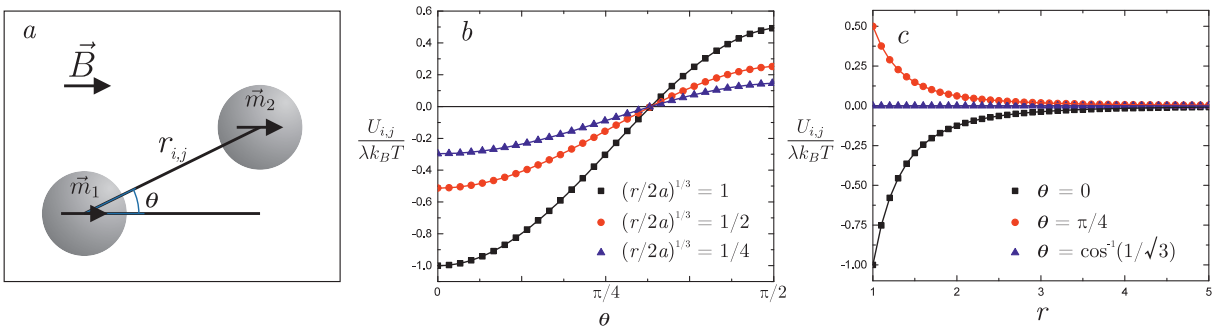

Figure 2.1: (a) A schematic of 2 particles, modeled as point dipoles, with the inter-particle vector, imposed magnetic field, dipole moments and the angle θ indicated. (b) A plot of the angle between particles, θ, against the interaction energy, $U_{i,j}/(\lambda k_B T)$, for 3 different separations (equation 2.14). All curves pass through 0 at $\theta = \cos^{-1}(1/\sqrt{3})$, the so called magic angle. (c) A plot of the separation of particles, $r/2a$, against interaction energy, $U_{i,j}/(\lambda k_B T)$, for 3 different angles (equation 2.14).

by [80]:

$$U = -\vec{B} \cdot \vec{m}. \tag{2.11}$$

From equations 2.8, 2.10 and 2.11, we can determine the interaction energy of two identical point dipoles, i and j, as

$$U_{ij} = \frac{\mu_0}{4\pi}\frac{m^2}{r^3}\left(1 - 3\cos^2\theta\right) = \frac{1}{4\pi\mu_0}\frac{v_p^2\chi_v^2 B^2}{r^3}\left(1 - 3\cos^2\theta\right). \tag{2.12}$$

Here, θ is the angle between the bond-vector connecting the particles i and j and the direction of the applied magnetic field, as shown in figure 2.1a. The interaction parameter, λ, is a dimensionless ratio of thermal energy, $k_B T$, and the interaction potential of two particles in contact and aligned with the external field. λ is given by [82]:

$$\lambda = -\frac{U_{i,j}(\theta = 0, r = 2a)}{k_B T} = \frac{\pi a^3 \chi_v^2 B^2}{9 k_{\mathrm{B}} T \mu_0}. \tag{2.13}$$

For $\lambda \gg 1$, the process of two particles coming together becomes essentially irreversible with thermal energy insufficient to break them apart [83]. We recast the interaction energy, equation 2.12, in terms of λ:

$$\frac{U_{i,j}}{k_B T} = \frac{\lambda}{2(r/2a)^3}(1 - 3\cos^2\theta). \tag{2.14}$$

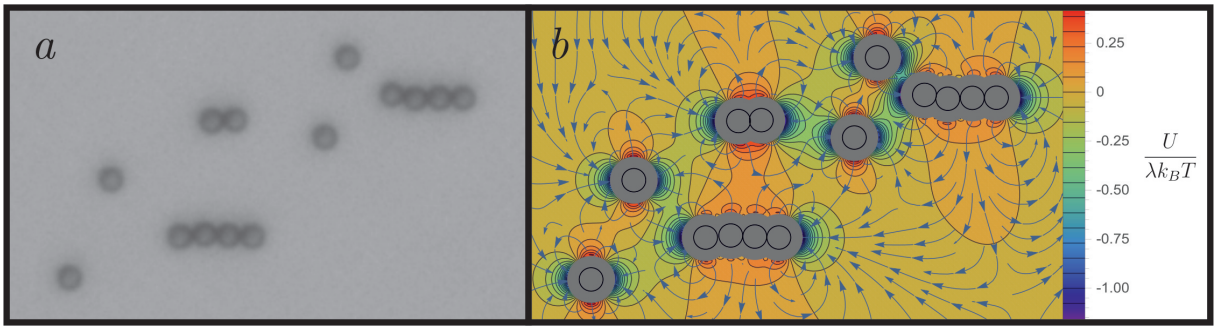

Figure 2.2: (a) A snapshot of magnetic particles aggregating. (b) A contour map of the interaction potential and a stream plot of the forces acting on particles. The grey regions indicate areas in which the centers of other particles are excluded due to hard sphere repulsions.

In figure 2.1*b* we plot $U_{i,j}/(\lambda k_B T)$ as a function of θ for three different separations. Independent of the separation the interaction energy passes through zero at $\theta = \cos^{-1}(1/\sqrt{3})$, the magic angle, which is where $U_{i,j}$ changes sign. This is also shown in figure 2.1*c* where we plot $U_{i,j}/(\lambda k_B T)$ as a function of $r/2a$ for 3 different angles: $\theta = 0$ (attractive), $\theta = \pi/2$ (repulsive), and $\theta = \cos^{-1}(1/\sqrt{3})$ (magic angle).

From equation 2.14, we can also derive an intrinsic length scale, R_1, which can be interpreted as a magnetic analogue of the Bjerrum length, $R_1 = 2a\lambda^{1/3}$. This length scale, R_1, is the maximum distance at which the interaction potential is equal to thermal energy [29].

In general, the force acting on a particle is the gradient of the potential energy landscape at that point. Thus from equation 2.12 it follows that the force acting on a particle in the presence of one other particles is:

$$F_{ij} = F_r\hat{r} + F_\theta\hat{\theta} = -\frac{\partial U_m}{\partial r}\hat{r} - \frac{1}{r}\frac{\partial U_m}{\partial \theta}\hat{\theta} = \frac{3\mu_0 m^2}{4\pi r^4}\left(\left(1 - 3\cos^2\theta\right)\hat{r} - \left(2\cos\theta\sin\theta\right)\hat{\theta}\right). \quad (2.15)$$

In figure 2.2 we use pairwise additivity and equations 2.14 and 2.15 to generate a plot that illustrates the potential and forces acting on a small collection of particles.

The interaction of chains of dipolar particles

Around an infinite rigid chain of dipoles the magnetic field depends on the perpendicular separation of the chains, d, and the longitudinal displacement, z, and has the form [84, 85]

$$B(d,z) \approx -(2\pi)^2\left(\frac{\mu_0 m}{4\pi d^2 a}\right)\left(\frac{a}{d}\right)^{1/2} e^{-2\pi d/a}\cos(2\pi z/a). \quad (2.16)$$

The energy of interaction between two chains is then the integral over the dipole moment density with this field [84, 86]:

$$U(d) = \pm(2\pi)^2 \frac{2\mu_0 m^2}{4\pi d^2 a} \left(\frac{a}{d}\right)^{1/2} e^{-2\pi d/a}. \tag{2.17}$$

This a rapid exponential decay indicating that there is typically minimal interaction between chains, except at small separations, which are common at high concentrations. The interaction is attractive or repulsive depending on whether the particles are in register or out of register, as illustrated in figure 2.3*a*.

For finite chains the total interaction energy of the two chains is the double sum of all interactions of particles in one chain with particles in another. First, we consider 2 chains far apart such that to a good approximation all the distances and angles between particles are the same. In this case the total interaction energy, U_{tot}, is given by

$$U_{\text{tot}} \approx \sum_{j}^{n_j} \sum_{i}^{n_i} U_{i,j}(r,\theta) = n_i n_j U_{i,j}(r,\theta), \tag{2.18}$$

where n_i and n_j are the number of particles in each chain.

The above approximation is true when the extent of the chains is short relative to their separation, i.e. $l \ll d$. At higher concentrations of chains they are often too close for this to apply. Using the coordinate system introduced in figure 2.3*b* the interaction potential between two particles, equation 2.12, can be rewritten in terms of the particle index using the substitutions

$$r = (d^2 + (z + 2ai - 2aj)^2)^{1/2} \quad \text{and} \tag{2.19}$$

$$\cos\theta = (z + 2ai - 2aj)/r. \tag{2.20}$$

The total interaction energy between chains is then the double sum of the interactions of particles in different chains. This double sum can be replaced by a double integral when the separation of chains is greater than a particle radius, $d > 2a$ [87]:

$$U_{\text{tot}}(d,z) = \sum_{j}^{n_j} \sum_{i}^{n_i} U_{i,j}(r,\theta) \approx \int_{j=0}^{n_j} \int_{i=0}^{n_i} U_{i,j}(r,\theta)\ didj. \tag{2.21}$$

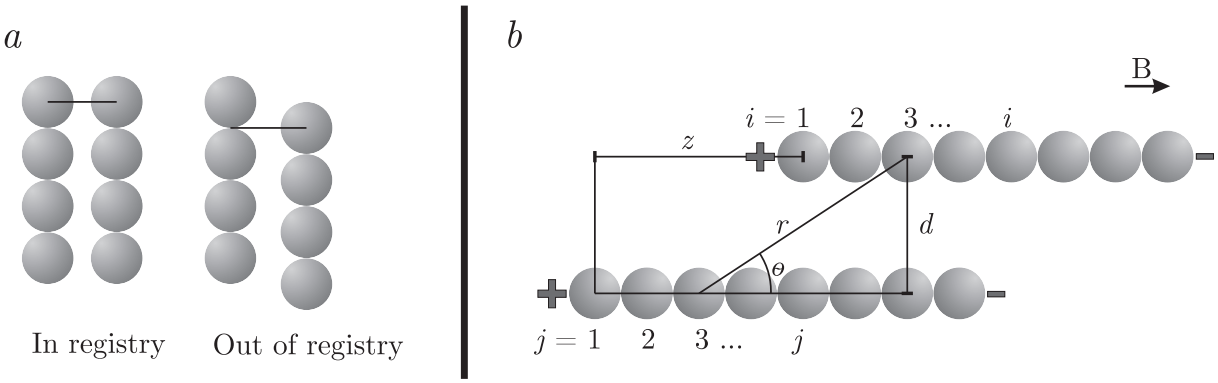

Figure 2.3: (a) A pair of chains in registry and pair of chains out of registry. (b) Two finite chains indicating the indexing and coordinates used in equation 2.19 and 2.20. Equation 2.22 shows that the interaction is equivalent to a coloumbic interaction of charges on the ends of the chain, these fictional charges are illustrated.

We find that the interaction of two parallel rigid rods is then

$$\frac{U_{\text{tot}}(d,z)}{k_BT} = \frac{\lambda}{2}\Bigg(- \frac{1}{\sqrt{(d/2a)^2 + ((z-l_j)/2a)^2}} - \frac{1}{\sqrt{(d/2a)^2 + ((z+l_i)/2a)^2}} + \frac{1}{\sqrt{(d/2a)^2 + (z/2a)^2}} + \frac{1}{\sqrt{(d/2a)^2 + ((z+l_i-l_j)/2a)^2}}\Bigg). \tag{2.22}$$

The interactions of two chains, therefore, is equivalent to a coulombic interaction of fictional charges placed at the ends of the chains, as indicated in figure 2.3*b* [33, 87]. We note that at large separations of the chains a dipolar form is regained, as is required for consistency with equation 2.18.

Only for shifts larger than half the chain length, $z > l/2$, does this represent an attractive interaction. However, even at lower values of z, this interaction leads to a torque being exerted on the chains [33]. Due to the proximity of chains, they will rotate and come into contact at a point. Subsequently, a rapid "zippering" motion is observed as the chains come together laterally [22, 88].

Modifications of the magnetic field around an infinite chain, equation 2.16, can lead to stronger interactions [84] which will change how chains and networks coarsen. When thermal fluctuations of the chain are significant an algebraic decay is observed [85]. Additionally, at the concentrations that we probe experimentally, there are defect driven interactions [84,89], as well as the interactions of the ends of chains [33, 90], that can drive aggregation and coarsening [88].

2.3 Experimental Methods

2.3.1 Optical microscopy

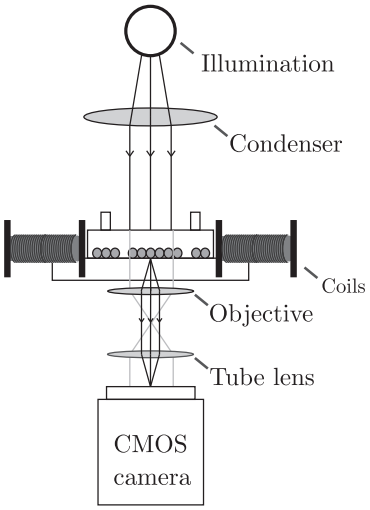

Figure 2.4: A schematic of a simple microscope with solenoids placed symmetrically either side of the sample. The sample of colloidal particles, positioned at the focal plane of the objective lens, is illuminated from above and focused onto a CMOS camera camera below.

Throughout this thesis, we use optical video microscopy to study magnetically induced assembly of colloidal particles. Figure 2.4 illustrates the basic principle of a optical video microscope. The sample is illuminated with collimated light which scatters off a colloidal particle. The scattering pattern is then focused, through an objective, onto a digital camera, which takes snapshots of the aggregation process. In this thesis we use a Olympus CK41 inverted microscope equipped with a Ximea xiQ USB3 CMOS camera that acquires 2048×2048 8 bit grey-scale images. Depending on the experiment, $4\times$ - $40\times$ objectives are used.

The external magnetic field was provided by two 470 turn solenoids, placed symmetrically either side of the sample cell giving a stable, locally uniform, magnetic field (figure 2.4). The magnetic field was varied in the range of $0 - 3.2$ mT, as was characterised with a Gaussmeter (Hirst Magnetic Instruments Ltd. GM07 Gaussmeter, PT002 Hall Probe). The power supply is controlled by a LabJack U3-LV, which has sub millisecond response times, this allows precise control of the imposed field.

The camera and magnetic field are controlled by software constructed in LabVIEW. To capture the aggregation processes in their entirety the frame rate is adjusted during the experi-

ment to give a non-uniform sampling of time. Controlling both the field and image acquisition from one piece of software allows for complete synchronization. For example, the frame rate can be adjusted from precisely the moment the field is applied and the field values, alongside millisecond timestamps, saved into the image file names.

2.3.2 Colloidal model system

We use aqueous suspensions of paramagnetic polystyrene spheres (carboxylic acid functionalised Dynabeads® M-270, Invitrogen), with a diameter of 3.0 μm and a mass density of $\rho = 1.6$ g cm^{-3}. These are highly monodisperse cross-linked polystyrene spheres with carboxyl functional groups at the surface. These functional groups give the surface of each particle a net negative charge which stabilises them against aggregation due to the electric double layer, section 2.2.1.

Due to their relatively high mass density they form a mono-layer at the bottom of the sample cell where they diffuse with a Brownian time of $t_B \sim 50$s, equation 2.2. The out-of-plane fluctuations are negligible as can be inferred from the particle's gravitational height, equation 2.3; for our system $h_g = 0.06$ μm, which is only a fraction of the particle radius.

The particles are contained in a 200 μm thick quartz glass cell (Hellma Analytics) and, after sedimentation, are allowed to equilibrate for several minutes before being exposed to a magnetic field. Due to magnetic nano-particles, γFe_2O_3 and Fe_3O_4, embedded in the polymer matrix, these particles are superparamagnetic. The magnitude of the induced magnetic moment is proportional to the external field for sufficiently small fields. Using SQUID measurements, we confirmed that our experiments are conducted within this region of reversible linear magnetisation, and find a dimensionless volume susceptibility of $\chi = 0.76$, consistent with previous studies [91]. This corresponds to an interaction parameter, equation 2.13, between $0 \leq \lambda \leq 1000$ for the range of magnetic fields used in this thesis.

2.4 Image analysis

Throughout this thesis we will rely on the accurate detection of particles from digital images. As well as the location of particles we are also interested in their local environment, in particular which particles neighbour which other particles and the clusters they belong to. The process of

particle detection is common in the field of soft matter and several open source programs exist that aim to locate and track colloidal particles [92, 93]. Here we use Wolfram's Mathematica to write bespoke image analysis algorithms tailored to our specific needs. Writing our own programs allows the combination of novel approaches to specific problems, such as our cluster determination, with standard image analysis approaches.

We outline in general terms two different procedures used to identify particles. We also show how we identify clusters of particles. This is a key step in the analysis of an aggregating system and is achieved in two novel ways that simplify and accelerate the process compared to traditional methods.

2.4.1 Particle detection by intensity thresholding

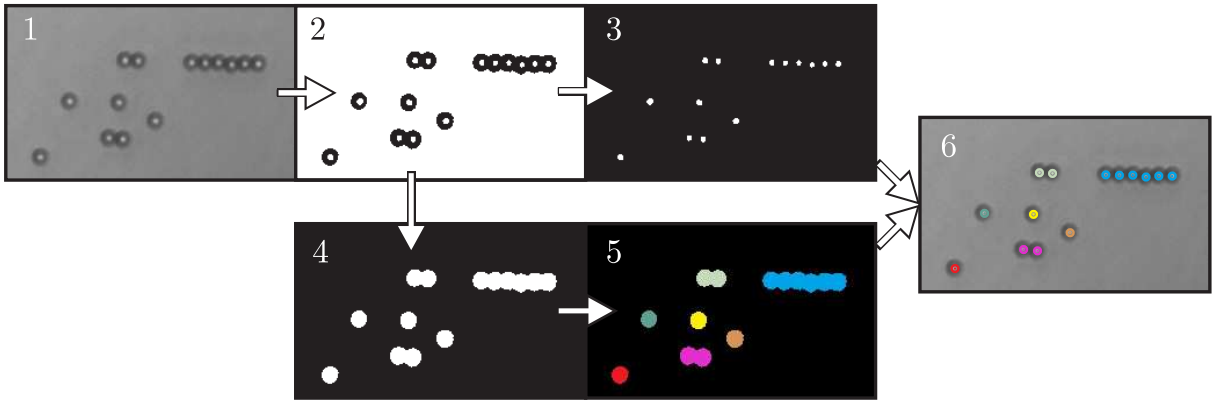

Figure 2.5: Particle detection based on intensity thresholding, see text for details.

Figure 2.5(1) shows the typical appearance of particles when observed with a bright field microscope. Qualitatively, relative to the background intensity particles are seen as a bright central spot surrounded by a dark ring. This description of the particle in terms of intensity is sufficient to systematically identify them.

The image may be segmented into a binary image, an array of 1s (white) and 0s (black), based on a threshold intensity value. Picking out the bright regions of an image reveals the center of particles (figure 2.5(2) and (3)). Connected groups of white pixels can be identified and characterised by morphological transforms [94].

To identify the particles that belong to the same cluster, we note that there is a dark ring around all the particles that is picked up by thresholding (figure 2.5(4) and (5)). We consider

that when coordinates are encapsulated by the same dark region they are members of the same cluster (figure 2.5(6)). If a dark region is in contact with the edge of the image, we discard the coordinates it encapsulates as we cannot know the true size of that cluster. This process for establishing clusters has an advantage over using a simple distance criterion, used to determine neighbouring particles, in that if a chain incorporates a single anomalous particle that is not detected by thresholding we will not consider this as two separate clusters.

The entire image analysis process is summarised below, and the numbered items in the list correspond to the panels in figure 2.5.

1. Acquire a digital microscopy image focused so that the particles have a bright spot in their center and a dark ring around them.
2. Perform a two level threshold on the image. The threshold value used is found automatically by the Otsu method [95].
3. Select the small components, leaving only the pixels that correspond to the bright spots of the particles. Find the coordinates of the particles from these components.
4. Following from step 2, select only the large components and invert the image. The resulting white regions correspond to the filled areas of the dark rings in the original image.
5. Label each component in step 4, removing components that are in contact with the edge of the image.
6. Associate the coordinates of particles from step 3 with the labels from step 5. Gathering a list of coordinates that have the same label gives a list of coordinates that belong to the same cluster.

2.4.2 Particle detection by watershedding

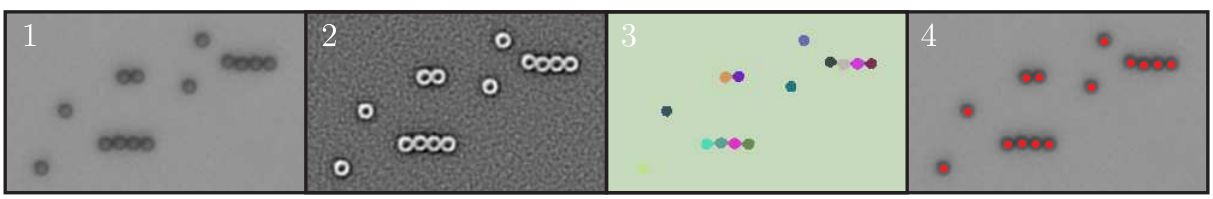

Figure 2.6: Particle detection based on a watershed, see text for details.

Under different illumination conditions, or with a different focusing of the microscope, the bright spot at the center of particles may be less pronounced. In figure 2.6(1) we show an image of the same particles as in figure 2.5(1), but with a different illumination. In this case an intensity threshold does not reliably identify particles. The change in intensity, however, can be found with various filters [96]. We apply a Laplacian of Gaussian filter to pick out the gradient of intensity between background and particle (figure 2.6(2)). The background is almost constant and has low values of intensity gradient and the same holds for the interior of particles. However the boundary between the two has a larger value because of the change in intensity.

We now have regions of low intensity bound by high intensity. These are readily segmented with watershedding methods [97]. A watershed considers the intensities as heights and floods the image, from the local minima, separating components along the connecting lines of these basins (figure 2.6(3)). The coordinates of the particles are the centers of mass of these components (figure 2.6(4)). Watershedding can be particularly powerful for images with gradients in the background intensity because the Laplacian filter only relies on local variation. It is also powerful for identifying particles lacking pronounced bright centers but with well defined edges.

The entire process is summarised below and the numbered items in the list correspond to the panels in figure 2.6.

1. Acquire a digital microscopy image in which particles have distinct edges but smooth internal intensity profiles.

2. Convolve the image with a Laplacian of Gaussian kernel with a radius corresponding the length scale of the intensity change corresponding to the edge of the particle. The Gaussian kernel helps reduce the impact of noise that otherwise would mimic gradients in intensity that the Laplacian kernel highlights.

3. Watershed the gradient image with a mimimum saliency condition, i.e basins whose boundary is below a given value are joined.

4. Find the center of mass of particles using the components determined in 3. In figure 2.6(4) the result of this analysis is shown.

2.4.3 Cluster detection with minimum-bandwidth orderings

Above, we outlined a way of establishing clusters based on an optical property of the image, i.e. based on a shared dark ring around particles. In this thesis we also need a way of determining clusters that relies on the coordinates of particles only.

This can be done as follows. Consider the collection of particles shown in figure 2.7*c*. Each particle is automatically assigned a label i. First, we establish which particles to consider as connected in an adjacency matrix $\mathbf{A} = a_{i,j}$. If the matrix element $a_{i,j} = 1$ then particle i neighbours particle j and if $a_{i,j} = 0$ they do not neighbour each other. Adjacency is determined by a distance threshold, r_{cut}, that we choose to be the first minimum of the pair-correlation function $g(r)$. Figure 2.7*a* shows the adjacency matrix for the collection of particles in figure 2.7*c*, values of 1 are black and values of 0 are white.

By definition, a particle from one cluster neighbours no particles in clusters other than its own. Grouping particles belonging to the same cluster together, therefore, gives a block diagonal matrix. This is illustrated in figure 2.7*b*, where we have revealed a block diagonal structure in the adjacency matrix by permuting rows and columns. To this end, we have used a minimum bandwidth transformation to tell us how to permute the rows and columns to achieve this. In brief, the bandwidth, which is defined for a particle, is given by [98]

$$bw_i = \max_{a_{i,j}\neq 0}|i-j|, \tag{2.23}$$

and the profile of the adjacency matrix is defined as [98]

$$Pr(\mathbf{A}) = \sum_i bw_i = \sum_i \max_{a_{i,j}\neq 0}|i-j|. \tag{2.24}$$

The bandwidth is the distance of the furthest non-zero element from the diagonal, and the profile is the sum of these values. The bandwidth of an element can be reduced by exchanging rows in the adjacency matrix. The minimum bandwidth ordering minimizes the profile and hence brings all elements as close to the diagonal as possible. From the block diagonal form shown in figure 2.7*b* we can see that exchanging particles from different clusters would necessarily increase the profile, confirming that it is a minimum of bandwidth ordering. Methods exist for determining the list of permutation that transform a matrix to a minimum bandwidth ordering and we use

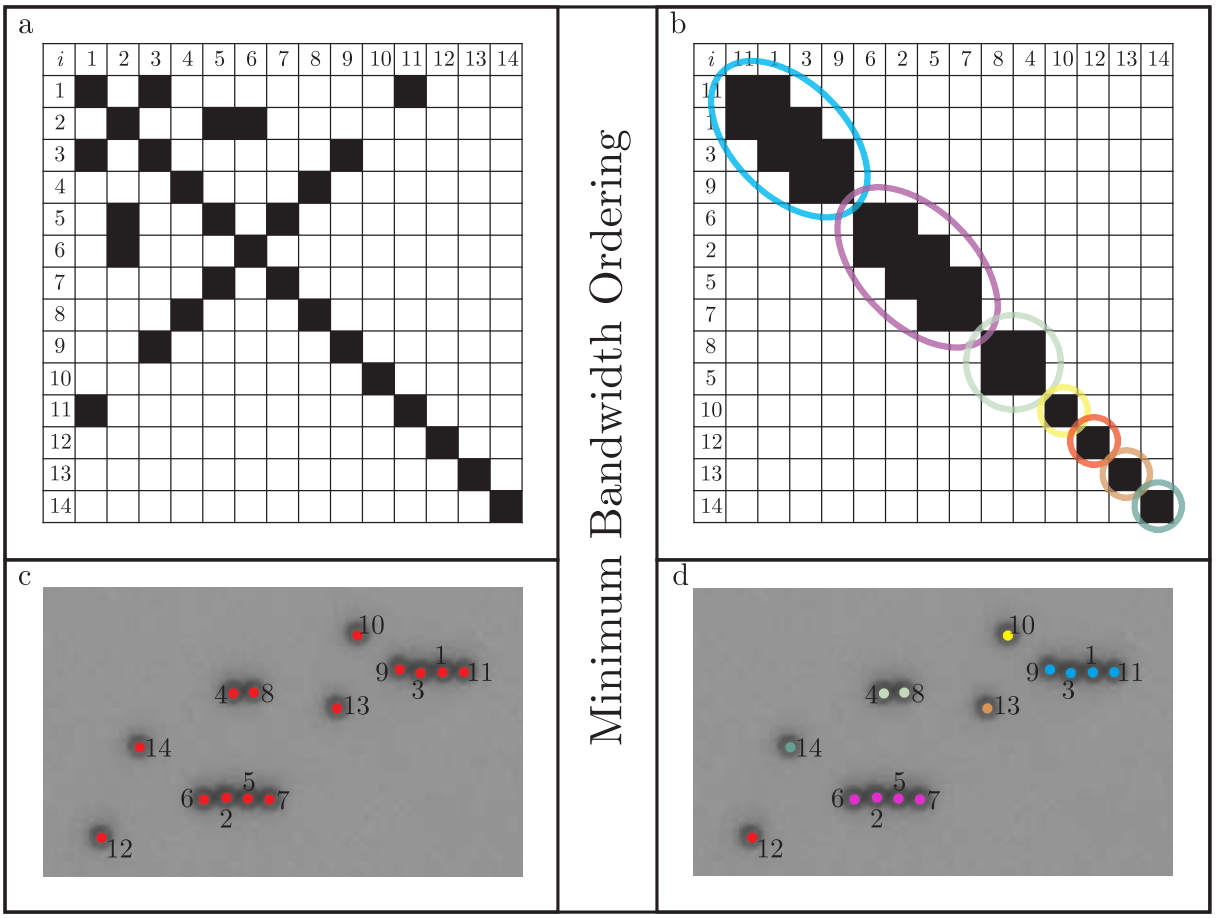

Figure 2.7: (a) The adjacency matrix for the particles shown in c and d, with the particle labels along the top and left hand side. Black squares correspond to values of 1 (neighbours), and white squares to values of 0 (not neighbours). (b) The adjacency matrix for the same particles where rows and columns have been exchanged to reveal clusters. Clusters are the circled blocks in the now minimum bandwidth ordered matrix. (c) Micrograph of particles with the labels shown. (d) Micrograph of the same particles as a with the different clusters coloured according the blocks shown in b.

Sloan's method [98]. In figure 2.7d we colour particles according to which block they are in in the minimum bandwidth ordered matrix, corresponding to the coloured disks in figure 2.7b, confirming that these blocks correspond to cluster of particles.

Also from the adjacency matrix, the coordination number of a particle i, c_i, can be calculated as

$$c_i + 1 = \sum_j a_{i,j}. \tag{2.25}$$

The coordination number of particles is of particular interested to us in chapters 4 and 6 and will be determined in this way.

Chapter 3

Deterministic aggregation kinetics of paramagnetic colloidal particles

ABSTRACT

In this chapter we study the irreversible aggregation kinetics of two-dimensional paramagnetic colloidal particles in the presence of an in-plane magnetic field at low packing fractions. Optical microscopy and image analysis techniques are used to follow the aggregation process and in particular study the packing fraction and field dependence of the mean cluster size. We compare experimental results to the predicted scalings for diffusion limited and deterministic aggregation respectively. It is shown that the aggregation kinetics for our experimental system is consistent with a deterministic mechanism, which thus shows that the contribution of diffusion is negligible.

3.1 Introduction

In the introduction, chapter 1, we introduced the idea of magnetically responsive systems and noted that the response profile of a device based on these materials will depend on the dynamics of structure formation. These devices rely on the formation of chains and clusters causing the observed changes in physical parameters, such as the viscosity [24]. Investigations have therefore focused on the dynamics of cluster formation at low particle packing fractions with work in two and three dimensions [21,22], real space experiments [99–110], scattering experiments [111–118],

and simulations [87, 90, 119–121].

Theoretical predictions based on a *diffusion limited irreversible aggregation* mechanism [122, 123], along with experimental [21, 22, 111, 118] and simulation work [124, 125], point to the mean cluster size, $\langle L \rangle$: equation 3.2, growing as a power law in time, t, with an exponent z': $\langle L \rangle \sim t^{z'}$. Predictions of these exponents have been given in the range of $0.5 < z' < 0.6$ [21]. Many investigations are reported in terms of a mean weighted by the number of particles in a cluster, $\langle S \rangle$: equation 3.3, that grows with a different exponent z: $\langle S \rangle \sim t^{z}$, though it has been established that $z \approx z'$ [99, 100, 106]. In addition, it is proposed that time can be rescaled to account for the dependence of the average cluster size on the external magnetic field, B, and the packing fraction, ϕ [21, 22, 99, 111, 119, 126].

When magnetic interactions dominate Brownian forces, a *deterministically controlled aggregation* process is proposed [21, 29, 106, 107]. In this regime, it has been predicted that the growth of the mean cluster size follows a power law, like in the diffusion limited case, but with a different packing fraction and magnetic field dependence [87, 90, 101, 127]. However, a detailed and quantitative experimental study of deterministic aggregation that simultaneously considers both the packing fraction and field dependence is lacking. In this chapter, we use a paramagnetic colloidal model to study the field induced aggregation using video microscopy. In particular, we measure the growth of the mean cluster size and propose a method for explicitly extracting the parameters that characterise the field and packing fraction dependence.

This chapter is organised as follows: we will start with a theory section which briefly introduces the theories of diffusion limited aggregation (section 3.2.2) and deterministically controlled aggregation (section 3.2.3). The experimental system is then introduced with details of the range of concentrations and fields that are probed (section 3.3). The data treatment is detailed and used to extract scaling parameters for the packing fraction and field dependence. The results of this processing are presented in section 3.4 for a range of packing fractions and field strengths. We discuss the results in light of the two proposed theories with particular focus on the packing fraction and field dependence.

3.2 Theory

3.2.1 Interactions between magnetic particles

The interaction between paramagnetic colloidal particles in the presence of an external field is dominated by their magnetic moments. This interaction is discussed in section 2.2.2 in the previous chapter. From equation 2.14 we have that the interaction energy, cast in terms of the interaction parameter λ, is

$$\frac{U_{ij}}{k_{\mathrm{B}}T} = \frac{\lambda}{2\left(r/2a\right)^3}\left(1 - 3\cos^2\theta\right), \tag{3.1}$$

where λ (equation 2.13) is the energy released in bringing two particles into contact from an infinite separation in units of $k_{\mathrm{B}}T$.

The result of applying a field is the evolution of a distribution of different cluster sizes, s, where s is the number of particles in a cluster. The mean is defined as,

$$\langle L \rangle = \frac{\sum_s s n_s}{\sum_s n_s}, \tag{3.2}$$

where n_s is the number of cluster of size s present in a snapshot [106]. The number weighted mean cluster size is given by

$$\langle S \rangle = \frac{\sum_s s^2 n_s}{\sum_s s n_s}. \tag{3.3}$$

3.2.2 Diffusion limited aggregation

Diffusion limited aggregation kinetics in dipolar systems has been described extensively, see e.g. [111, 125, 126, 128], and therefore we only briefly recap the essentials. From Smoluchowski's kinetic equation of aggregation one can, in certain limits, give expressions for the average cluster size as a function of time for an irreversible diffusion limited aggregation mechanism [123]. In essence, the equation is a rate equation involving a reaction kernel that describes the rate at which clusters of size i and j join. Taking the collision cross section of clusters of different sizes to be the same, and the diffusion coefficient of a cluster to have a power law dependence on its

size, $D_s \sim s^{\gamma}$, the average cluster size grows as [21]

$$\langle L \rangle \sim t^{1/(1-\gamma)}. \tag{3.4}$$

Hence, if the friction of a chain is taken to be proportional to its length, then $\gamma = -1$, and $\langle L \rangle \sim t^{1/2}$ [123]. The choice of γ gives a range of values for $0.5 < z' < 0.6$ [19, 21, 22]. For the diffusion dominated case a time rescaling based on the time to diffuse to a capture radius, within which particles are rapidly drawn together, i.e. the typical time for doublet formation, t^*_{DIFF}, is proposed [21, 104, 112]. This capture radius is often defined by the region around the particle in which the interaction due to the magnetic dipoles equals the thermal energy, $U_{ij}/k_{\mathrm{B}}T = 1$. In 2D and for a given packing fraction, ϕ, this leads to the following expression for t^*_{DIFF} [21, 104, 119]

$$t^*_{\mathrm{DIFF}} \sim \frac{a^2}{D\lambda^{2/3}\phi}. \tag{3.5}$$

This implies that for diffusion limited aggregation, noting the definition of λ (equation 2.13), this characteristic time is proportional to $1/B^{4/3}$ and $1/\phi$.

3.2.3 Deterministic aggregation

Next, we introduce the deterministically controlled aggregation largely following [127] with a potential of the form of equation 3.1. For small clusters of size s that are relatively far apart, and aligned with the magnetic field, the interaction energy between the clusters is approximated by s^2 multiplied by the inter particle potential U_{ij}, equation 3.1, with $\theta = 0°$:

$$\frac{U_s}{k_{\mathrm{B}}T} = -\frac{s^2\lambda}{(r/2a)^3}. \tag{3.6}$$

The force, $F_s = -\partial U_s/\partial r$, is then given by

$$F_s = -\frac{24a^3s^2\lambda k_{\mathrm{B}}T}{r^4}. \tag{3.7}$$

This attractive magnetic force is balanced by a drag force, F_{drag}, which depends on the cluster size s [120]. Here, we take the friction of a chain to be proportional to the number of particles it contains, so that $F_{\mathrm{drag}} = -s6\pi\eta a v$ [123], where η is the viscosity of the solvent, and v the velocity of the cluster.

In the overdamped limit, the equation of motion becomes:

$$F_s + F_{\text{drag}} = -\frac{24a^3 s^2 \lambda k_{\text{B}} T}{r^4} - 6s\pi\eta a \frac{\mathrm{d}r}{\mathrm{d}t} = 0. \tag{3.8}$$

We integrate the equation of motion taking the final separation as zero and the initial separation, R_0, between clusters of size s in a system of packing fraction ϕ as $R_0 = a\,(s/\phi)^{1/2}$. It then directly follows that the time for two clusters of size s to come together, τ_s, is

$$\tau_s = \left(\frac{\pi\eta a^3 s^{3/2}}{20\lambda\phi^{5/2} k_B T} \right). \tag{3.9}$$

Assuming hierarchical growth, the total time for a cluster of size s to form, t_s, is then given by the sum $t_s = \tau_{s/2} + \tau_{s/4} + ... + \tau_1$. The expression for t_s corresponds to a geometric series, $t_s = \tau_s(\epsilon + \epsilon^2 + \dots)$, with $\epsilon = (1/2)^{3/2}$. In this model, the cluster size s is equal to the mean cluster size $\langle L \rangle$, which is therefore found to grow as

$$\langle L \rangle \sim \left(\frac{20 k_B T \lambda \phi^{5/2}}{\pi\eta a^3} t \right)^{2/3}, \tag{3.10}$$

predicting $z' = 2/3$ [127]. A typical time scale, t^*_{DET}, can then be identified using that $\langle L \rangle \sim (t/t^*_{\text{DET}})^{2/3}$, so that

$$t^*_{\text{DET}} \sim \frac{a^2}{D\lambda\phi^{5/2}}, \tag{3.11}$$

which is proportional to $1/B^2$ and $1/\phi^{5/2}$.

3.3 Methods

In this chapter we use the experimental system that we outlined in section 2.3.2. In summary, we use an aqueous suspensions of paramagnetic polystyrene spheres with a diameter of 3.0 μm and a mass density of $\rho = 1.6$ g cm^{-3}. We investigate samples with packing fractions in the range $0.01 < \phi < 0.05$, and subject to magnetic field strengths in the range $B = 0 - 3.2$ mT (interaction parameters in the range $0 < \lambda < 1000$). Due to their relatively high mass density they form a mono-layer at the bottom of the sample cell.

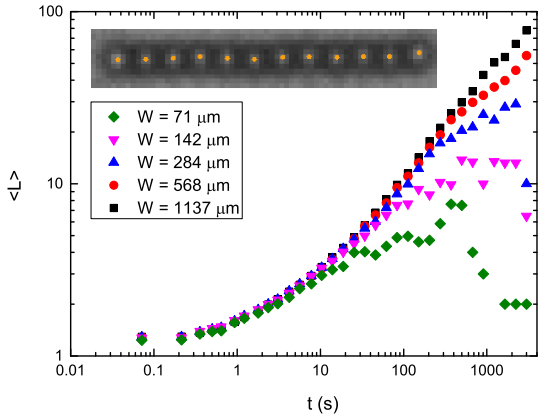

Figure 3.1: The mean cluster size $\langle L \rangle$, equation 3.2, against time for different observable rectangular regions of width W for a single experimental run with a packing fraction $\phi = 0.037$ and an external magnetic field $B = 3.12$ mT. The full field of view is 1150×1150 μm^2. The inset shows a microscopy images of a typical cluster with the results of our image analysis algorithm plotted over it.

The chain formation is captured using video-microscopy and analyzed with the methods outlined in section 2.4. In particular, we use intensity thresholding to identify particles (see inset in figure 3.1). Once the clusters have been identified, the mean cluster size $\langle L \rangle$, equation 3.2, is computed. As the typical cluster length becomes on the order of the image width, W, finite size artefacts can start to impede on the analysis of the cluster sizes. To test these effects we systematically increased W at the maximum magnetic field and highest packing fraction used, $B = 3.12$ mT and $\phi = 0.037$ respectively, and monitored the convergence of the mean cluster size as W increases (figure 3.1). Note that this analysis is performed on a single experimental run, so the error in $\langle L \rangle$ cannot be defined. This analysis shows that only at very late times the mean cluster size may be affected by the finite field of view.

3.4 Results and discussion

Figure 3.2 presents a series of images capturing the process of aggregation into linear chains upon application of an external magnetic field. Particles, starting from an initially random configuration, come together to form one particle thick chains. Chains of two particles thick are negligible at the low packing fractions used as they are not formed in significant quantities over the timescale of observation. Inherent to the strong interactions the chains are rigid and thermal

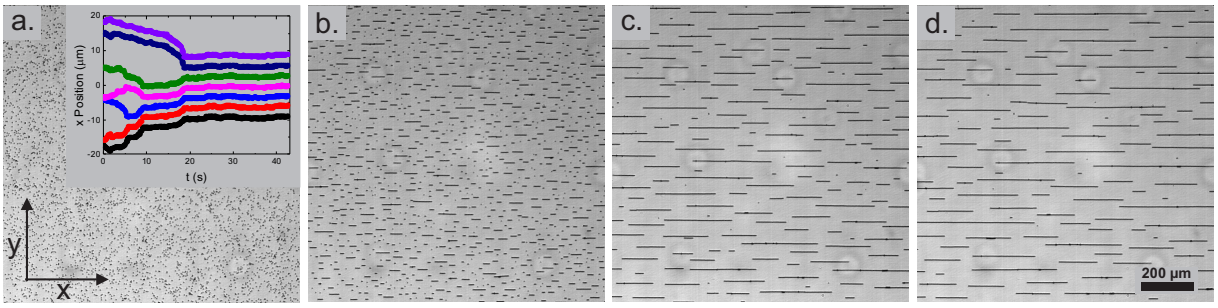

Figure 3.2: Microscopy images for different times showing the magnetic field induced chain formation. Panel (a) shows the initial state of the system before the magnetic field is applied. Panels (b-d) show the system at respectively 95 s, 1680 s and 3000 s after a constant uniaxial magnetic field is applied in the x direction at $t = 0$ s. The packing fraction is $\phi = 0.031$ and the magnetic field is $B = 1.88$ mT. The inset shows the x-positions of a small collection of particles over the first 40 seconds.

fluctuations are small. As shown in the inset in figure 3.2a, which shows the x-positions of a small collection of particles over the first 40 seconds, the particles follow well-defined trajectories which are reminiscent of deterministic rather than diffusive motion. We observed no break up events; when clusters joined to form a larger cluster they did so irreversibly.

The mean cluster size $\langle L \rangle$, equation 3.2, as a function of time is presented in figure 3.3a for different magnetic fields at a constant packing fraction. A clear monotonic growth of cluster size with time can be seen with faster growth of clusters at higher magnetic fields. Figure 3.3b shows the analogous graph for different packing fractions at a constant magnetic field. Again, a monotonic growth is observed, now with faster growth at higher packing fractions. In both cases the long time behaviour shows an apparent power law scaling of the mean cluster size with time, consistent with earlier reports [99]. We note that at early times, just after the field is applied, the cluster size depends on the packing fraction, which is due to a small number of particles that are in contact in the random starting configuration. At intermediate and long times the effects of this initial structuring are negligible.

In considering the magnetic field and packing fraction dependence of the cluster size it is common practice to plot a proposed time rescaling and judge how effective a given theory is at removing the dependence on the magnetic field and packing fraction by the quality of data collapse [21,119,129,130]. Another approach is to fit to a particular scaling law with the packing fraction dependence and field dependence as free fitting parameters [131, 132]. However, in the approach we use here we do not require a specific functional form for the cluster growth. Instead

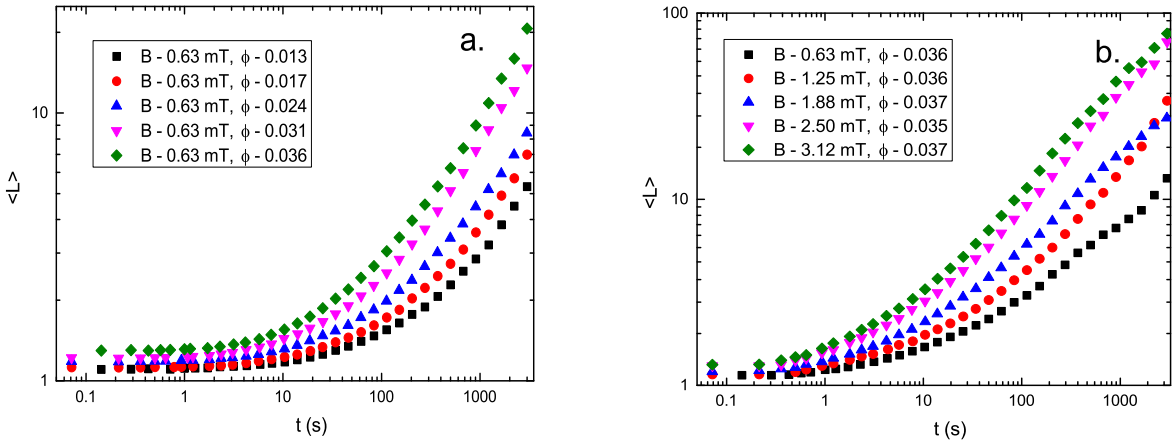

Figure 3.3: The mean cluster size, $\langle L \rangle$, as a function of time, t, for experimental runs at (a) a constant packing fraction $\phi \approx 0.036$ and an increasing magnetic field B and (b) a constant magnetic field $B = 0.63$ mT and an increasing packing fraction ϕ.

we write that the mean cluster size, $\langle L \rangle$, grows as a monotonic scaling function f of unspecified form of the variable $t^* = \phi^\alpha B^\beta t$, such that

$$\langle L \rangle = f\left(\phi^\alpha B^\beta t\right). \tag{3.12}$$

Here, α and β are scaling constants that characterise the packing fraction and field dependence of the growing mean cluster size. Comparison to equations 3.10 and 3.11 shows that the deterministic model predicts values of $\alpha = 5/2$ and $\beta = 2$, while the diffusive theory equation 3.5 predicts values of $\alpha = 1$ and $\beta = 4/3$.

Equation 3.12 states that a particular mean cluster size is generated by the same $\phi^\alpha B^\beta t$. As the magnetic field B is strictly controlled in our experiments, we first consider chain formation for varying ϕ and constant B. In particular, we measure the time at which a given cluster size is reached for different packing fractions ϕ, as shown in figure 3.4. Because $\phi^\alpha t$ is constant for a given mean cluster size, the exponent α is directly obtained from the gradient of $\ln t$ vs. $\ln \phi$ as shown in the inset of figure 3.4. The determination of the exponent α is robust with respect to the choice of the given cluster size as is also illustrated in figure 3.4, where the light grey lines correspond to the same analysis for a smaller given cluster size. In general, we choose the largest mean cluster size common to all data sets as the given cluster size.

Having established the value of α, an analogous procedure is performed to determine the

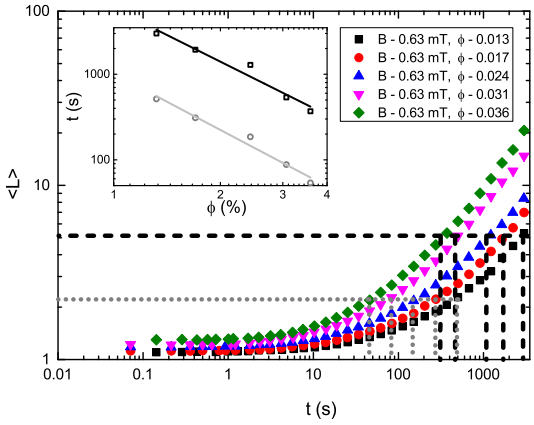

Figure 3.4: The mean cluster size $\langle L \rangle$ against time for experimental runs at different packing fractions ϕ but with the same magnetic field B. The horizontal lines cut the curves at the same cluster size. The vertical lines, dropping from the intersects, show the time at which that cluster size occurred. The inset shows the packing fraction against the time at which a particular cluster size was achieved and the solid line is the linear fit to the data.

exponent β for the magnetic field dependence. The mean cluster size can be considered as $\langle L \rangle = f(B^\beta(\phi^\alpha t))$ and because the factor $\phi^\alpha t$ is known, the effect of the magnetic field strength on the growth kinetics can be determined. To this end, we determine the $\phi^\alpha t$ at which a given mean cluster size is reached for different field strengths B. The exponent β is then extracted from a linear fit of $\ln(\phi^\alpha t)$ vs. $\ln B$.

The values for the exponents α and β extracted from our experiments, alongside the values as predicted from diffusive and deterministic aggregation, are summarised in table 3.1. We also determined the exponents using the number weighted mean $\langle S \rangle$, equation 3.3, and very similar values were obtained, which shows that both means scale in the same way with ϕ and B. The value for α is consistent with deterministic aggregation, while the exponent β is in between what is expected for diffusive and deterministic aggregation. We note however that a very small fraction of particles ($\leq 0.1\%$) is pinned to the glass surface, which will hinder the growth of clusters, particularly at long times as they are incorporated into chains. As such, this may

Table 3.1: A summary of the experimentally obtained values for the exponents ϕ^α and B^β alongside the theoretical prediction for the diffusive and deterministic aggregation.

exponent	experimental	diffusive	deterministic
α	2.44	1	5/2
β	1.61	4/3	2

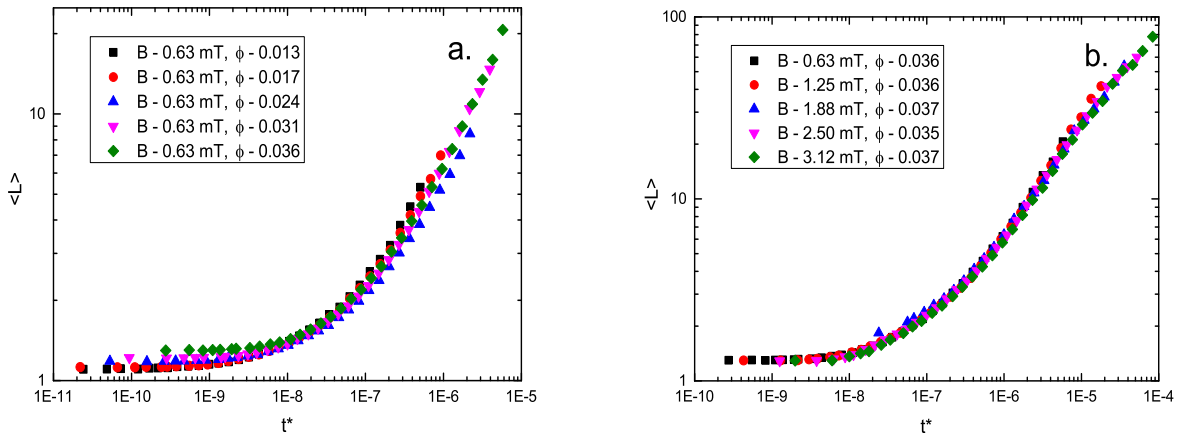

Figure 3.5: The mean cluster size, $\langle L \rangle$, as a function of the rescaled time, $t^* = \phi^\alpha B^\beta t$, where α and β are the values obtained from the experiments (see table 3.1). In panel (a) the experimental runs at a constant packing fraction, $\phi \approx 0.036$, and an increasing magnetic field B are presented, while panel (b) shows the experimental runs a constant magnetic field, $B = 0.63$ mT, and an increasing packing fraction ϕ. Note that the data presented here is the same as in Figure 3.3.

contribute to the deviation from theory in our experimentally measured β value. Nevertheless the combination of the excellent agreement of the packing fraction dependence and the field dependence being larger than the diffusive prediction makes us confident that deterministic aggregation is the key mechanism behind the chain formation in our system.

The data presented in figure 3.3 can now be re-plotted as a function of the rescaled time $t^* = \phi^\alpha B^\beta t$ using the experimentally determined values for α and β (table 3.1). The rescaled plots are presented in figure 3.5 and as expected an excellent data collapse is observed for the magnetic field (a) and packing fraction (b) dependent data[1]. Finally, we show in figure 3.6 the master curve of $\langle L \rangle$ versus t^* averaged over all experimental runs. The data is excellently described by a power law fit of the form, $\langle L \rangle = a + bt^{*^{z'}}$. Here, a represents the zero time cluster size, which we expect to be close to unity as at the low packing fractions used most particles will not be close enough to be considered as neighbours. Consistent with this we find that $a = 1.12$. The pre-factor is found to be $b = 3.1 \cdot 10^4$ and the exponent $z' = 0.61$. The value of z' is in very good agreement with the deterministic model, equation 3.10, but also lies in the range of diffusive theory, equation 3.4, which prevents any distinction using the exponent. Despite the fact that we cannot distinguish mechanisms from the exponent z', we can do so from the

[1]Data collapsed by the time rescalings predicted by the diffusive and deterministic theories presented in section 3.2.2 and section 3.2.3 (equations 3.5 and 3.11) are shown in the appendix, figure A.1.

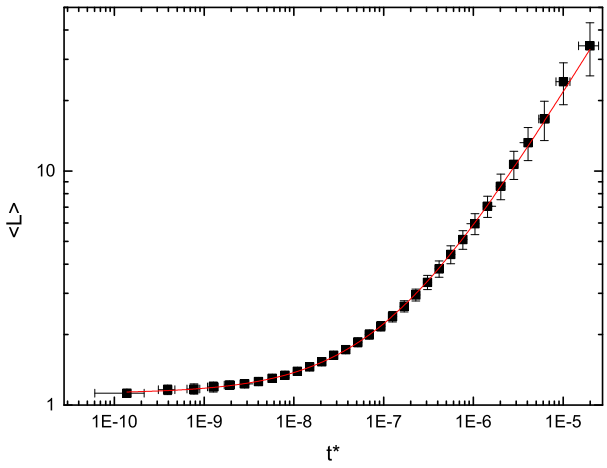

Figure 3.6: The mean cluster size, $\langle L \rangle$, averaged over all 25 experimental runs, plotted as a function of the re-scaled time, t^*. The error bars correspond to the standard deviation of all the experimental runs. The solid line is a power law fit to the data of the form $\langle L \rangle = a + bt^{*^{z'}}$, is performed and plotted through these points in red. The fitting parameters are $a = 1.12, b = 3.1 \cdot 10^4$ and $z' = 0.61$.

exponents characterising the packing fraction and magnetic field dependence, which indicate a deterministic mechanism. Importantly, our approach allows the complete characterisation of the field and packing fraction dependence of chain formation without pre-assuming a mechanism. Combining the exponents α and β and the fitting parameters a, b and z', thus fully predicts the time at which a given mean cluster size is reached.

3.5 Conclusions

The magnetic field induced aggregation of paramagnetic colloidal particles into linear chains has been studied in two dimensions using video microscopy. We find that the mean cluster size grows as a power law in time. The exponents that characterise the packing fraction and magnetic field dependence of the mean cluster size are directly determined from the experimental data and lead to an excellent data collapse upon plotting the mean cluster size as a function of the rescaled time. Comparison to diffusion limited and deterministic models for chain formation shows that the aggregation kinetics in our system is consistent with a deterministic mechanism and that the contribution of diffusion is thus minimal.

Acknowledgements

This work was carried out in collaboration with François Lavergne, Kira Klop, and Sarah Morrow. We also thank William Sampson, David Robinson and Mark Wilson for useful discussions.

Chapter 4

Coordination number statistics of cluster formation

ABSTRACT

In this chapter, we establish a direct relation between the distribution of coordination numbers of particles and the mean cluster size using simple statistical considerations. The chain forming system that was outlined in the previous chapter is used as a model system. Empirically, a shifted geometric distribution of cluster sizes is observed, consistent with a discrete compound Poisson growth process. To corroborate the compound Poisson nature of this process, experimental results are compared to simulations in which the initial spatial distribution of particles is controlled. The generality of our approach is demonstrated using another clustering processes in two dimensions as a model system.

4.1 Introduction

Controlling self-assembly, the fascinating range of processes by which initial components build into complex structures [60–63], remains a formidable challenge. The range of different interactions and competing driving forces when many components are present in particular complicate the problem [64]. To exploit self-assembled structures for the development of useful materials and tunable devices, it is a prerequisite to have a deep understanding of the fundamental

structural and dynamical processes underlying self-assembly.

The coordination number of a constituent entity is a central quantity in self-assembling systems as this characterises the local structure around that entity [65–71]. Indeed, the geometry of molecules and hence their directional interactions result in highly specific self-assembled structures [72]. Accordingly, controlling the structure in self-assembling mesoscopic systems such as nanoparticles and colloids requires the ability to control the coordination number, resulting in considerable effort in developing directional interactions in these systems [49,54–57,133–135]. The importance of the coordination number on the rigidity of a structure has long been recognised in granular packings [136]. Somewhat surprisingly, the statistics characterising the coordination number distribution, its evolution during self-assembly, and its relation to the final structure has never been addressed in colloidal systems to our knowledge.

In this chapter, we use simple statistical considerations to provide a full prediction of the distribution of coordination numbers for individual particles in a chain forming system. Our theory is tested against experiments in which we follow the chain formation process in a system of super-paramagnetic colloidal particles upon the application of an external magnetic field [20, 21, 108, 137], an excellent model system to establish the relation between cluster formation and coordination number statistics. The validity and generality of our approach is further confirmed using atomistic computer simulations in which the starting configuration of a chain-forming system is systematically varied from random to ordered. The results of this imply that the chain growth proceeds via a compound Poisson process. Further, the probabilistic approach we develop for the chain forming system is applied to a more complex assembly system of two dimensional (2D) cluster formed in a rotating magnetic field [30, 31]. This provides a general perspective on self-assembly based on local geometry as characterised by the coordination number.

This chapter is organised as follows: we first introduce the theory of coordination number statistics of chains (section 4.2.1) and disks (section 4.2.2). The experimental methods used to probe these two cluster types are introduced and a brief overview of the image analysis used in each is given (section 4.3). We then present results of chain formation, we characterise the cluster size distribution and compare the observed coordination number distribution to the predicted distributions (section 4.4.1). Next, we present the coordination number distributions for a disk forming system and compare them to theory (section 4.4.2).

4.2 Theory

The growth of clusters results in a distribution of cluster sizes characterised by a discrete probability distribution $P(s)$. The final state of a system depends sensitively on the starting configuration; a distribution of cluster sizes evolves throughout the growth process. From this cluster size distribution, coupled with knowledge of the structures of clusters, we may elaborate the distribution of coordination numbers of particles as a function of time.

4.2.1 Chain formation

We will first consider chain formation. As a starting point for our theory we need a functional form of $P(s)$. We will show experimentally that the cluster size distribution, $P(s)$, of the chain forming system is accurately described by a shifted geometric distribution. As such we will develop the theory specifically for this distribution. It is, however, important to note that the concept is general and $P(s)$ may be replaced with an alternative distribution appropriate to another growth process.

The discrete probability distribution of a shifted geometric is given by

$$P(s) = \frac{1}{\mu}\left(1 - \frac{1}{\mu}\right)^{s-1} \quad , \tag{4.1}$$

such that $P(s)$ gives the probability of choosing a chain of size s when randomly selecting a cluster and $\sum_{s=1}^{\infty} P(s) = 1$. Here, μ represents the mean of the distribution, $\mu = \sum_{s=1}^{\infty} sP(s)$, and is equivalent to $\langle L \rangle$ from the previous chapter (equations 3.2). It has been replaced here for notational purposes.

The probability that a particle i has a coordination number c is conditional on s, the size of the cluster that the particle belongs to. We denote this probability $P(c|i;s)$. The probability that a particle i, chosen at random, is in a chain of size s is denoted $P(i;s)$. The product of the two, $P(c|i;s)P(i;s)$, is the probability of randomly selecting a particle that is in a cluster of size s and has a coordination number c, $P(c \cap i;s)$ [1]. It follows that the probability that a particle, chosen at random, has a coordination c is given by the sum over all cluster sizes of this

[1] The symbol $\cap$ represents the intersection of two events. In this case it can be read as the probability that a particle has coordination number c and that that same particle belongs to a cluster of size s.

		$P(\mathrm{c}{=}0\|i;s)$	$P(\mathrm{c}{=}1\|i;s)$	$P(\mathrm{c}{=}2\|i;s)$	$P(\mathrm{c}{>}2\|i;s)$
$s{=}1$		1	0	0	0
$s{=}2$		0	1	0	0
$s{=}3$		0	2/3	1/3	0
$s{=}s$		0	$2/s$	$(s$ - $2)/s$	0

Figure 4.1: Illustrations of clusters of different sizes, s, colour coded by their co-ordination number, c. For each cluster size the probability of finding a coordination number of 0, 1, and 2 is given, $P(c|i;s)$. The final illustration is the general case of a cluster of length s.

probability [138]:

$$P_c = \sum_{s=1}^{\infty} P(c \cap i; s) = \sum_{s=1}^{\infty} P(c|i;s)P(i;s). \tag{4.2}$$

The probability of finding a particle in a cluster of a particular size, $P(i;s)$, may be elaborated from the probability distribution, $P(s)$, as

$$P(i;s) = \frac{s\,P(s)}{\sum_{s=1}^{\infty} s\,P(s)} = \frac{s}{\mu^2}\left(1 - \frac{1}{\mu}\right)^{s-1} \quad , \tag{4.3}$$

which is a normalised probability distribution, $\sum_{s=1}^{\infty} P(i;s) = 1$. Note that $P(i;s)$ is related to the particle weighted mean $\langle S \rangle$, introduced in the previous chapter, by $\sum_{s=1}^{\infty} sP(i;s) = \langle S \rangle$.

Specifically in the case of linear chains, where only zero coordinate, one coordinate, and two coordinate particles exist, $P(c|i;s)$ may be described in terms of the cluster sizes, as shown in figure 4.1, where we illustrate how $P(c|i;s)$ depends on the cluster size. Single particles are isolated and have a coordination number of 0. For larger chains the termini of the chains each have one neighbour and the rest, the body of the chain, have two neighbours. This model neglects the possibility of cruciform defects [139], laterally aggregated chains, and other deviations from simple chains.

The probability that a particle has coordination number c, P_c, is now easily found. The

fraction of zero coordinate particles is simply the probability of isolated particles:

$$P_0 = P(i; s = 1) = \frac{1}{\mu^2} \ . \tag{4.4}$$

The fractions of particles with coordination numbers 1 and 2 follow from equation 4.2 and figure 4.1:

$$P_1 = \sum_{s=2}^{\infty} \frac{2\,P(i;s)}{s} = \frac{2(\mu-1)}{\mu^2}, \tag{4.5}$$

$$P_2 = \sum_{s=2}^{\infty} \frac{(s-2)\,P(i;s)}{s} = \frac{(\mu-1)^2}{\mu^2}, \tag{4.6}$$

such that $\sum_{c=0}^{2} P_c = 1$, i.e. the probability that a particle has either a coordination of 0, 1, or 2 is unity. From equations 4.4 - 4.6 we obtain the mean, $\bar{c}$, and the variance, σ_c^2, of the coordination number distribution as

$$\bar{c} = \frac{2\,(\mu-1)}{\mu}, \text{ and} \tag{4.7}$$

$$\sigma_c^2 = \frac{\bar{c}}{\mu}. \tag{4.8}$$

Note that $\lim_{\mu\to 1} \bar{c} = 0$, $\lim_{\mu\to 1} \sigma_c^2 = 0$, $\lim_{\mu\to\infty} \bar{c} = 2$ and $\lim_{\mu\to\infty} \sigma_c^2 = 0$. These limits represent the cases of isolated particles, $\lim \mu \to 1$, and of the chain lengths tending to infinity where all particles are in the body of a chain, $\lim \mu \to \infty$. Importantly, equation 4.7 tells us that there is a one-to-one relationship between the mean coordination number and the mean chain length such that knowledge of either allows the full statistics of the coordination number distribution to be calculated.

4.2.2 Disk formation

The theory may be extended to other cluster shapes such as disk–like aggregates. We propose the following simple scheme that mimics compact close-packed 2D clusters: we consider that clusters grow in hexagonal shells, filling each shell before proceeding to build the next. Figure

4.2 illustrates this idea. The final row of figure 4.2 shows a cluster of size s and indicates how successive shells of a cluster are filled in our simple model. The first particle is placed next to a corner of the previous shell and proceeds to fill first along the edge of the previous shell and wraps around each corner until the shell is complete.

	$P(0\|i;s)$	$P(1\|i;s)$	$P(2\|i;s)$	$P(3\|i;s)$	$P(4\|i;s)$	$P(5\|i;s)$	$P(6\|i;s)$	$P(c<6\|i;s)$
s=1 	1	0	0	0	0	0	0	0
s=2 	0	1	0	0	0	0	0	0
s=3 	0	0	1	0	0	0	0	0
s=4 	0	0	1/2	1/2	0	0	0	0
s=5 	0	0	2/5	2/5	1/5	0	0	0
s=6 	0	0	1/3	1/2	0	1/6	0	0
s=7 	0	0	0	6/7	0	0	1/7	0
s=8 	0	0	1/8	1/2	1/4	0	1/8	0
s=s 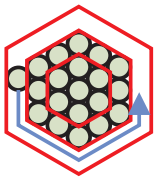	0	0	Algorithmically determined					0

Figure 4.2: Illustrations of clusters of different sizes, s, colour coded by their co-ordination number, c. For each cluster size the probability of finding a coordination number of 0 - 6 is given, $P(c|i;s)$. The final illustration is the general case of a cluster of size s.

We generate these clusters algorithmically and numerically evaluate equation 4.2 with the values of $P(c|i;s)$ determined from the generated clusters. In equation 4.2 the sum runs over all possible clusters $s = 1$ to ∞. This is not possible with algorithmically generated clusters; we can only compute this over a finite range. We generate clusters up to $s = 500$, significantly larger than any observed in our experiments. One would require a large mean cluster size before significant numbers of clusters of this size, or greater than this size, are expected to be observed.

4.3 Methods

4.3.1 Experimental methods

Chains: Here we use the experimental system outlined in the previous chapter, section 3.3. In summary, we use monodisperse paramagnetic spheres with a diameter of 3.0 μm . Dilute suspensions with packing fractions $\phi < 0.05$ are confined by gravity to a monolayer at the bottom of a quartz glass sample cell. Two solenoids, placed symmetrically either side of the sample are used to generate a uniform external magnetic field ranging from $B = 0 - 3.2$ mT, throughout the whole sample.

Disks: To achieve rotating magnetic fields we use two pairs of solenoids perpendicular to one another. Passing a current through each pair as a $\pi/2$ shifted sine wave gives a magnetic field vector of constant magnitude that rotates with a uniform frequency, ω. We will consider only one frequency and field strength here, this was chosen such that a particular phenomenon was observed - the growth of compact disk like clusters [30, 31]. We found that a frequency of $\omega = 0.1$ ms^{-1} and field strength of $B = 0.25$ mT generated clusters of this type that rotate at a slower frequency than the imposed frequency.

The cluster formation processes are captured using video-microscopy and analyzed with the methods outlined in section 2.4. In particular, for the chain formation we use intensity thresholding to identify particles and cluster, with a distance criteria to determine the coordination numbers of particles. Figure 4.3 shows snapshots of the system with a region expanded to show the results of this image analysis. For the disk formation, we use watershed thresholding to identify particles and a distance criteria to determine clusters and coordination numbers, figure 4.8.

4.3.2 Simulation methods

Molecular dynamics simulations[2] were done at the experimentally determined packing fraction with particles, confined to a plane, interacting via induced dipoles and through a short-range r^{-12} potential. The initial particle velocities are taken from a Maxwell-Boltzmann distribution.

[2]Simulations were performed by David Robinson, supervised by Professor Mark Wilson, Oxford University Physical and Theoretical Chemistry department.

Starting configurations are generated in two distinct ways. In the first, molecular dynamics simulations are performed in the fluid phase to generate 100 independent and random configurations each containing 200 particles. In the second, 100 independent configurations of 225 particles each are generated by displacing particles from an ideal square lattice with lattice spacing, a_0, by random two-dimensional vectors. The magnitudes of these vectors vary from zero, corresponding to the ideal lattice, to $\sim 0.2a_0$. At higher displacements the configurations resemble random configurations, whereas at low displacements a high degree of ordering is retained.

4.4 Results and discussion

4.4.1 Chain formation

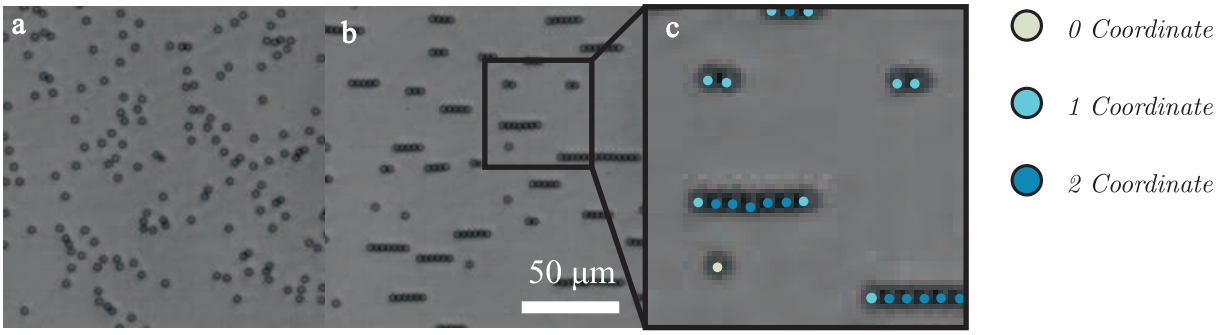

Figure 4.3: Images of the chaining process with the coordination numbers overplotted. (a) Initial configuration of a $\phi = 0.036$ sample. (b) The same sample 276 seconds after the application of a $B = 0.63$ mT magnetic field. (c) An expanded region of b showing the coordination numbers of particles.

From an initially random arrangement of particles, chains are formed due to the directional interaction of dipoles induced by an imposed magnetic field. This was investigated in the previous chapter and the physics is well documented in references therein. Figure 4.3 illustrates the process of particles coming together to form chain like aggregates under the action of a uniaxial magnetic field. A small region is enlarged showing the coordination numbers as determined by the image analysis methods outlined in section 2.4.

From the image analysis of snapshots we obtain cluster sizes at all times. In figure 4.4 we plot the cluster size distribution, $P(s)$, for all times. We observe a decay of probability; single particles are the most prevalent 'clusters' at all times and there is a monotonic decay of $P(s)$ as a function of s. This distribution is defined for the set $\{s : s \in \mathbb{N}^+\}$ as the smallest possible

clusters are single particles.

For a geometric distribution, equation 4.1, plotting $P(s/\mu)$ against s/μ rescales the distributions at different times to approximate the probability density function of the exponential distribution – the continuous analogue of the geometric distribution. As shown in figure 4.4a, we indeed find very good agreement between our experimental data, which is averaged over 25 different runs, and the exponential distribution at all times. Low values of $P(s/\mu)$ are only sampled by larger cluster sizes. Due to the limited field of view, and the observation time we only probe a range of mean cluster sizes. As such, the exponential distribution slightly overestimates the observed probability of low values of s/μ and, as a requirement of normalization, under-estimates the probability for intermediate values of s/μ.

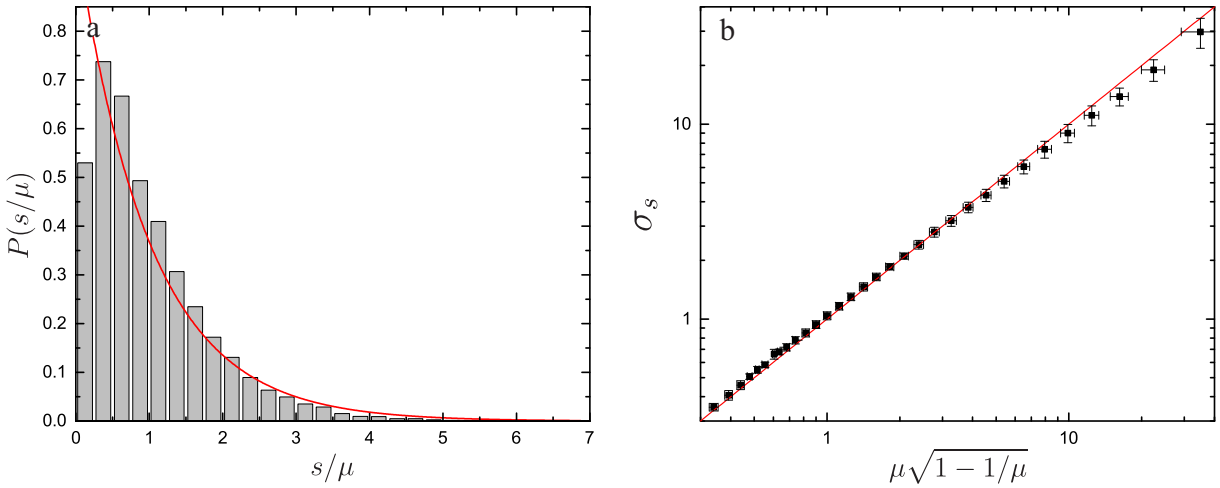

Figure 4.4: (a) The experimental probability distribution function for the cluster size $P(s/\mu)$ plotted as a function of s/μ. The solid line represents the exponential distribution, which is the continuous analogue of the geometric distribution, equation 4.1. (b) The standard deviation, σ_s, against $\mu\sqrt{1-1/\mu}$, a function of the mean of the chain length. The solid line represents the prediction of equation 4.1: $\sigma_s = \mu\sqrt{1-1/\mu}$, a straight line of gradient 1 in this plot.

Another powerful fingerprint of a geometric distribution is the interrelation of the mean and the standard deviation. From equation 4.1 it follows that $\sigma_s = \mu\sqrt{1-1/\mu}$. Figure 4.4b shows the variance of the chain lengths, σ_s, against the function of the mean chain length, $\mu\sqrt{1-1/\mu}$. This relation fits very well corroborating the applicability of the geometric distribution.

Next, we determine the fraction of particles with specific coordination numbers for our experiments and compare these with the theoretical predictions, equations 4.4 - 4.6. Figure 4.5a shows the fraction of particles with $c = 0, 1, 2$ and $c > 2$ as a function of the mean chain length μ. The agreement between the experiments and the predictions from equations 4.4 - 4.6

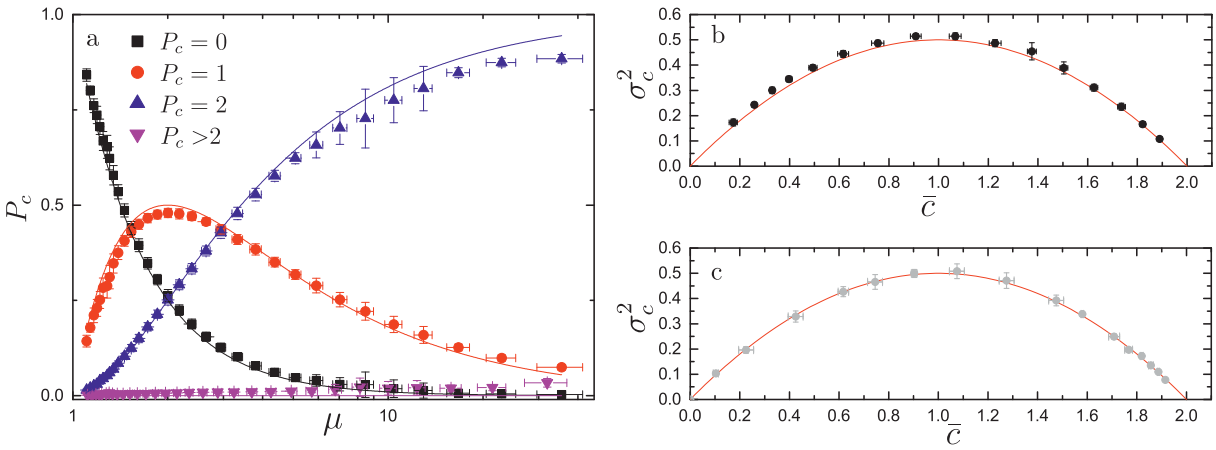

Figure 4.5: (a) The fraction of particles with coordination number c, P_c, for $c = 0, 1, 2$ and $c > 2$ as a function of the mean chain length μ. Closed symbols correspond to experiments; solid lines represent equations 4.4 - 4.6. (b) Variance of the coordination numbers, σ_c^2, plotted against the mean coordination number, $\bar{c}$, for the experimental results. (c) σ_c^2 plotted against $\bar{c}$ for the simulation results. In (b) and (c) the solid line is the prediction from equations 4.7 and 4.8: $\sigma_c^2 = \bar{c} - \bar{c}^2/2$.

is excellent for all mean cluster sizes. Only for larger mean cluster sizes, corresponding to later time, a small deviation becomes apparent. The deviation from theory at late times is due to the presence of a small fraction of particles with $c > 2$, which are not described in our model of simple linear chains. This assertion is confirmed by plotting the variance of the coordination number σ_c^2 against the mean coordination number $\bar{c}$ – but now neglecting the particles with $c > 2$ – alongside the theoretical prediction following from equations 4.7 and 4.8: $\sigma_c^2 = \bar{c} - \bar{c}^2/2$ (see figure 4.5b). Excellent agreement between experiment and theory is observed, especially given the fact that there are no fitting parameters. If the $c > 2$ particles are not removed the data points sit fractionally above the theoretical curve.

The computer simulation of the chain growth process, evaluated with a random starting configuration, shows the same coordination number statistics as in the experiments. This is confirmed by plotting $\sigma_c^2(c)$ as a function of $\bar{c}$, see Figure 4.5c. Importantly, this shows that our statistical model for cluster formation holds for both the colloidal (experimental) and atomistic (simulation) systems, despite the fact that the overdamped dynamics exhibited by the experimental system are very different from those of the simulation, where the presence of momentum leads to a qualitatively different growth process.

It is informative to note that the geometric distribution is the simplest distribution that arises from a classical compound Poisson process: Consider a sparse monolayer of particles with

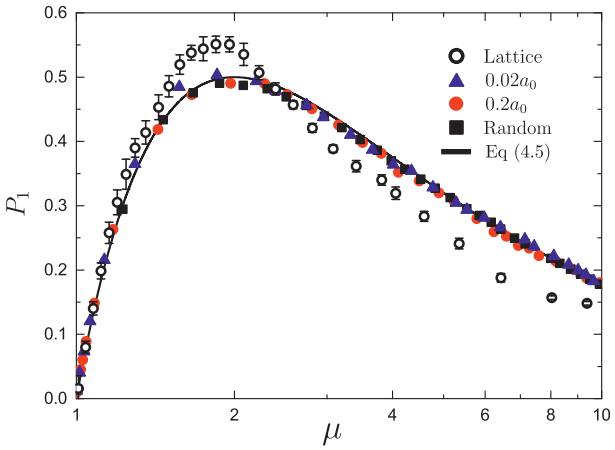

Figure 4.6: The fraction of particles with coordination number $c = 1$, P_1, as a function of the mean cluster size μ as obtained from the simulation for different degrees of ordering in the starting configuration, as characterised by the maximum initial displacement from the lattice sites in units of the ideal lattice spacing, a_0. Also shown are data corresponding to a random starting configuration and the solid line shows the predicted result from equation 4.5.

locations independent of all others particles. Segmenting the plane into sections of equal areas, each section will contain a random number of particles according to a Poisson distribution [140]. Upon the application of a magnetic field at $t = 0$, particles instantaneously start to associate with nearby particles to form short chains, with a distribution of lengths determined by the number of particles in its local area - a Poisson distribution of particles. Subsequently, these short chains combine with each other into longer chains. Importantly, chains are randomly distributed in space at all times so the number of subsequent aggregation events is also determined by a Poisson process. From this we would conclude that the chain length distribution for the overall chain length arises from a classical compound Poisson process, a cascade of subsequent Poisson events. The simplest example of this is the geometric distribution, making it a likely candidate distribution [141].

This model is not an exact description of our system: it implies a stronger separation of the growth process, namely a clear initial aggregation stage separated in time from subsequent aggregation events, each independent of the last. For the experimental growth process, the clustering is a continuous process. However, a compound Poisson interpretation highlights a key concept: the length of a chain is derived from a random number of aggregation events of clusters of random length, which is entwined with the initial spatial distribution of particles. As such it should be possible to violate this and alter the growth process by ordering the particles before a magnetic field is applied. This is difficult to achieve experimentally [142] but is simpler

to achieve in the simulations outlined in sec 4.3.2.

The simulations allow us to reveal how the chains grow according to a compound Poisson process, and hence how the resulting coordination number statistics is affected by the initial configuration. The solid line in figure 4.6 shows the probability of coordination number 1 as given by equation 4.5 along with simulation data associated with different degrees of ordering of the initial particle positions. Clearly a deviation from the compound Poisson process is seen for increasingly ordered starting configurations. Particles starting from a perfectly ordered lattice have a tendency to 'pair up' and the doublets that result still have a large degree of ordering and can thus pair up again. This explains both the observed excess of P_1 around $\mu = 2$, and its subsequent deficit for $\mu > 2.5$, relative to the compound Poisson prediction; the difference being a consequence of a more uniform chain length distribution than that arising from our compound Poisson process. We note that already a small amount of disorder in the initial particle positions significantly interferes with the pairing process observed for perfect lattice and hence randomises the configuration very rapidly, leading to a distribution of chain lengths. As a result, the compound Poisson process is recovered very rapidly for increasing amounts of disorder in the starting configuration and as the mean chain length increases.

Finally, we show how the coordination number statistics can be probed in the time domain, which is the natural 'reaction coordinate' when studying cluster formation. By using the time dependence of the mean cluster size given in section 3.4 as $\mu = a + bt^{*^{z'}}$, with $a = 1.12$, $b = 3.1 \cdot 10^4$, $z' = 0.61$ and $t^* = \phi^{2.44} B^{1.61} t$ [143], we can directly convert the dependence of P_c on μ into a time dependence for any ϕ and B. We illustrate this in figure 4.7*a*, where we show P_0, P_1 and P_2 as a function of time for three different combinations of ϕ and B alongside the theoretical prediction. The corresponding snapshots at $t = 500$ s are shown in figure 4.7*b–d*. As expected the sample with the highest packing fraction ($\phi = 0.024$) and at the highest magnetic field ($B = 1.88$ mT) exhibits the fastest aggregation, while the sample at $\phi = 0.013$ and $B = 0.63$ mT shows the slowest chain formation. The sample at $\phi = 0.013$ and $B = 1.88$ mT is an intermediate case with the same concentration as the slowest case and the same field as the fastest case. This shows that increasing either ϕ or B independently has the expected effect.

Excellent agreement between experiments and theory is observed, figure 4.7, which implies that our statistical description holds, regardless of whether the packing fraction or the magnetic

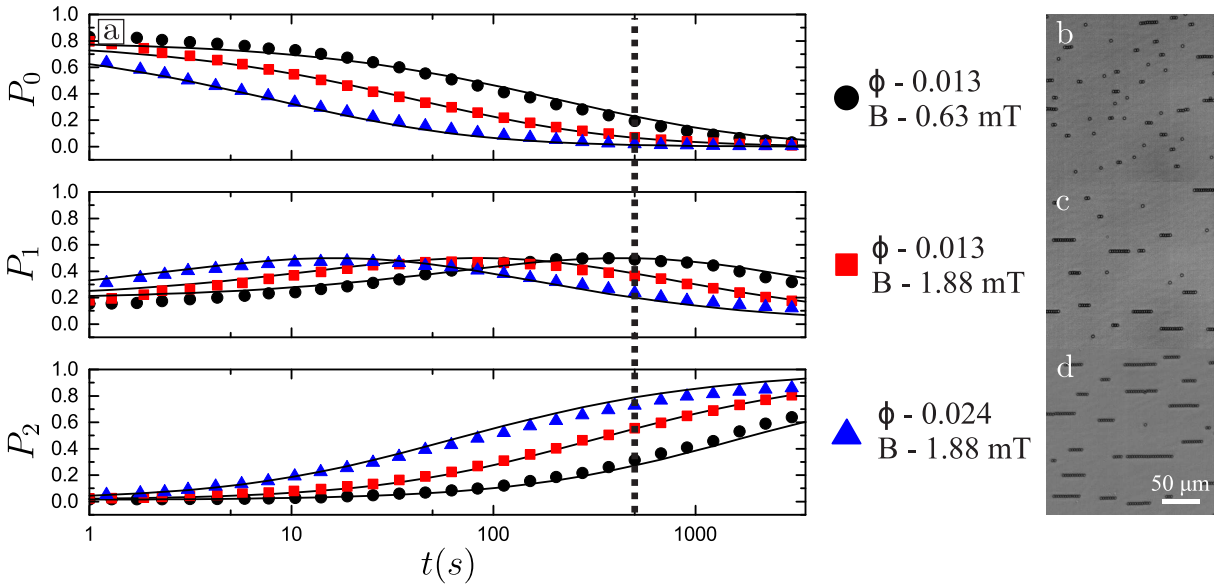

Figure 4.7: (a) The time evolution of P_0, P_1 and P_2 for three samples, each with a different combination of packing fraction ϕ and magnetic field B, as indicated below the panel. (b–d) Snapshots corresponding to these three experimental systems at $t = 500$ s, as indicated by the dashed line in panel (a).

field is varied. This shows that the model of clusters as straight chains is good for the range of packing fraction and fields investigated and that the cluster size distribution of particles is geometric in this range. This further confirms that the coordination number distribution fully characterises the chain length distribution at all times and *vice versa*.

The accurate description of the cluster size distribution as a shifted geometric greatly simplifies the theoretical modeling of these systems. At higher concentrations the geometric distribution is not predicted. Numerical analysis of Smoluchowski kinetic equations shows that as lateral aggregation becomes more important deviations from a geometric distribution will be observed, altering $P(s)$ [87, 90, 144].

4.4.2 Disk formation

Next, we consider aggregation induced by a rotating magnetic field [30–32, 86, 100, 109, 110, 145]. We limit ourselves to a single concentration, frequency and field strength, as discussed in section 4.3.1. Figure 4.8 shows a sample of clusters that result from applying fields as outlined in section 4.3.1. Qualitatively, clusters tend to be compact close packings of particles [30, 31]. In a static field particles tend to aggregate in line with the imposed magnetic field, minimizing

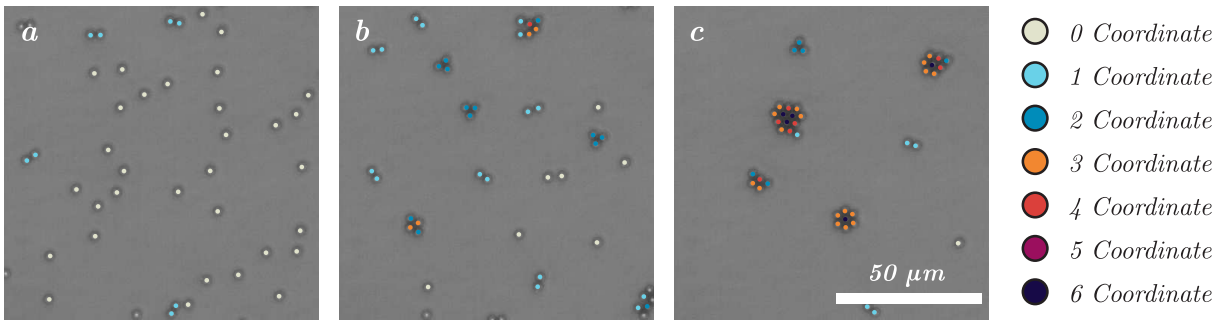

Figure 4.8: Images of the clustering process of particles in a rotating field with the coordination numbers overplotted. (a) Initial configuration of a $\phi = 0.05$ sample. (b) The same sample 60 seconds after the application of a $B = 0.25$ mT magnetic field rotating with a frequency $\omega = 100$ s^{-1}. (c) 600 seconds after the initial application of the magnetic field.

their potential energy. Here, particles form islands that rotate with a frequency lower than the imposed frequency [30].

By inspection, the clusters in figure 4.8 are consistent with those presented in the schematic in figure 4.2, outlined in the theory section 4.2.2. For example, clusters of 7 particles tend to form a hexagon with the addition of more particles starting a new shell, figure 4.8*c*. The simple scheme for disk like structures, section 4.2, does not incorporate the possibility of clusters of the same size having different shapes [146]. Small clusters, $s < 4$, adopt both chain structures and compact structures. These account for a small fraction of all particles and the impact is not expected to be large.

In figure 4.9*a* we show the mean cluster size as a function of time and observe that clusters grow monotonically with time. We find that the growth follows the power law $\mu = 1.1{+}0.008t^{0.83}$, consistent with previous observations [100]. The cluster size distribution at a time $t = 1318$ s after the application of a magnetic field is shown in figure 4.9*b*. A shifted geometric distribution of the same mean, $\mu = 4.91$, is also plotted in red, showing excellent agreement over the range of cluster sizes. In the inset of figure 4.9*b*, we further confirm that the cluster size distribution is a shifted geometric distribution at all times by plotting σ_s against $\mu\sqrt{1-1/\mu}$, equation 4.1.

The evolution of the fraction of particles with coordination numbers in the range $c = 0-6$ is shown in figure 4.10*a* as a function of mean cluster size, and as a function of time. The coordination numbers predicted from our statistical theory are also shown. In general there is good agreement between theory and experiment. Zero coordination particles are described well at all mean cluster sizes. At early times, we see a small excess of 1 coordination particles

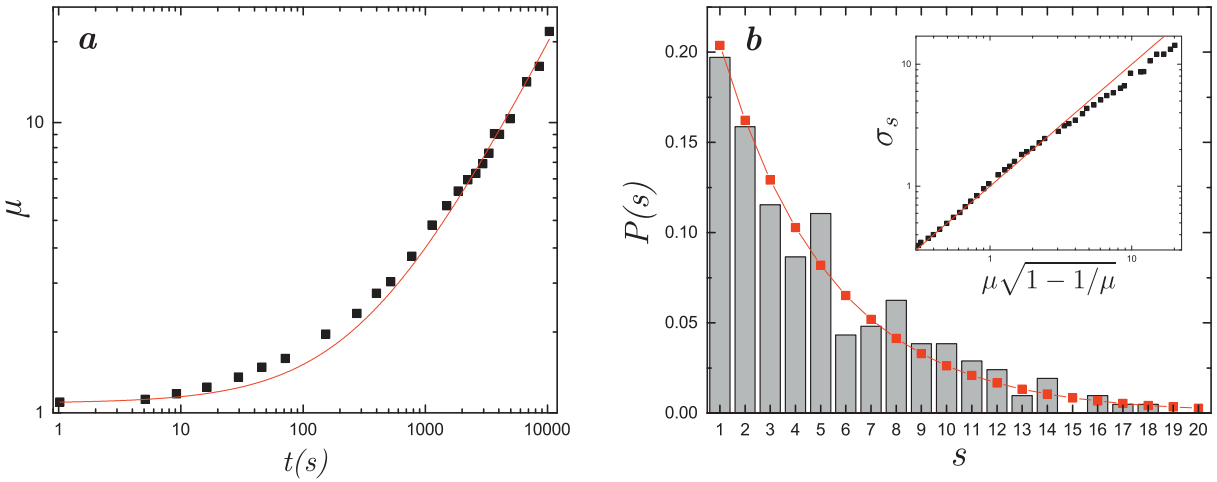

Figure 4.9: (a) The mean cluster size as a function of time, the red line represents the power law fit $\mu = 1.1 + 0.008t^{0.83}$. (b) The cluster size distribution at time $t = 1318$s with the shifted geometric distribution, $\mu = 4.91$, shown. The inset shows the standard deviation, σ_s, against $\mu\sqrt{1-1/\mu}$, a function of the mean chain length. The solid line represents the prediction of equation 4.1 : $\sigma_s = \mu\sqrt{1-1/\mu}$

and a corresponding deficit of 2 and 3 coordination particles. This deviation is due to the tendency for particles to still adopt chain like structures, as opposed to close packings. At late times, we observe a slight over estimation of the number of 6 coordination particles; cluster re-arrangements transiently break the close packing of clusters reducing the average number of 6 coordination particles.

To summarise the data presented in figure 4.10*a*, we plot the mean coordination number against the standard deviation of the coordination numbers in figure 4.10. Excellent agreement is seen between theory and experiment for all coordination number confirming that our model captures the key structural properties of the clustering process.

4.5 Conclusions

We have developed a direct relation between the coordination number statistics and the mean cluster size using simple statistical considerations. We confirm our model on a chain forming experimental model system of paramagnetic colloidal particles in an external magnetic field. Our approach has been confirmed by atomistic computer simulations by systematically varying the starting configuration, affecting the nature of the chain formation process, indicating a compound Poisson like process in the experiments. Our results imply that the coordination

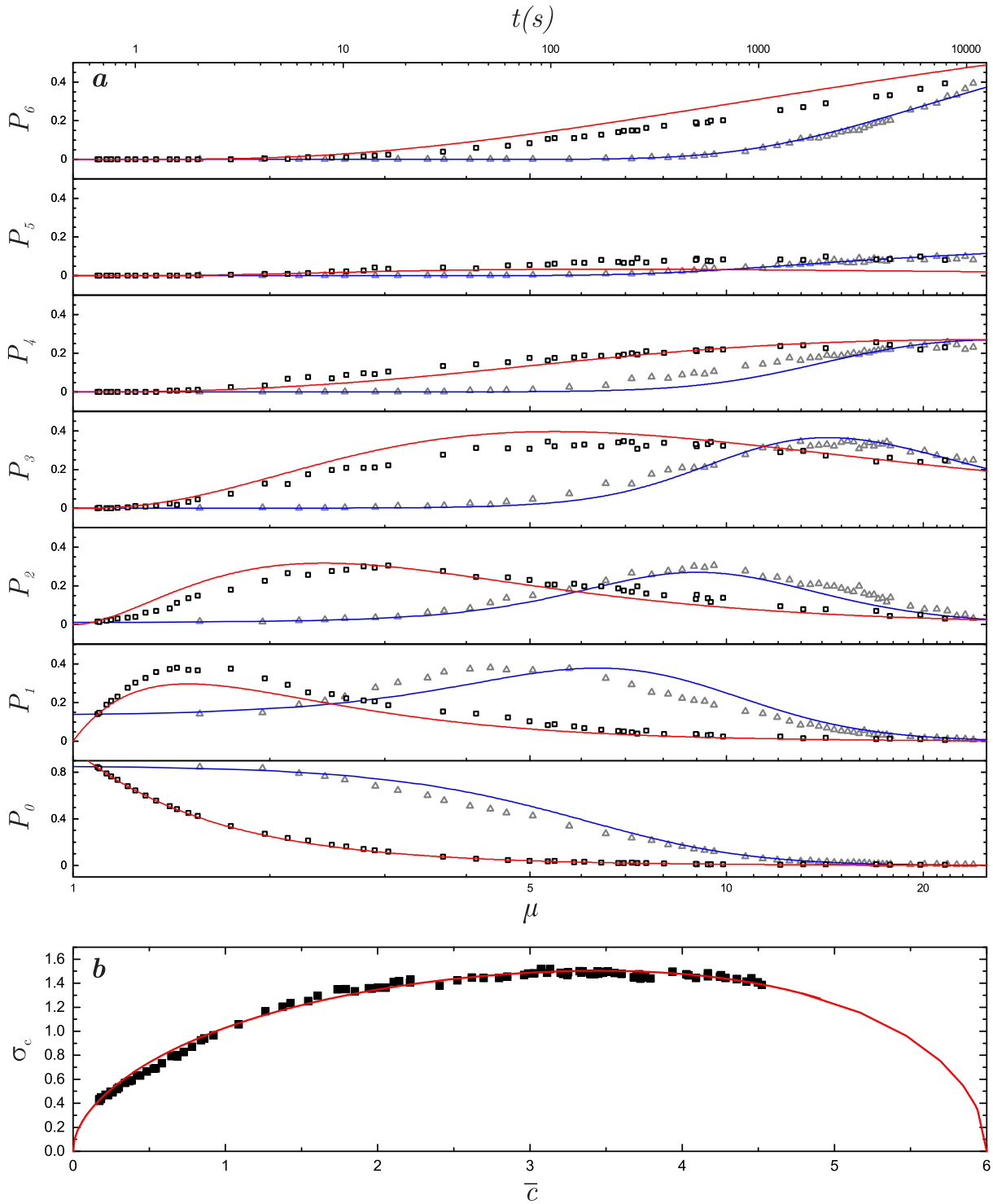

Figure 4.10: (a) Graphs of the fraction of particles with a particular coordination number as a function of μ, black squares, and time t, grey triangles. Solid lines correspond to the theoretical curves in time, blue, and in mean cluster size, red. See text for details. (b) σ_c against $\bar{c}$, the solid line represents the result of our statistical analysis. To extend the curve to higher mean coordination numbers, 25000 possible clusters where considered.

number distribution fully characterises the cluster size distribution and *vice versa* at all times. Our probabilistic approach of analysing cluster formation through coordination number statistics is applicable to more complex systems, such as the 2D disk that we have demonstrated, and provides a general geometric perspective on self-assembly.

Acknowledgements

This work was carried out in collaboration with William Sampson, David Robinson, and Mark Wilson. In particular, the simulations were performed by David Robinson, supervised by Mark Wilson.

Chapter 5

Coarsening dynamics and structural properties of magnetorheological networks

ABSTRACT

In this chapter, we investigate the structural properties of magnetorheological networks. The size distributions, orientational ordering and spatial distribution of the void phase is investigated and compared to random fiber theory. In the fiber phase, the segment length distribution is characterised, as well as the distributions of fiber widths and orientations. These network properties are interrelated such that the entire growth process of fibrous networks can be summarised in terms of a single length scale. We follow the evolution of this length scale in time for a range of fields and concentrations, investigating the dynamics of the network coarsening and its dependence on magnetic field strength and surface coverage.

5.1 Introduction

Fibrous networks are of great general importance and have found myriad applications in filtration, composite materials, catalysis as well as biomedical applications [40–45]. Paper is another well known example in which fibers are deposited from a suspension generating random networks.

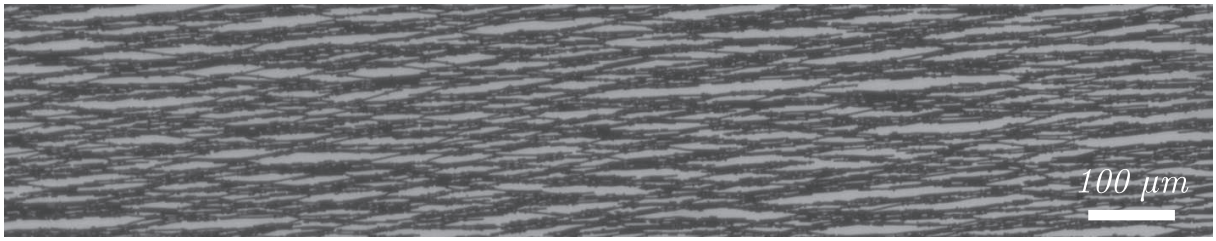

Figure 5.1: Microscopy image showing the percolating network of paramagnetic particles that results from applying a magnetic field. The snapshot is 30 s after the application of a 1.88 mT magnetic field to a sample of particles with a surface coverage of $\phi = 0.63$.

System spanning networks of particles formed due to induced anisotropic interactions have also been observed in both electrorheological and magnetorheological systems [33, 34]. In two dimensions, at surface fractions greater than $\phi = 0.3$ percolating networks of paramagnetic particles are formed when a constant magnetic field is applied [22]. An image of such a network is shown in figure 5.1, note that this is a kinetically arrested state. The thermodynamic state can only be accessed with pulsed fields that allow the structure to rearrange into the minimum energy structure [35–39].

A range of methods have been used to study these structures including, simulations, light scattering, ultrasonic propagation, conductance, optical transmittance and optical microscopy, mostly in three dimensions [88,116,147–154]. A detailed understanding of the mesoscopic structure in two dimensions remains an open question. The structural properties of random networks can be described by the theory of stochastic fibrous networks [155–158]. In this chapter we will investigate the extent to which these model random networks resemble networks of paramagnetic particles and highlight the differences between them.

In this chapter we elaborate on the structural distributions of particle networks in two dimensions and investigate the magnetic field dependence and the surface coverage dependence of network formation. We will first introduce random fibrous networks, a model system to which we compare our experimental system, section 5.2.1. We then outline the experimental methods used, section 5.3.1, and new image analysis methods needed to quantify stochastic networks of particles, section 5.3.2. In section 5.4.1 we report the distributions of network properties for a range of surface coverages and magnetic fields. We then probe how these properties are related to each other, section 5.4.3. We then report on the coarsening dynamics of two dimensional magnetorheological networks in terms of the mean void area, section 5.4.4.

5.2 Theory

The theory of stochastic random fibrous networks is introduced. Some of the key structural properties are derived and the effects of introducing orientational order are described.

5.2.1 Stochastic fibrous networks

The archetypal random fiber networks are constructed with fibers (rigid rectangles of fixed length, l, and width, ω) obeying three criteria [155]:

1. fibers are positioned independently of each other;
2. the fibers have a uniform probability of being deposited at any point;
3. and the fibers have an equal probability of making all possible angles relative to an arbitrary fixed reference axis.

The properties of random fibrous networks networks are well documented and many structural properties of networks obeying these rules may be derived mathematically. We will outline here some key results following the work of W. W. Sampson [158].

Consider two fibers, of length l and width ω, being placed at random in a unit square with the fibers forming an angle ϕ relative to each other. The probability of two fibers forming a relative angle ϕ is uniform with the probability density function (pdf) $P(\phi) = 1/\pi$, $0 \leq \phi < \pi$. Having placed one fiber, there is a chance that a subsequent fiber will overlap with the first when being placed, $P(\text{cross})$. The probability of this is given by the ratio of the area of the parallelogram illustrated in figure 5.2*a* and the total area of the square, defined with sides of unit length. The parallelogram is centered on the first fiber and has sides of length l and an interior angle of ϕ. It follows that the probability of two fibers crossing is given by:

$$P(\text{cross}) = \int_0^\pi P(\text{cross}|\phi)P(\phi)d\phi = \int_0^\pi \frac{l^2 \sin\phi}{\pi} d\phi = \frac{2l^2}{\pi}, \tag{5.1}$$

where $P(\text{cross}|\phi)$ is the probability of crossing given that a particular relative angle has been formed. Note, this is dimensionless due to the division by the area of the square, defined with sides of unit length.

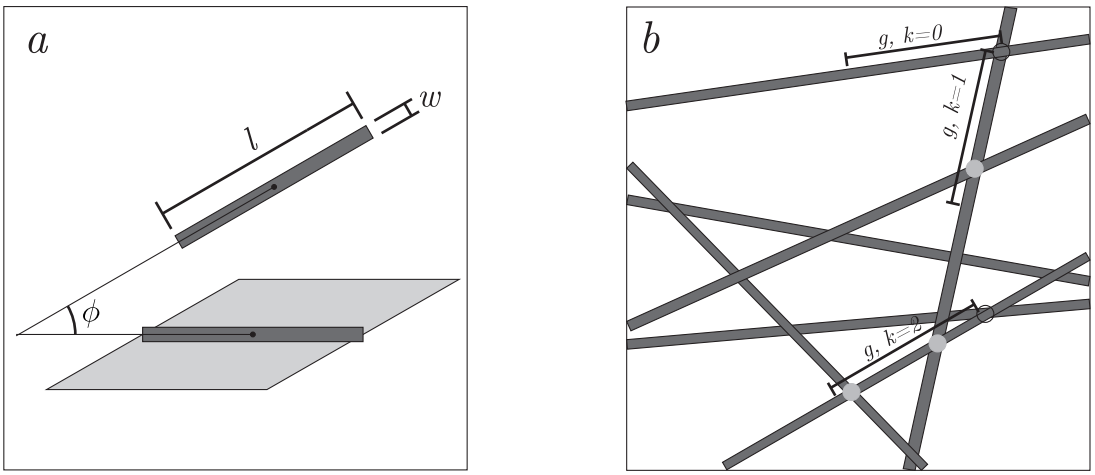

Figure 5.2: (a) Two fibers of length l and width ω with a relative angle ϕ. Around the horizontal fiber is a parallelogram with sides of length l and an angle of ϕ, it represents the area from which the center of the second fiber is excluded if the fibers are to not intersect. (b) A network of several fibers intersecting with a selection of intervals of the same length g containing different numbers of crossings, k.

If there are n_{fiber} fibers per unit area, the number of possible crossings is approximately $\frac{1}{2}n_{\text{fiber}}^2$. The expected number of crossings per unit area, n_{cross}, is then the product of the number of possible crossings and the probability that a crossing occurs such that

$$n_{\text{cross}} = \frac{n_{\text{fiber}}^2 l^2}{\pi} = \frac{c^2}{\pi\omega^2}, \tag{5.2}$$

where c is the coverage, the average number of fibers covering a given point, given by $c = wln_{\text{fiber}}$. The crossings per fiber is given by $n_{\text{cross/fiber}} = 2n_{\text{cross}}/n_{\text{fiber}} = 2lc/\pi\omega$. A fiber of length l subdivided this many times will result in segments with a typical length, $\bar{g}$, given by

$$\bar{g} = \frac{l}{n_{\text{cross/fiber}}} = \frac{\pi\omega}{2c}. \tag{5.3}$$

Assuming crossings are independent random events; the number of crossings, k, within an interval of length g is governed by a Poisson distribution with mean $\mu = g/\bar{g}$:

$$P(k) = \frac{e^{-\mu}\mu^k}{k!}. \tag{5.4}$$

The probability that no crossings occur in an interval g is $P(k=0) = e^{-\mu}$. If we consider intervals that have at one end an intersection we find that $1-P(k=0)$ represents the cumulative

probability distribution of segment lengths, figure 5.2*b*. The pdf of segment lengths, $P(g)$, is therefore given by:

$$P(g) = \frac{1}{\bar{g}} e^{-\frac{g}{\bar{g}}}, \tag{5.5}$$

an exponential distribution with mean $\bar{g}$, variance $\bar{g}^2$, and coefficient of variation 1. The coefficient of variation, cv, is the ratio of the standard deviation and the mean, $cv_g = \sigma_g/\bar{g} = 1$. We note that the exponential distribution is a special case of the gamma distribution,

$$P(x) = \frac{\left(\frac{\beta}{\alpha}\right)^{-\alpha} x^{\alpha-1} e^{-\frac{\alpha x}{\beta}}}{\Gamma(\alpha)}, \tag{5.6}$$

which has a mean β, variance β^2/α, and coefficient of variation $1/\sqrt{\alpha}$. Γ is the gamma function. We use the gamma distribution to investigate correlations in the intersections of fibers. Relative to $\alpha = 1$, which we call the random limit, $\alpha > 1$ probes flocculated intersections, $\alpha < 1$ dispersed intersections. In the flocculated limit the intersection points on a fiber exhibit some degree of clumping, and in the dispersed limit they tend to spread themselves more evenly. In the limit that $\alpha = 1$ the gamma distribution reduces to the exponential in equation 5.5 that results from fibers placed independently of each other. For generality, we will continue the theory using the gamma distribution, equation 5.6, and note that when $\alpha = 1$ and $\beta = \bar{g}$ we recover the random limit.

The intervals between crossings define the perimeters of voids; the distribution of void sizes follows from the distribution of segment lengths (equation 5.6). The probability distribution for the area of voids, $P(a)$, described by rectangles with sides independently drawn from the segment length distribution, such that $a = g_x g_y$, is given by:

$$P(a) = \int_0^\infty P(g_x)P(g_y)dg_x = \frac{2a^{\alpha-1}\left(\frac{\alpha}{\beta}\right)^{2\alpha} K_0\left(\frac{2\sqrt{a}\alpha}{\beta}\right)}{\Gamma(\alpha)^2}. \tag{5.7}$$

This has a mean $\bar{a} = \bar{g}^2$, variance $\sigma_a^2 = 3\bar{g}^4$, and coefficient of variation $cv_a = \sqrt{3}$ in the random limit of $\alpha = 1$. K_0 is the zeroth order modified Bessel function of the second kind. Equation 5.7 is well approximated by a gamma distribution, equation 5.6, with the same coefficient of variation. A comparison of the two distributions is given in figure 5.3. The gamma distribution has been found to accurately model the void space in several physical systems, such as as the

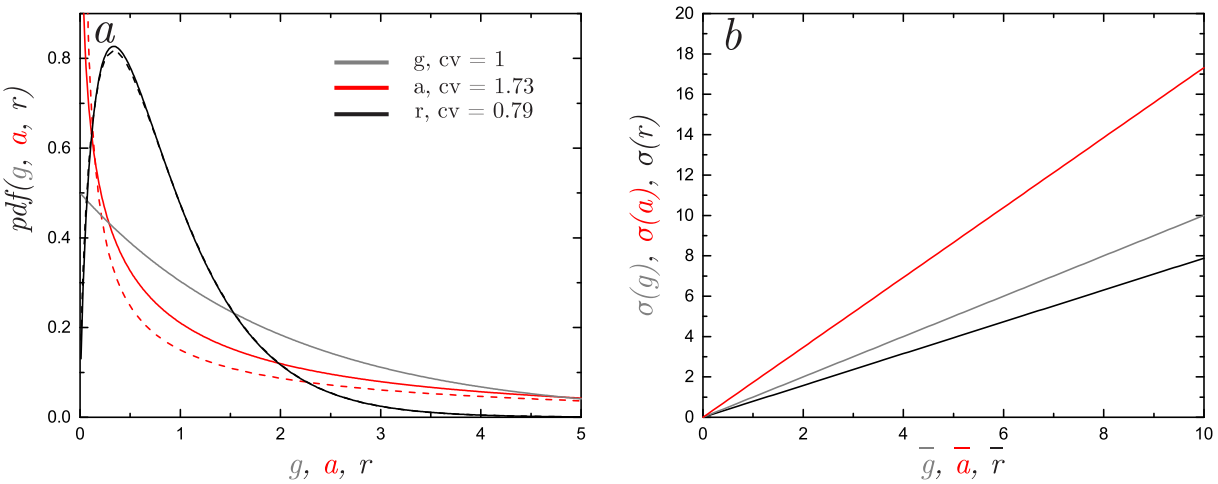

Figure 5.3: (a) The theoretical probability density functions for the segment length (g, grey), the void area (a, red), and the void radius (r, black). The solid lines represents the theoretical predictions in the random limit, the dashed lines are gamma distribution with equivalent coefficients of variation. All the distribution presented have a mean of 1. (b) The mean vs the standard deviation of the distributions presented in a, all are straight lines with a gradient defined by the coefficient of variation.

voids of sandstone and in a range soils, reinforcing its use here as a candidate distribution for the void size distributions or a percolating network [159, 160].

Finally, we consider the probability distribution of the radii of circles with the same areas as the voids that we have just derived, $P(r)$, with $r = \sqrt{a/\pi}$. We find this with a suitable change of variables

$$P(r) = \frac{da}{dr}P(a) = \frac{4\pi^{\alpha}\left(\frac{\alpha r}{\beta}\right)^{2\alpha} K_0\left(\frac{2\sqrt{\pi}r\alpha}{\beta}\right)}{r\Gamma(\alpha)^2}, \tag{5.8}$$

such that the mean is $\bar{r} = \bar{g}\sqrt{\pi}/4$, the variance is $\sigma_r^2 = \bar{g}^2(1/\pi - \pi/16)$, and the coefficient of variation is $\sigma_r/\bar{r} = (16 - \pi^2)^{1/2}/\pi = 0.79$. As before, the coefficient of variation is independent of the mean, indicative of a gamma distribution which is found to be an excellent approximation of equation 5.8, figure 5.3a.

The probability densities of the segment length distribution, equation 5.5, void area distribution, equation 5.7, and the void radius distribution, equation 5.8, are plotted in figure 5.3 along with their approximating gamma distributions, equation 5.6. A table summarising the expected distributions of key properties of a random fibrous network is given in table 5.1. In addition to the unweighted mean, variance, and coefficient of variation, we also include the area

Property	Distribution	Mean	Variance	Unweighted cv	Area-weighted cv
Segment Length	Exponential*	$\bar{g}$	$\bar{g}^2$	1	n/a
Segment Width	Constant	ω	0	0	n/a
Void Area	Gamma	$\bar{g}^2$	$3\bar{g}^4$	$\sqrt{3} \approx 1.73$	1.18
Void Radius	Gamma	$\frac{\bar{g}\sqrt{\pi}}{4}$	$\bar{g}^2 \left(\frac{16-\pi^2}{16\pi}\right)$	$\frac{(16-\pi^2)}{\pi} \approx 0.788$	0.53

Table 5.1: A summary of the distributions and key interrelations that result from random fiber theory. * Note: the exponential is a special case of the gamma distribution.

weighted coefficients of variation, as it turns out that all of these values are experimentally relevant.

In addition to the random network system outlined above, stochastic deviations to the orientation of fibres may also be investigated. In equation 5.1, we used a uniform probability distribution for the probability distribution of relative angles. To model a preferential orientation of fibers, fibers are considered to have a peaked distribution of angles relative to a fixed reference axis. The one parameter cosine distribution is a common candidate:

$$P(\theta) = \frac{1}{\pi} - \epsilon \cos(2\theta), \tag{5.9}$$

where ϵ is a pre-factor that encapsulates the degree of orientation ordering: increasing ϵ decreases the variance. The one parameter cosine distribution, defined in the range $0 < \theta < \pi$, can only handle a range of $0 < \epsilon < 1/\pi$, limiting the degree of orientational ordering it can model. In spite of this, it is still informative to consider the influence of ordering fibers in this way. It is often used in the place of other distributions, such as the Von Mises (equation 5.12), which would require numerical treatment but do not substantially alter the inferences we can make on the influence of ordering fibers [158].

Using the one parameter cosine distribution, the expected number of crossings per unit area becomes

$$n_{\text{cross}} = \frac{c^2}{\pi\omega^2} - \frac{c^2\pi\epsilon}{6\omega^2}. \tag{5.10}$$

The crossings per fiber follows, as before, as $n_{\text{cross/fiber}} = 2n_{\text{cross}}/n_{\text{fiber}} = cl(6-\pi^2\epsilon^2)/3\pi\omega$. This has a corresponding influence on the mean distance between inter-fiber crossings such that the

mean segment length is given by

$$\bar{g} = \frac{\pi\omega}{2c(1-\frac{\pi^2\epsilon^2}{6})} - \frac{8\omega}{3\pi(1+\frac{2}{-6+\pi^2\epsilon^2})}, \tag{5.11}$$

indicating that increased orientational ordering leads to longer mean segment lengths, which has a knock-on effect on the mean void area and radii, equation 5.7. The crossings of oriented fibers, like the crossings of uniformly oriented fibers, are a point Poisson process in the plane. It follows that the segment length distribution in a network of oriented fibers is exponentially distributed. The void distribution follows from the segment length distribution, as before for uniformly oriented fibers (equation 5.7), and a Gamma distribution with $cv = 1.73$ is expected. Experimentally, the similarity of orientated and un-oriented fibers has been corroborated with simulations of fibrous networks exhibiting the same distributions of inscribed circles in both cases [161].

Experimentally we will find that voids and segments are more strongly orientated than can be captured by the one parameter cosine distribution. We will compare both the void orientation distribution and segment orientation distribution to the Von Mises distribution centered around $\bar{\theta} = 0$. The Von Mises probability density function, defined for $-\pi < 2\theta < \pi$, with a mean orientation $\bar{\theta} = 0$, is defined by:

$$P(\theta) = \frac{e^{\epsilon_{\text{vm}}\cos(2\theta)}}{\pi I_0(\epsilon)}. \tag{5.12}$$

It has a mean of 0, and a one-to-one relationship between ϵ_{vm} and the variance, which captures the degree of orientational ordering. Here I_0 is the zeroth order modified Bessel function of the first kind.

Throughout this theory section we have implicitly assumed that the length of fibers, l, is much larger than both the width, ω, and the typical inter-crossing distance, $\bar{g}$. The limit of this is a line process in which fibers are infinitely long and thin [158]. Figure 5.4 shows images of simulated infinite line processes and illustrates the effects of systematically varying the number of fibers, the degree of orientational ordering, and the thickness of fibers. In panels *a-c*, there is no preferred orientation and we show the effects of varying the number of fibers. Panels *d-f* show the effects of increased ordering, voids become elongated as the order increases left to right. Panels *g-i* show the effect of increasing the width of fibers, small voids are filled in as larger

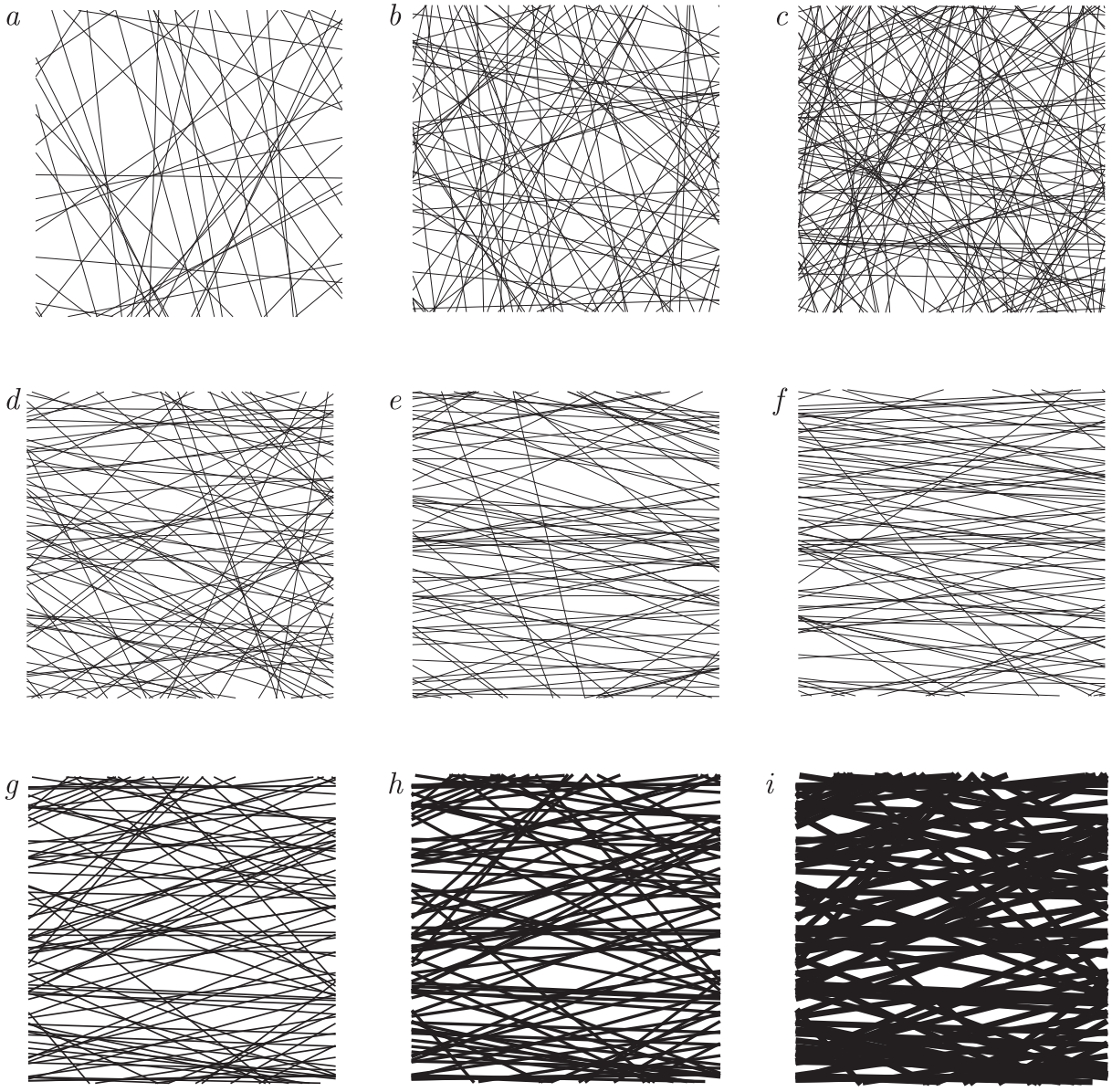

Figure 5.4: Simulated stochastic fibrous networks. (*a-c*) a uniform angular probability is used with fibers of a fixed width 0.0025 while the number of fibers is 50, 100 and 150 respectively. (*d-f*) 100 fibers with a fixed width 0.0025 are generated with a Von Mises distributed angle relative to the x axis such that the standard deviation is expected to be 0.63, 0.33 and 0.23 respectively. (*g-i*) 100 fibers drawn from the same angular distribution, with standard deviation 0.33, are generated with widths of 0.005, 0.01 and 0.02 respectively. The plotting area for each is a unit square and widths are given in terms of fractions of this arbitrary unit.

voids shrink - the distribution is not expected to be affected by this [162].

5.3 Methods

5.3.1 Experimental methods

In this chapter we use the same experimental system as we have done in the previous chapters, outlined in section 2. In summary, we use monodisperse paramagnetic spheres with a diameter of 3.0 μm (Dynabeads®, Life Technologies). Concentrated suspensions with packing fractions $0.4 < \phi < 0.8$ are confined by gravity to a monolayer at the bottom of a quartz glass sample cell. A uniform external magnetic field ranging from $B = 0 - 3.2$ mT is applied throughout the whole sample. The subsequent network formation is captured using video-microscopy and analysed with the methods outlined in section 5.3.2.

In this chapter we use a 4× magnification objective, which is lower than was used in the previous chapters. Single particle detection is not possible at these magnifications as the typical radius of a particle is ~ 1 pixel, so only larger structures can be observed. We measure the properties of voids, the area between connected regions of particles, and the fiber phase, the contiguous region of particles.

5.3.2 Image analysis of networks

We extract quantitative measures of the structural properties of the networks from digital images using novel image analysis algorithms. Particles appear as dark regions when viewed with brightfield microscopy with bright ellipsoid like structures, voids, spread throughout the particle's fiber phase. Figure 5.1, shows an example image. We introduce here the image analysis algorithms we use to extract the dimensions, positions and orientations of voids, and the lengths, widths and angles of representative segments of the fiber phase.

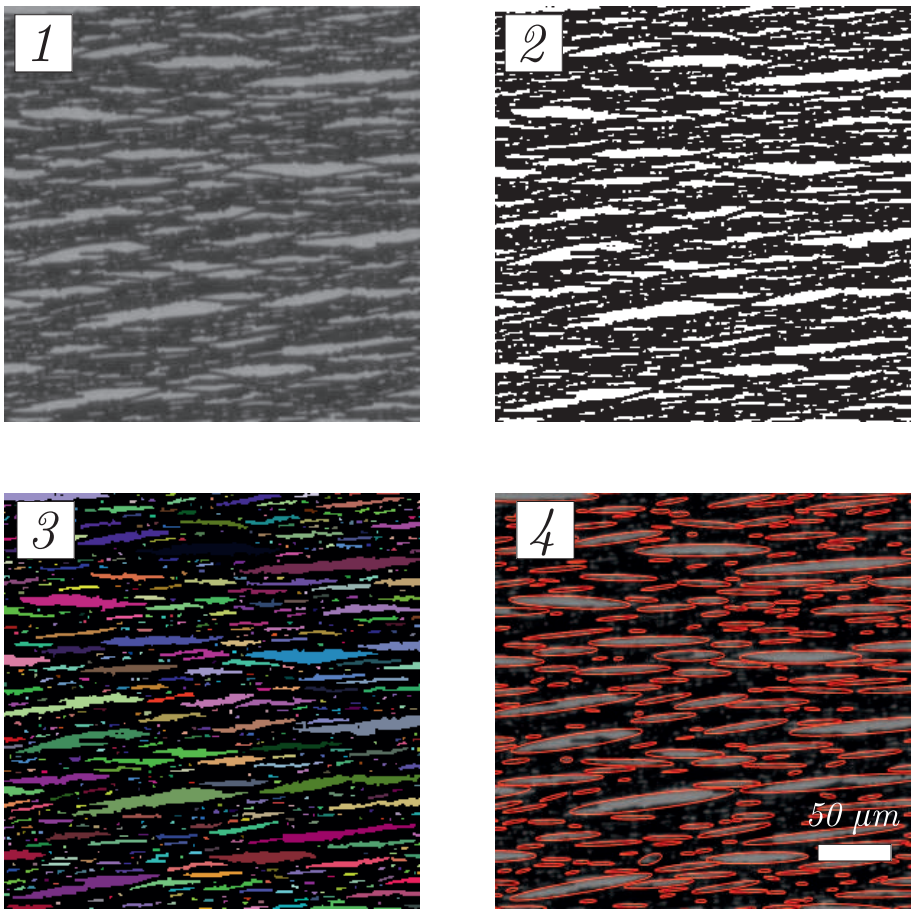

Figure 5.5: (1-4) show the stages of the void phase image analysis algorithm, see text for details.

Void phase image analysis

Figure 5.5 illustrates the image analysis process we use to identify voids, continuous areas free from particles. Voids are segmented by an intensity threshold, reducing the image to a binary image in which the voids are connected regions of white pixels, figure 5.5(2). The voids can then be identified with standard morphological transforms, figure 5.5(3). These components are fitted with an oriented best fitting ellipse, giving an angle and two orthogonal length scales. We take the number of pixels in a component to be a measure of the area. In figure 5.5(4) we plot the ellipses identified by this analysis, for clarity only voids sampled by more than 10 pixels are shown.

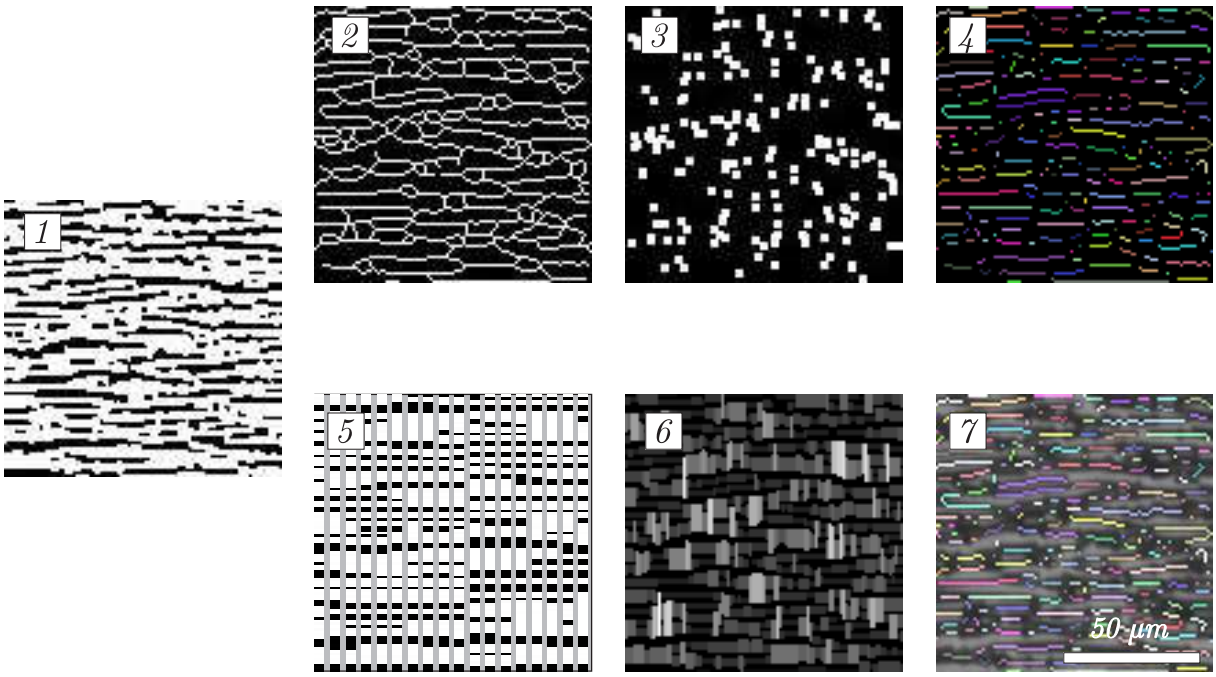

Figure 5.6: (1-7) show the stages of the fiber phase image analysis algorithm, see text for details.

Fiber phase image analysis

We quantify the fiber phase, the system spanning network of particles, as a set of representative segments. We define these to be the set of points between branching points in a morphological thinning of a binary image. First, we segment an image using an intensity threshold, figure 5.6(1). To this binary image we apply a morphological thinning transform, successive erosions until convergence is achieved, resulting in a skeleton image, figure 5.6(2). The branching points of the skeleton image are identified with inbuilt Mathematica routines, figure 5.6(3), and subtracted from the morphological thinning. This results in isolated groups of pixels that can be identified as representative segments using morphological transforms, figure 5.6(4).

So far in this analysis of the fiber phase we have obtained information about the length of segments and about their orientation. We do not, however, have any information about the width of segments. To obtain this, we partition the binary image into 1 pixel wide columns perpendicular to the mean fiber orientation, figure 5.6(5). We can now assign a thickness to all points in the original image. The thickness at a point is the number of pixels in the corresponding component found in the columns in figure 5.6(5). We construct a matrix with the same dimensions as the original image where each element is the thickness measured from the slices, figure 5.6(6). This provides a look up table of thicknesses that can be coupled with the

segments from figure 5.6(4).

In summary, to analyse the segments (numbers correspond to the panels in figure 5.6):

1. Following on from step 2 of the void phase analysis, figure 5.5(2), invert the binary image (white become black, and black becomes white).
2. Reduce this binary image to a skeleton by successive erosions until convergence.
3. Identify the branching points of the skeleton using standard algorithms.
4. Remove the branching points from the skeleton and identify the resultant components.
5. Slice the image into columns 1 pixel wide and measure the width of each component in each slice.
6. From 5, construct an array of values of the width of the fiber at that point. (In figure 5.6(6) the intensity is proportional to the width.)
7. Combine 4 and 6, segments are identified from the skeleton and width information is retained by coupling with 6.

Breakdown at late times: In figure 5.6(7) we have illustrated the fiber phase analysis on a sample of $\phi = 0.65$, $B = 1.25$ mT, at a time $t = 3.2$ s after applying a magnetic field. At these early times the segments measured define the perimeters of all voids. In figure 5.7, we show the results for the same sample but at a later time $t = 879$ s. The segments measured define the perimeters of small voids annealed into the fiber phase and, as a result, are often broken into several smaller sections around larger voids. The segments represent the structure of the network at all times but we only expect them to be consistent with the segments defined in random fiber theory at early times.

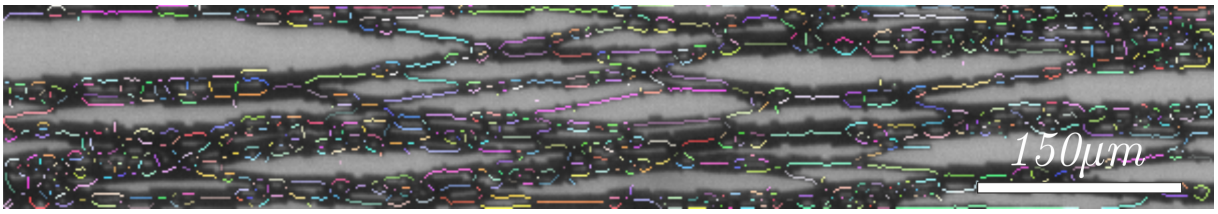

Figure 5.7: The results of the void phase image analysis algorithm, as detailed in the text, at 879 s after the field is applied.

5.4 Results and discussion

At the outset of this chapter, we outlined the theory of random fibrous networks as an idealised model of the network structures that we observe in two dimensional suspensions of paramagnetic particles. First we will establish the distributions of the characterising properties of the void phase: area, a; semi-major radius, r_1; semi-minor radius, r_2; orientation, θ_v; and elongation, r_1/r_2 as well as the characterising properties of the segment phase: length, g; width, ω; and orientation, θ_s. These distributions are compared to the theoretical predictions. Having characterised the distributions, we have established the minimal amount of information required to report a given property, typically using a mean or standard deviation. We go on to establish the interrelations of properties and compare these to the relevant theoretical predictions. Ultimately these interrelations allow us to report a single property which expresses the state of a system in its totality.

The coarsening dynamics are then investigated by considering the influence of time, field and concentration on the evolution of the network structure. It turns out that we observe two distinct growth pathways, one that occurs at higher concentrations and the other at lower concentrations.

5.4.1 Distributions

From the theory of stochastic networks, section 5.2.1, we derived the area of voids and their typical radius from the segment length distribution - we present the segment length distribution first, followed by the distributions of void area and radii. We then present the fiber width distribution, followed by the angular distributions of voids and segments. Note that for all of the void properties we have used an area weighted mean. We use a weighted mean to account for the presence of small annealed voids in the fiber phase that are numerous but do not contribute to the perceived bulk structure. By giving favour to larger voids we capture the dominant features of the network at all times. Additionally, note that all distribution are averaged over all times for all takes $\phi > 0.6$.

Segment length distribution

In figure 5.8*a* we plot the mean segment length, $\bar{g}$, against the standard deviation, $\sigma(g)$. We find that the mean and standard deviation are proportional. Fitting with a straight line $y = a*x+b$, we find that the coefficient of variation is 1.29. The segment length distribution is expected to be an exponential distribution, equation 5.5. The exponential has a coefficient of variation of unity so a value of 1.29 represents a slight deviation of experiment from random fiber theory.

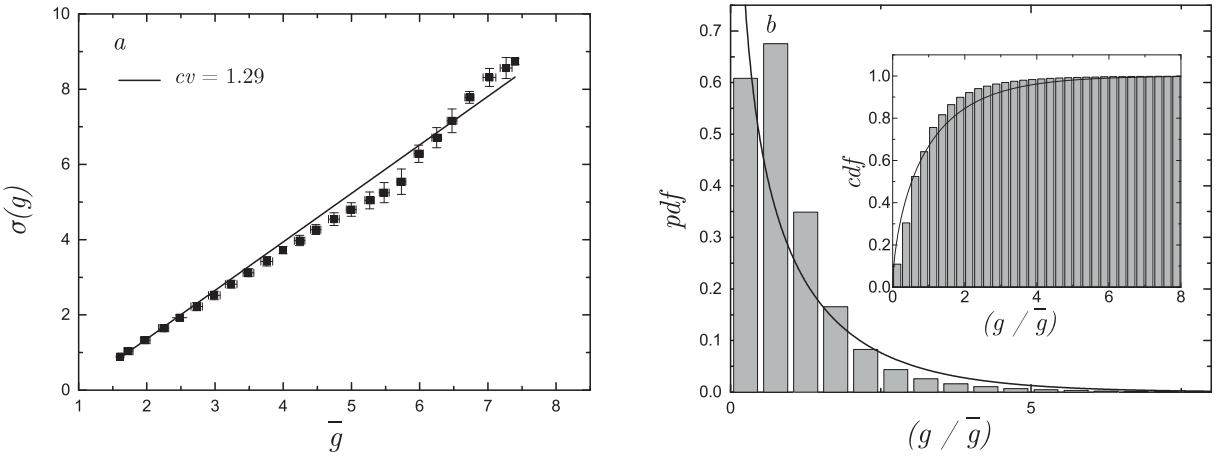

Figure 5.8: (a) The standard deviation of the segment lengths plotted against the mean showing a straight line of gradient 1.29. (b) The pdf of rescaled segment lengths. In black is a gamma distribution, equation 5.6 , with a mean of 1 and the coefficient of variation as measured from experiment, $cv = 1.29$. The inset shows the cdf (cumulative distribution function).

We confirm that the segment length distribution is well described by a Gamma distribution by re-scaling all the segment lengths with the mean and plotting it against a gamma distribution with a mean of 1 and a coefficient of variation of 1.29, figure 5.8*b*.

In section 5.2.1 we noted the possibility of segment length distribution with non unity coefficients of variation. Using the experimentally measured coefficient of variation we predict the influence of this deviation from an exponential distribution on the subsequent void area and radius distributions from equations 5.7 and 5.8. For the area distribution, we now expect a coefficient of variation of 1.28 rather than the 1.18 that we previously observed, table 5.1. Similarly, for the radius we expect the coefficient of variation to be 0.6 instead of 0.53, table 5.1.

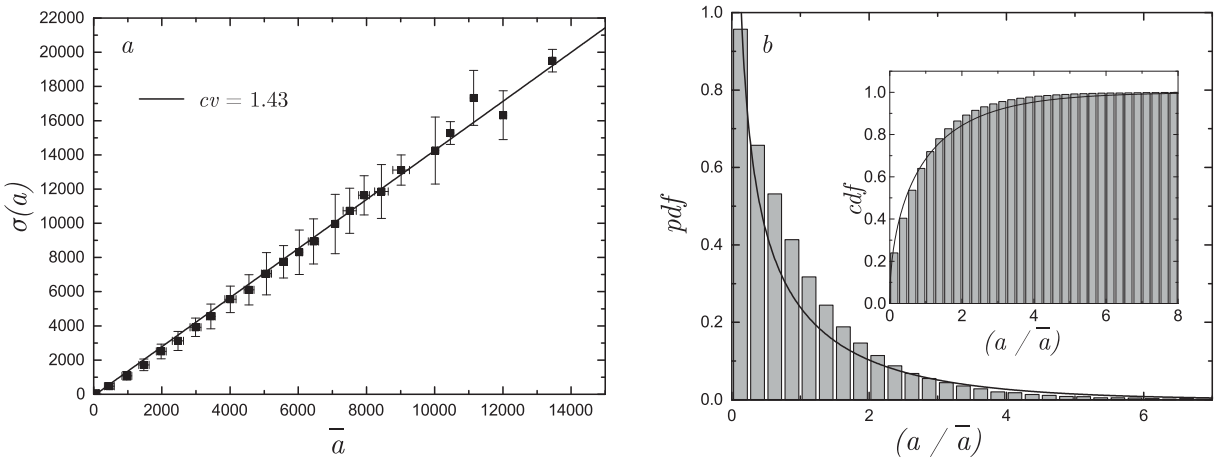

Figure 5.9: (a) The standard deviation of the void areas plotted against the mean showing a straight line of gradient 1.43. (b) The pdf of rescaled void areas. In black is a gamma distribution with a coefficient of variation $cv = 1.43$, as measured from a. The inset shows the cdf.

Void area distribution

In figure 5.9 we plot the mean void area, $\bar{a}$, against the standard deviation, $\sigma(a)$, and find a linear relationship with gradient 1.43. We show in figure 5.9 that this distribution, like the segment length distribution, may be rescaled by the mean and is well approximated by a gamma distribution. Taking into account the cv measured for the segment length distribution, the void area distribution is well captured by random fiber theory. The difference between 1.28, the expected coefficient of variation, and 1.43, the experimentally observed value, may be in part due to the limited range of segment lengths probed. Due to the breakdown in image analysis of the segment length distribution, section 5.3.2, only the early stages of the segment growth are probed.

Void radii distributions

The theory as outlined predicts only a single length scale, equation 5.8, that characterises a void. In the experimental system we find that voids are elliptical and so we can measure the semi-major axis, r_1, and the semi-minor axis, r_2. Both length scales independently follow the predicted distribution, the Gamma distribution, and have coefficients of variation equal to 0.85 and 0.81 respectively, figures 5.10 and 5.11. Like the area distribution, the coefficient of variation is slightly larger than expected from random fiber theory as outlined in section 5.2.1, table 5.1.

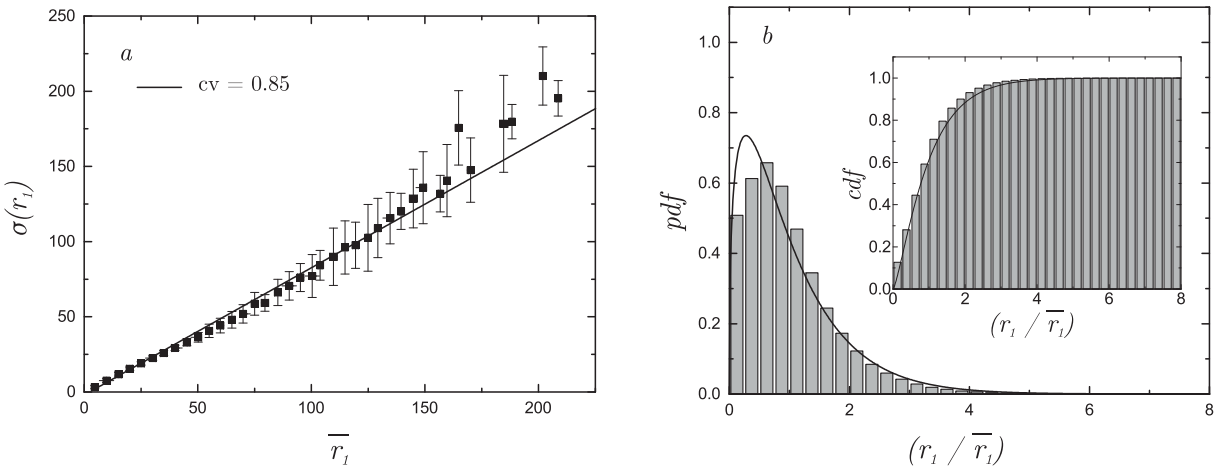

Figure 5.10: (a) The standard deviation of the void semi major axes is plotted against the mean showing a straight line of gradient 0.85 (black). (b) The pdf of rescaled void semi major axes. In black, the gamma distribution with mean 1 and coefficient of variation 0.85, extracted from a. The inset shows the cdf.

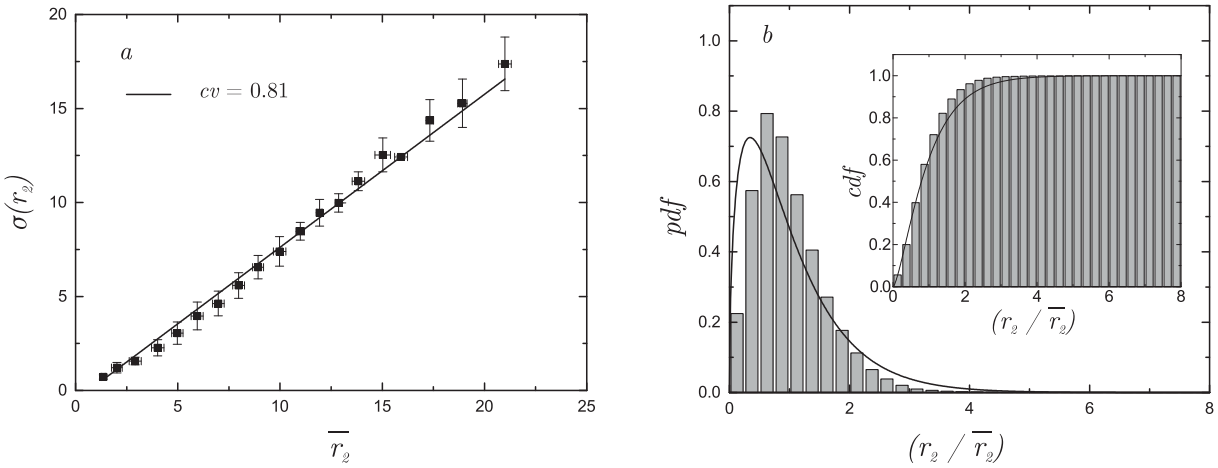

Figure 5.11: (a) The standard deviation of the void semi minor axes is plotted against the mean showing a straight line of gradient 0.81 (black). (b) The pdf of rescaled void semi minor axes. In black, the gamma distribution with mean 1 and coefficient of variation 0.81, extracted from a. The inset shows the cdf.

Segment width distribution

Theoretically, we provide no prediction of how the widths of fibers should be distributed; we assume fiber widths to be constant in the construction of the random fiber model. Experimentally, the case of fiber widths is complicated by the fact that a plot of the mean against the standard deviation is not a straight line, shown in figure 5.12a. At the start of an experiment the particles are randomly arranged in the plane. When a magnetic field is applied they begin to align, initially into chains. As this happens the apparent width, as measured with the image analysis

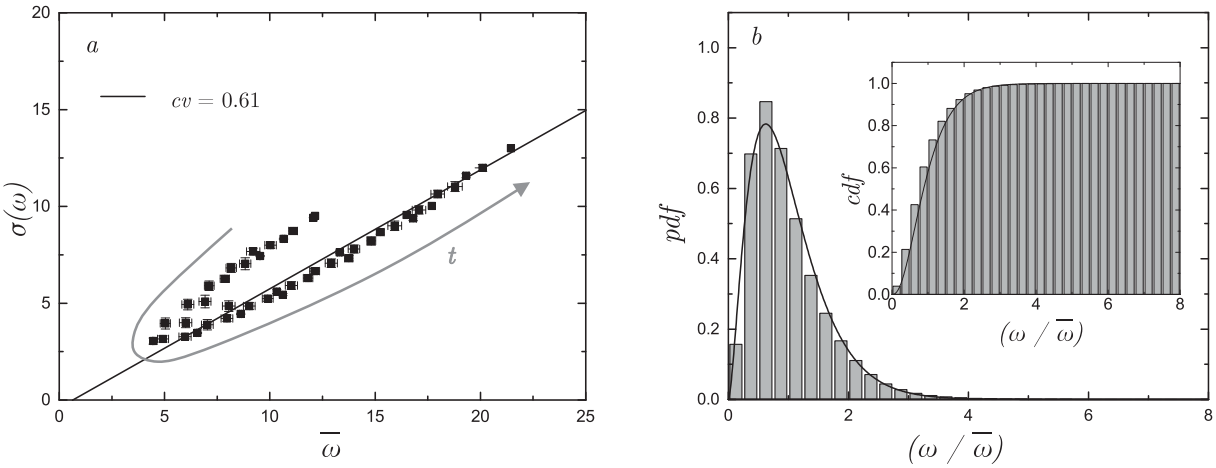

Figure 5.12: (a) The standard deviation of the segment widths is plotted against the mean showing a straight line of gradient 0.61 (black). A grey line indicates the progression of time. (b) The pdf of rescaled segment widths. In black, a gamma distribution with coefficient of variation 0.61 and mean 1 as measured from experiment. The inset shows the cdf.

outlined in section 5.3.2, decreases. As time progresses, particles begin to aggregate laterally and the mean width begins to grow. After this initial attrition of the mean, a linear relationship of mean width and the standard deviation is observed; a gamma distribution manifests when fibers begin to coarsen laterally. The coefficient of variation of this gamma distribution is found to be 0.61.

To complete the treatment of segment widths, the experimental probability distribution is show in figure 5.12*b*, exhibiting excellent agreement with a gamma distribution with coefficient of variation 0.61. The early time behaviour represents a small enough fraction of the total data and do not impact the pdf shown in figure 5.12*b*.

Void and segment orientation distribution

Voids and segments have an orientation that we expect to be centered around the x-axis, the axis along with we apply a field. We compare the distributions to the Von Mises distribution, equation 5.12. In figure 5.13 we show, for a particular experimental run, the histogram of void orientation fitted with a Von mises distribution. Excellent agreement is seen at all times. The Von Mises captures the lack of a preferential orientation at early times and the strong preference at late times.

To consider all the data for different times and takes we must attempt to collapse the

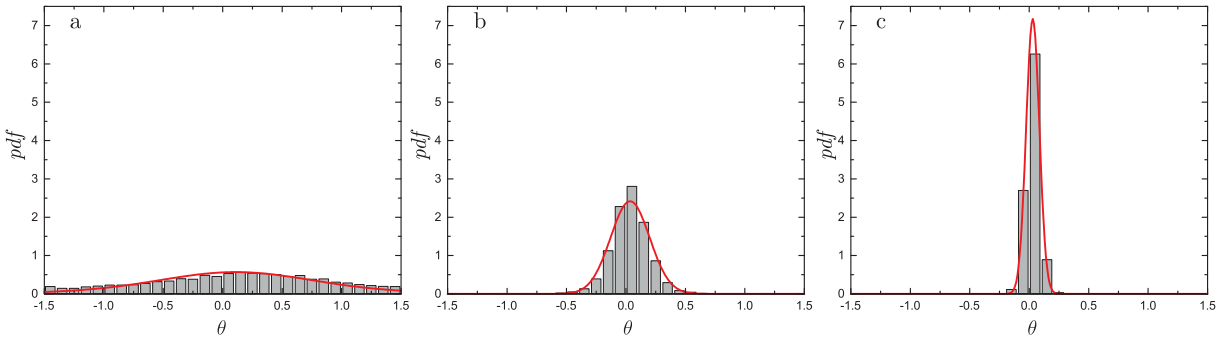

Figure 5.13: The pdfs of void orientations, with a line showing a fitted Von Mises distribution, for three points in time throughout an experiment with $\phi = 0.7$ and $B = 1.87$ mT (a) $t = 0.06$ s, (b) $t = 0.34$ s, (c) and $t = 30$ s after the initial application of the magnetic field.

histograms onto the same distribution. To collapse a data set, $\{P(\theta_{\text{exp}})\}$, onto a Von Mises distribution with $\bar{\theta} = 0$ and $\epsilon_{\text{vm}} = 1$ we estimate the epsilon that best fits a set of data, ϵ_{est}. Then we modify our data with the function:

$$f(P(\theta_{\text{exp}})) = \frac{(2\pi)^{\frac{1}{\epsilon_{\text{est}}}-1}(P(\theta_{\text{exp}})I_0(\epsilon_{\text{est}}))^{1/\epsilon_{\text{est}}}}{I_0(1)}, \tag{5.13}$$

which reshapes the observed curve so that it fits a Von Mises distribution with mean 0 and $\epsilon_{\text{vm}} = 1$. This assumes that the data is indeed Von Mises distributed.

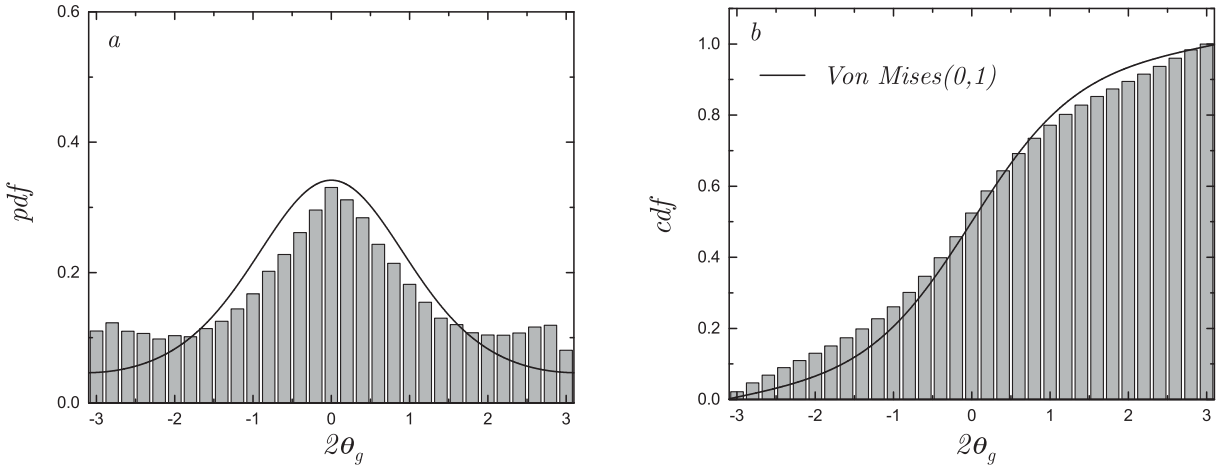

Figure 5.14: (a) The pdf of segment orientations with a line showing a Von Mises distribution with mean 0 and $\epsilon = 1$, (b) is the corresponding cdf.

For the segments, we have removed those that are less than 5 pixels long. Segments shorter than this are limited in the number of orientations accessible due to the small number pixels. If included, these short segments cause a sharp peak at $\theta_s = 0$. We note that there are more high angle segments than expected from a Von Mises distribution, see figure 5.14. This is likely

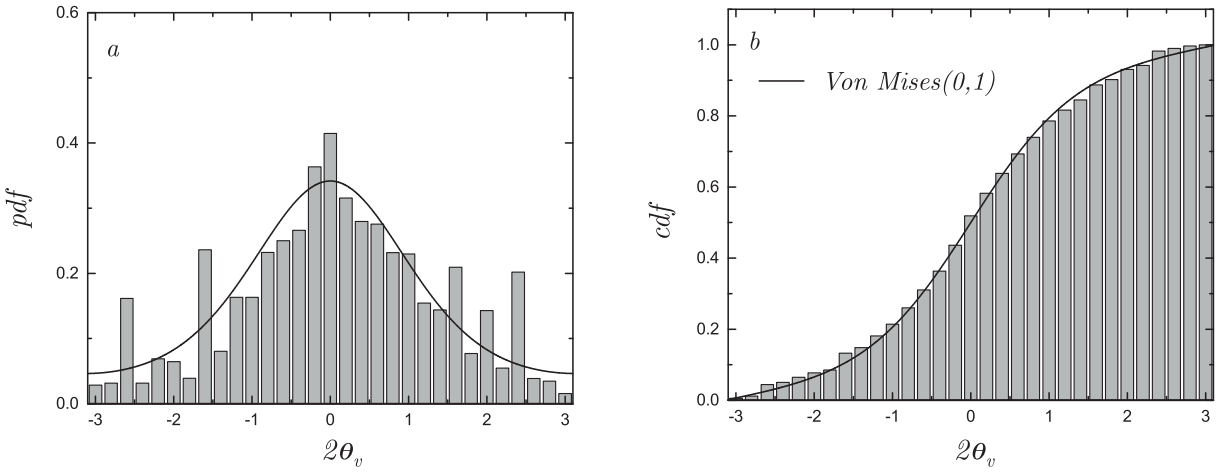

Figure 5.15: (a) The pdf of void orientations with a line showing a Von Mises distribution with mean 0 and $\epsilon = 1$, (b) is the corresponding cdf.

caused by the breakdown of the fiber phase analysis. In the image analysis process, the skeleton has to route around small annealed voids breaking it into small parts at high angles. It is an artifact of the image analysis process as seen in figure 5.7 in section 5.3.2 and is particularly a problem at late times.

The voids, on the other hand, are well described by the Von Mises distribution at all angles, see figure 5.15. For both properties the relevant parameter to report is the standard deviation, $\sigma(\theta)$, as this characterises the spread of the distribution.

Summary of distributions

In characterising the distributions of the length scales in the system we have found that, consistent with theory, the ratio of the standard deviation and the mean is constant. We have made repeated use of the gamma distribution to model these and seen that to a good approximation it represents the observed distributions. Crucially, for all of these properties only their mean determines the full distribution as the coefficients of variation are known. Similarly, treating the orientation distribution of voids and segments as a Von Mises distribution, we can report the angular distributions in terms of the standard deviation only. We have summarised the observed distributions in table 5.2.

Property	Distribution	Coefficient of variation
Segment Length, g	Gamma	1.29
Segment Width, ω	Gamma	0.61
Segment Orientation, θ_s	Von Mises	N/a
Void Area, a	Gamma	1.43
Void Semi Major, r_1	Gamma	0.85
Void Semi Major, r_2	Gamma	0.81
Void Orientation, θ_v	Von Mises	N/a

Table 5.2: The observed distributions and, where relevant, coefficients of variation for all of the properties discussed in the text.

5.4.2 Spatial distribution of voids

The polygons that result from a random line process are distributed randomly over the plane with uniform probability and independently of each other [158]. This is a classic Poisson process - if the plane is segmented into regions of equal area we expect the number of void centers in a region to be described by a Poisson distribution. For a Poisson distributed variable, the mean and variance should be equal, equation 5.4 [140].

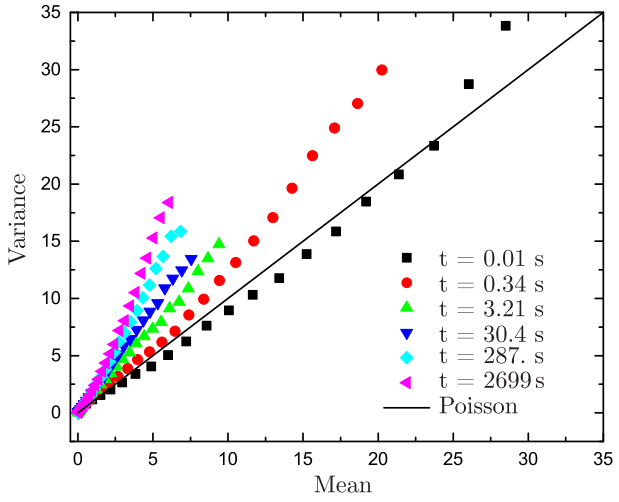

Figure 5.16: The mean number of voids in an area vs the variance of the number of voids in an area for different times throughout an experimental run with surface coverage $\phi = 0.65$ and field strength $B = 1.25$ mT.

To test if the voids are randomly distributed, we segment the plane into squares and calculate the mean number of voids in a square and the variance of the number of voids. We systematically vary the size of the squares used and observe how the mean and variance change. This process is repeated at different times throughout an experimental run revealing how the

distribution evolves in time. The results of this process are shown in figure 5.16. As time progresses the gradient of the mean vs variance line increases indicating a deviation from Poisson behaviour. At later times, when the network is established, stronger deviations from the Poisson process are observed. The positions of voids, therefore, are not independent of each other.

5.4.3 Interrelations of network properties

We relate the key network properties to each other using a combination of random fiber theory and empirically derived relationships. It turns out that by establishing a series of connections between properties we can summarise the complete state of a network with any one property. We will first establish the empirical relations.

Semi major Vs. semi minor: Empirically, the mean length of the semi major axis, $\bar{r}_1$, and the semi minor, $\bar{r}_2$, are strongly correlated. To a good approximation they are linearly related, $\bar{r}_2 = 0.42 + 0.07\bar{r}_1$, see figure 5.17*a*.

Ratio of axis Vs. elongation: Empirically, the mean elongation, the average of r_2/r_1 for each void, is linked to the ratio of the mean of the radii taken independently, $\bar{r}_2/\bar{r}_1$, figure 5.17*b*. This is fitted with a power law and we find that $\langle r_2/r_1\rangle = -0.12 + 0.93(\bar{r}_2/\bar{r}_1)^{0.53}$. An intuitive result would be a one to one relationship. Over the range of values accessible the line of best fit is $\langle r_2/r_1\rangle = 0.07 + 0.99\bar{r}_2/\bar{r}_1$, i.e. an almost one to one relationship, however there is a clear non-linearity in the data.

Elongation Vs. void orientation: Elongated voids experience a torque which tends to align them with the magnetic field. More elongated voids are aligned more strongly by the field. As a consequence, we expect there to be link between the mean elongation and the standard deviation of void angles, plotted in figure 5.17*c*. Empirically, for more elongated structures, smaller values of $\langle r_2/r_1\rangle$, the relationship appears to be linear. The full curve is fitted with $\sigma(\theta_v) = 0.005 + 1.02\langle r_2/r_1\rangle + 37.4\langle r_2/r_1\rangle^{6.4}$.

Void orientation Vs. Segment orientation: The angular distribution of voids and segments are clearly conceptually linked, with segments defining the borders of voids. Plotting the standard deviations of these distributions against each other we find a linear interrelation of $\sigma(\theta_s) = 0.33 + 0.32\sigma(\theta_v)$, see figure 5.17*d*. However, this is only valid for standard deviations

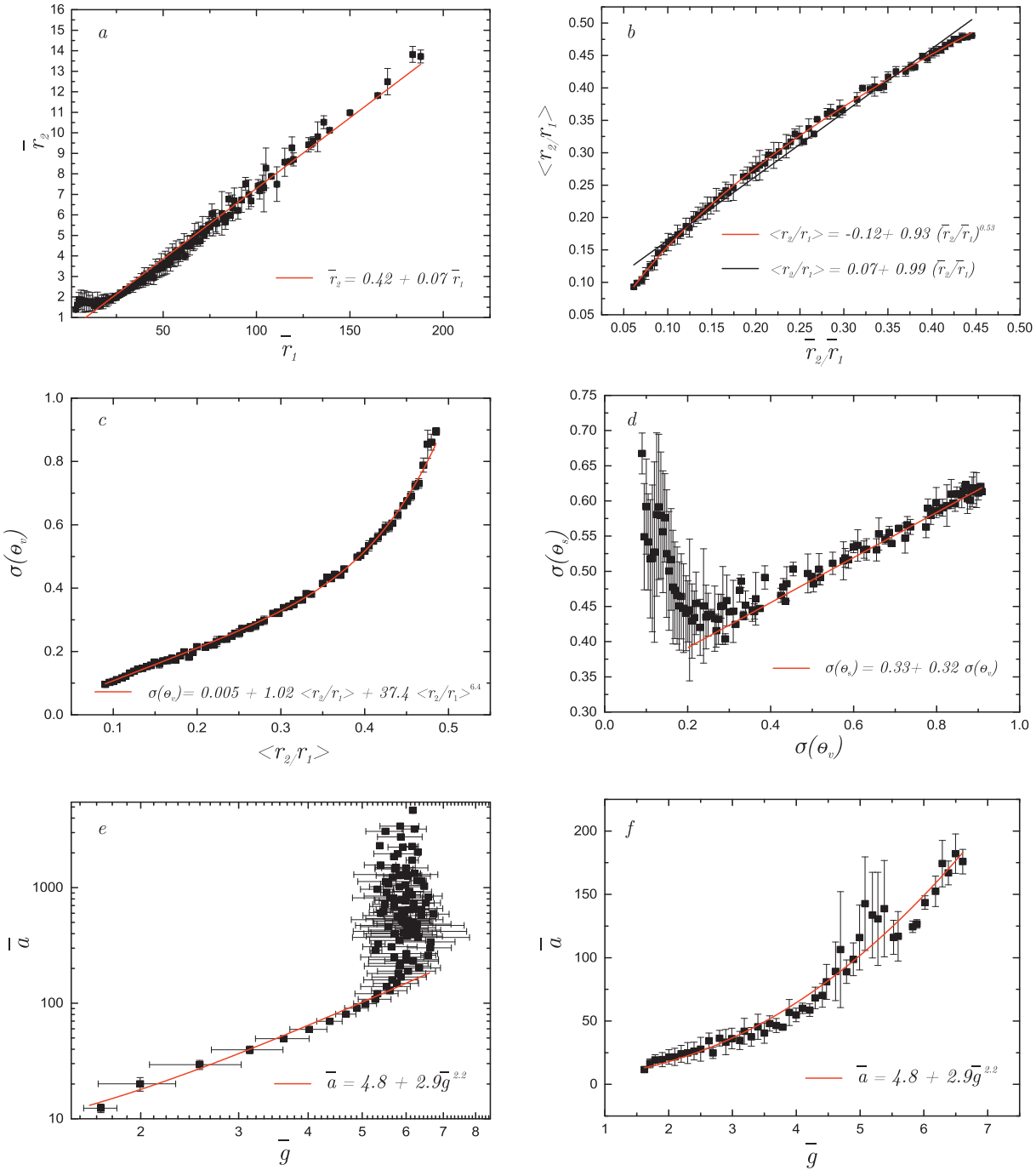

Figure 5.17: (a) Mean length of the semi major axes against the mean semi minor axes. (b) The ratio $\bar{r}_2/\bar{r}_1$ against the mean elongation. (c) Mean elongation against the standard deviation of void orientation. (d) Standard deviation of void orientation against standard deviation of segment orientation. (e) Mean segment length against mean void area for the full range of data. (f) Mean segment length against mean void area for values below the apparent divergence in e. Lengths are in µm and areas in µm^2.

$\sigma(\theta_s) > 0.2$ as our measure of segment angles breaks down at late times due to the presence of small annealed voids in the fiber phase (section 5.3.2).

Segment length Vs. void area and semi major: This breakdown in segment analysis, the partitioning of segments in the image analysis process due to the presence of small annealed voids, is also observed for the interrelations of the mean segment length, $\bar{g}$, with the semi major axis, $\bar{r}_1$, and with the mean void area, $\bar{a}$. For example, both the mean void area and the mean semi-major length diverge at a mean segment length $\bar{g} \approx 6$, figure 5.17*e* and figure 5.18*b*. Considering only values below the apparent breakdown, 5.17*f* and 5.18*a*, we find that $\bar{a} = 4.8 + 2.9\bar{g}^{2.2}$ and $\bar{r}_1 = -6.06 + 5.4\bar{g}$. This is consistent with random fiber theory, from which we would expect $\bar{a} \sim \bar{g}^2$ and $\bar{r} \sim \bar{g}$, table 5.1.

Void area Vs. semi minor: Random fiber theory predicts the mean of void radii to be proportional to the square root of the area. This is confirmed in figure 5.18*c* where we find that the semi-minor axis is strongly correlated with the area with a best fitting power law of $\bar{r}_2 = 0.9 + 0.09\bar{a}^{0.53}$.

Void area Vs. semi major: The semi-major axis is expected to be related to the mean void area in a similar way to how the semi minor axis is related to the mean void area. However, since we already know the interrelation of $\bar{r}_2$ and $\bar{a}$ and the interrelation between $\bar{r}_2$ and $\bar{r}_1$, we can straightforwardly derive a new relation for $\bar{a}$ as a function of $\bar{r}_1$. In figure 5.18*d* we find that the derived relation is in very good agreement with the data.

Segment length Vs. semi minor: For some connections, such as the $\bar{r}_2$ against $\bar{g}$, derived relations are a powerful tool. In the case of $\bar{r}_2$ vs $\bar{g}$, since the void width is typically small when the breakdown of the segment analysis occurs, we have only a limited range of data to establish a relation. Instead, using the relation of $\bar{r}_1$ and $\bar{g}$, and the connection between $\bar{r}_1$ and $\bar{r}_2$, we may estimate $\bar{r}_2$ vs $\bar{g}$ from well established links. Figure 5.18*e* compares the predicted relation[1] and the experimental data. As the aggregation process proceeds agreement between prediction and experiment improves.

Segment length Vs. segment orientation: Linking the mean segment lengths to the standard deviation of segment orientations is not possible as our measure of both properties breaks down

[1]The derived relations often do not have simple functional forms as they result from nested functions, as such they are not presented. All of the information needed to reconstruct them is in the equations given for the other properties.

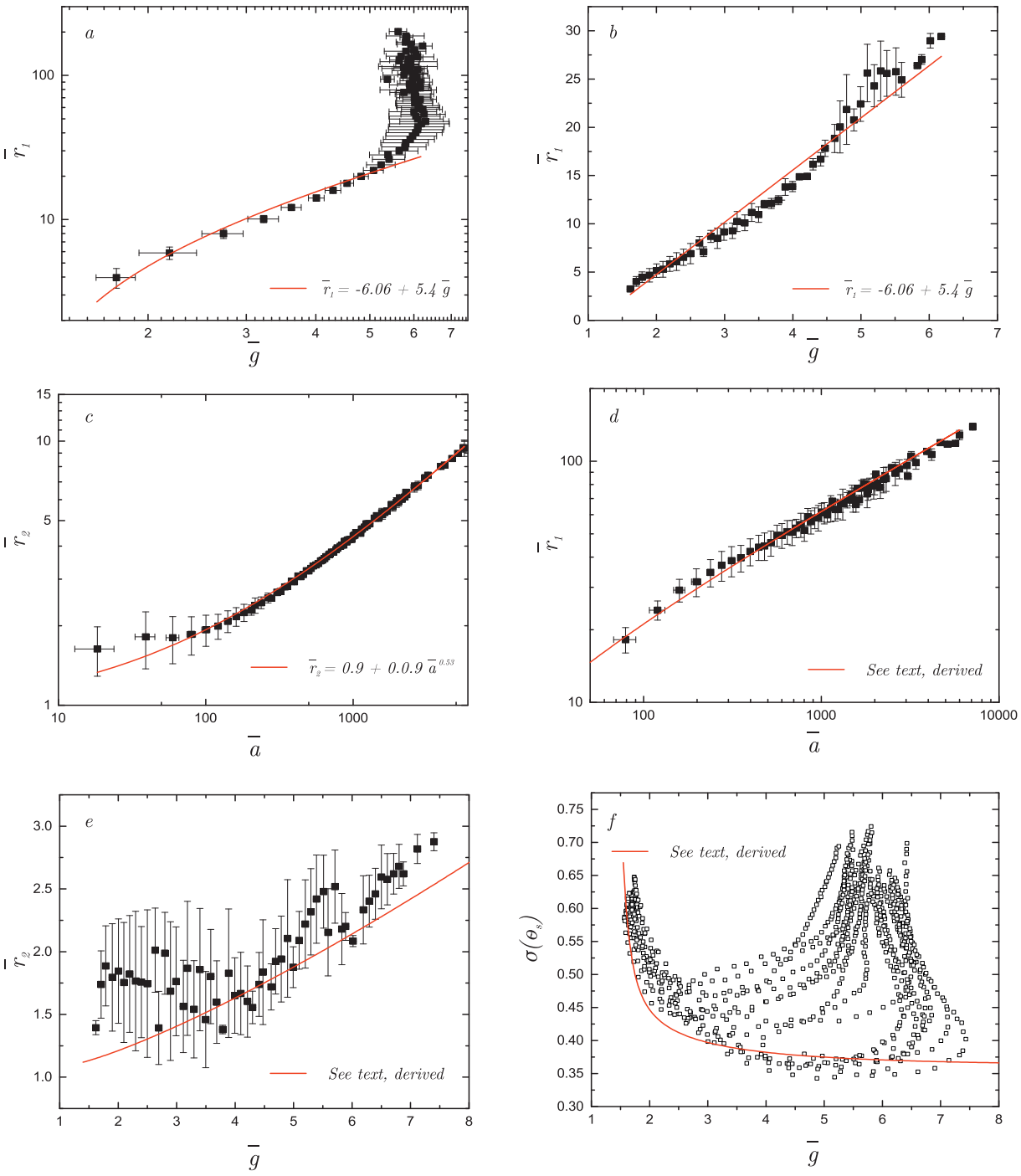

Figure 5.18: (a) Mean segment length against mean semi major length for the full range of data. (b) Mean segment length against mean semi major length for values below the apparent divergence in (a). (c) Mean void area against the mean semi minor length. (d) Mean void area against the mean semi major length. The solid line represents a function derived from the other relationships, see text. (e) Mean segment length against mean semi minor length only for values below an apparent divergence. The solid line represents a function derived from the other relationships, see text. (f) Mean segment length against the standard deviation of segment orientation. The solid line represents a function derived from the other relationships, see text. Lengths are in μm and areas in μm^2.

independently. Using the more strongly defined links already presented we can derive a relation that we would expect to hold if a breakdown did not occur, figure 5.18f. At small segment lengths, early times, the agreement is good. At all times the derived curve appears to describe the minimum observed experimental value and follows the trend we expect from theory i.e. that more strongly oriented fibers give rise to longer mean segment lengths.

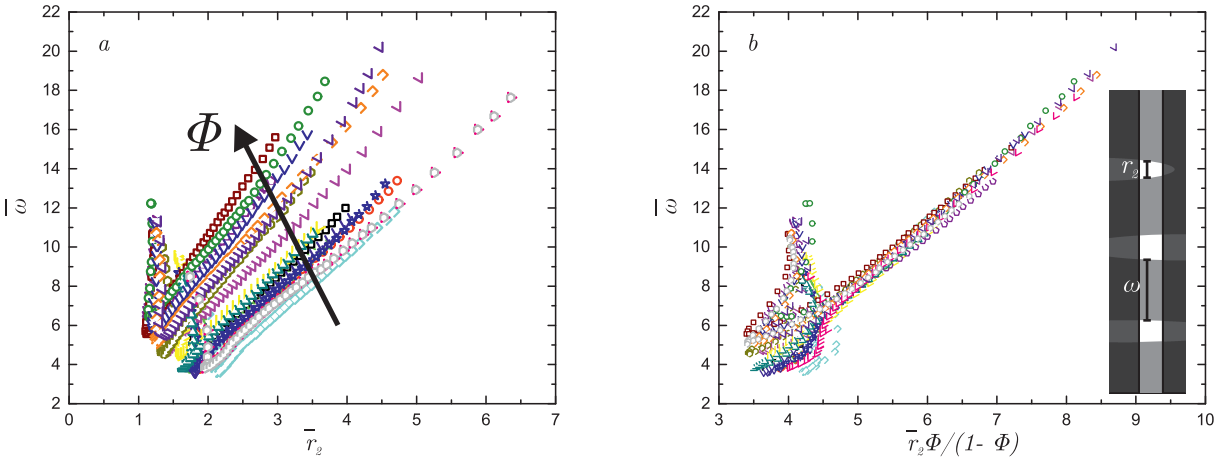

Figure 5.19: (a) Mean void widths, $\bar{r}_2$, against the mean fiber width, $\bar{\omega}$. (b) $\bar{r}_2\phi/(1-\phi)$, a function of the mean void width and the concentration, against the mean segment width. Inset (b) Schematic indicating the conceptual slice outlined in the text. Note: such that the means represent those of a thin slice, as shown in the schematic, we must length weight means for these properties, as opposed to area weighting.

Semi minor Vs. segment width: The final property that we presented a distribution for in section 5.4.1 is the segment widths, $\bar{\omega}$. We relate this to the void semi minor axis, the other dominant length scale in the same direction, see figure 5.19. We find that the link between these two properties is strongly concentration dependent. The widths of voids and the widths of segments make up the height of the image, as illustrated in the inset of figure 5.19. We can define the surface coverage in terms of the mean void radius in a slice as $1-\phi = n\bar{r}_2/h$, where h is the height of the image and n the number of voids. In a slice the number of voids must be the same as the number of fibers. Since nothing other than voids and fibers make up a slice we know that $n\bar{\omega} + n\bar{r}_2 = h$. Substituting $1-\phi = n\bar{r}_2/h$ into this constraint, eliminating h from the equation, we find that $\bar{\omega} = \bar{r}_2\phi/(1-\phi)$. Figure 5.19*b* shows how effectively this captures the concentrations dependence revealing the linear dependence of the two properties. We fit this with a straight line and find that $\bar{\omega} = -7.3 + 3.0\bar{r}_2\phi/(1-\phi)$.

We have established a graph of properties using the interconnections defined above, figure 5.20. This allows graph us to predict the value of all properties knowing the value of just one.

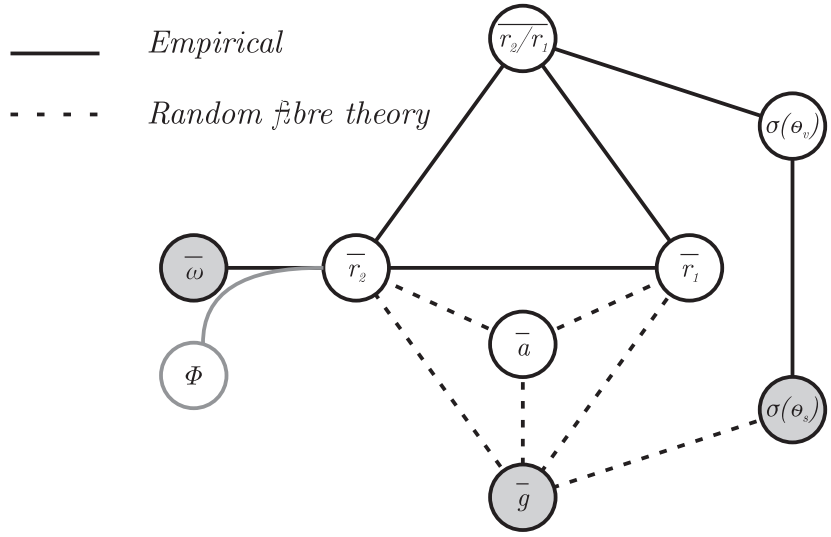

Figure 5.20: All of the interrelations of properties we use to characterise particle networks. solid lines indicate confirmed relations. White circles are void properties, grey circles are fiber properties. See figure 5.17 and figure 5.18 , as well as the text, for details of these relations.

For example, knowledge of the mean void area is sufficient to state the standard deviation of the orientation of voids by calculating the mean void radii, then from this the elongation, and finally linking the elongation to the void orientation. Crucially, it represents a way of reducing the number of properties required to summarise the state of a network as a whole to a single property.

5.4.4 Coarsening dynamics

The statistical geometry of networks, discussed in the previous sections, was presented for samples with surface coverages $\phi > 0.60$. At these concentrations, at all times a network consistent with random fiber theory is observed. Concentrations below this threshold form a system spanning network via a qualitatively different pathway. Transiently, the distributions of structural properties in these lower concentration takes are not consistent with random fiber theory. As they are not fibrous networks at all times these takes were omitted from the previous section.

Plotting the weighted mean void area against time in figure 5.21 and splitting the data into takes above this threshold value, $\phi > 0.60$, and takes below it, $\phi < 0.60$, reveals the difference between the network formation at high concentrations and at low concentrations. When $\phi > 0.60$, we observe power law behaviour at all times, i.e. $\bar{a}$ vs t is a straight line in

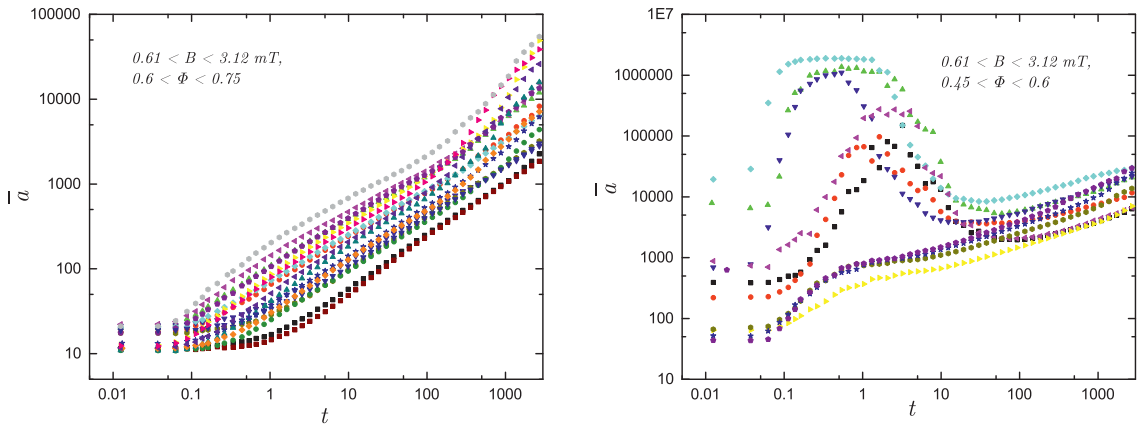

Figure 5.21: (a) Plots of the weighted void area against time for takes with surface coverages $0.6 < \phi < 0.75$, for the full range of fields 0.614 mT $< B <$ 3.12 mT. (b) Plot of the mean weighted void area against time for takes in the range $0.45 < \phi < 0.6$, for the full range of fields. Note the difference in scale between (a) and (b). Areas are given in units of μm^2 and time in seconds.

log-log space. For $\phi < 0.60$, on the other hand, $\bar{a}$ is only power law at late times ($t > 50$ s). At times shorter than this, there is a period of rapid growth of the mean cluster size. This growth profile either shoulders before entering a power law regime or peaks and decreases before entering a power law regime.

The mechanisms of growth are revealed by plotting snapshots of the image analysis at key points throughout an experiment. In figure 5.22 we show snapshots for both a high concentration ($\phi > 0.60$) sample and a low concentration sample ($\phi < 0.60$) alongside plots of the weighted mean area against time for these samples. For the low concentration sample, $\phi = 0.54$, particles begin to align with the field but retain enough of the disorder of their starting configuration such that they segment the plane, figure 5.22a.1. The growth of chains continues and the particle phase, transiently, does not form a percolating network, figure 5.22b.1. Chains and small clusters begin to combine and segment the plane, restoring percolation. Instead of ellipses, voids are maze-like structures with many unconnected ends of chains, figure 5.22c.1. As the free ends connect with each other, and with the sides of other chains, voids become convex and the network begins to resemble a random fiber network, figure 5.22d.1.

We contrast this with the higher concentration sample, $\phi = 0.67$, which forms a percolating network of particles at all times. At early times, the void shapes are still strongly influenced by their random starting configuration, figure 5.22a.2. From then on, ellipse like voids grow and fibers thicken, figure 5.22b.2 $-$ d.2.

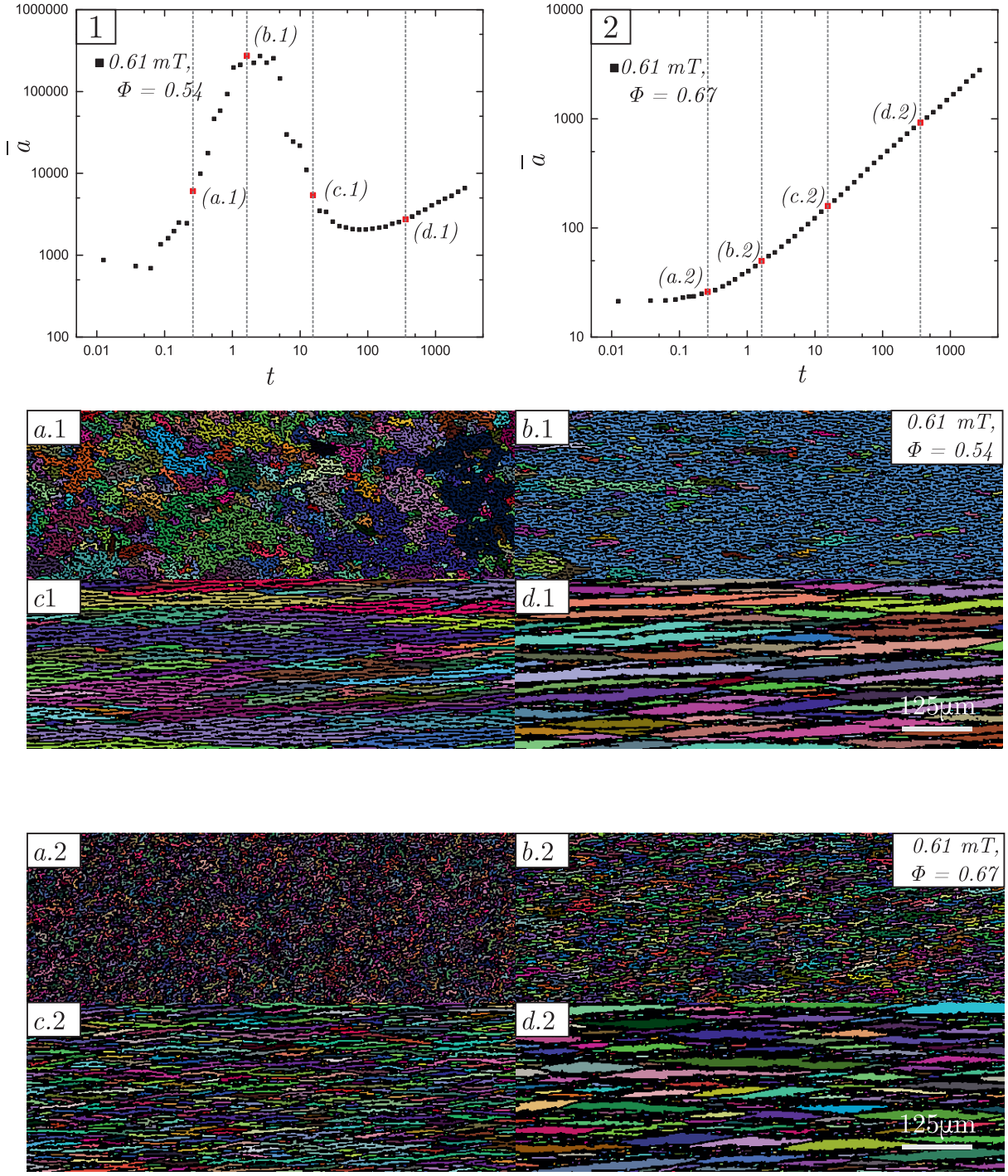

Figure 5.22: (1) A plot of the mean void area against time for a sample with $\phi = 0.54$ subjected to magnetic field $B = 0.614$ mT. (2) Plot of the mean void area against time for $\phi = 0.67$ subjected to a field $B = 0.614$ mT. (a.1 - d.1) Snapshots indicating the components identified by image analysis for the frames indicated on (1). (a.2 - d.2) Snapshots indicating the components identified by image analysis for the frames indicated on (2).

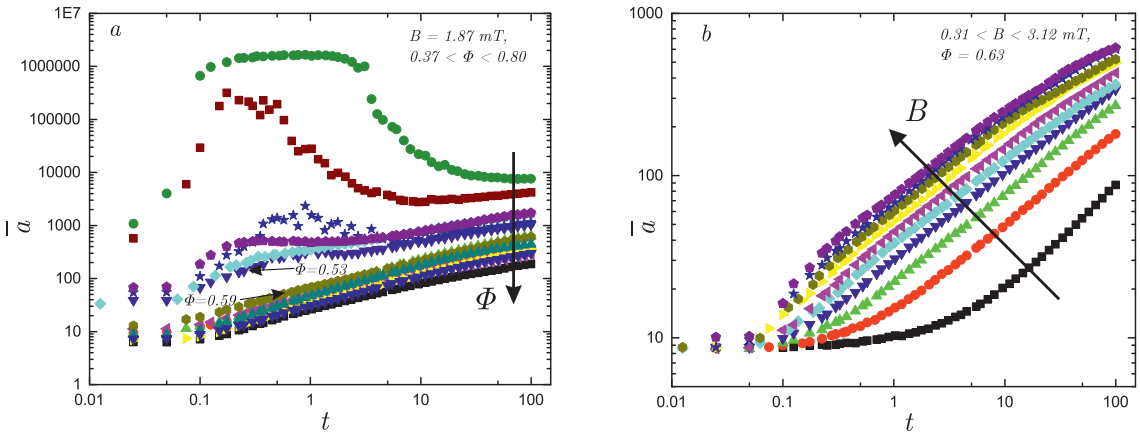

Figure 5.23: (a) Plots of the weighted void area against time for a range of surface coverages, $0.37 < \phi < 0.8$, all at a field $B = 1.87$ mT. (b) Plots of the weighted void area against time for a range of field strengths, 0.31 mT $< B <$ 3.12 mT, for the same sample with a surface coverage of $\phi = 0.63$.

To probe the transition in mechanism, which we expect to be strongly concentration dependent, we perform a series of experiments at the same field strength while systematically varying the concentration in the range $0.37 < \phi < 0.8$. Having confirmed that at long times ($t > 100$ s) the power law behaviour persists, figure 5.21, we focus on the early time dynamics only ($t < 100$ s). When $\phi = 0.59$ we observe power law growth at all times while for $\phi = 0.53$ we observe a deviation from power law, a marker of the onset of the low concentration growth mechanism, figure 5.23.

Also in figure 5.23, we probe the field dependence of the coarsening process. For a single sample, surface coverage $\phi = 0.63$, we perform multiple experiments, systematically applying fields in the range 0.31 mT $< B <$ 3.12 mT for 100 s and allowing the sample to relax for at least 10 minutes before applying a new field. For the complete range of fields we find that the mean void size grows as a power law in time and that stronger fields cause the network to coarsen more rapidly. The mean cluster size at the start of all runs is the same indicating that all sample have been fully randomised.

In chapter 3 we outlined a method for extracting the concentration dependence and the magnetic field dependence of the physical timescale present in the growth of the mean chain length. We assumed that the property of interest is given by a monotonically growing function $f(\phi^\alpha B^\beta t)$. We measured the time at which a particular mean chain length is achieved for different takes and, since the mean chain length is the same, we know that $\phi^\alpha B^\beta t$ must also be

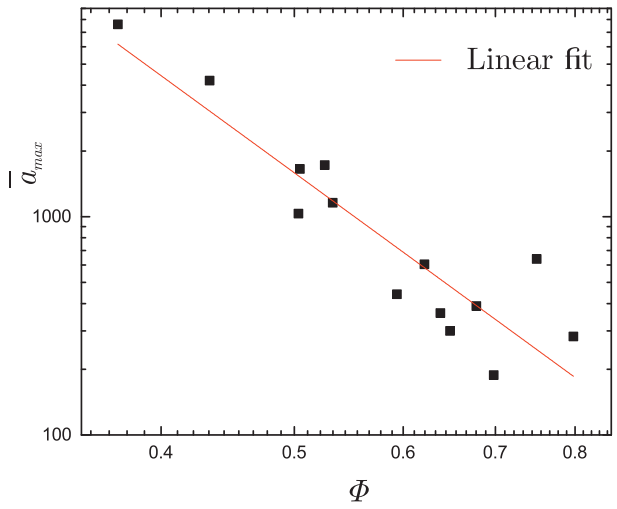

Figure 5.24: (a) Maximum void area, $\bar{a}_{\max}$, plotted as a function of ϕ, the surface coverage, with a straight line fit in red. (b) Plot of the time exponents, c, against surface coverage with the mean value indicated in red.

the same. As a result, a plot of $\log(B)$ vs $\log(t)$ is a straight line with gradient $-\beta$ for takes at the same surface coverage. Conversely, a plot of $\log(\phi)$ vs $\log(t)$ is a straight line with gradient $-\alpha$ for experiments performed with the same magnetic field strength. We use the same method here to extract the field strength dependence of the coarsening of the mean void area.

The experiments at a fixed magnetic field allow us to investigate the concentration dependence of the growth process. Not all takes grow monotonically so the method outlined above cannot be applied. The low concentration pathway ($\phi < 0.6$), in which particles do not form a percolating network at all times, is likely to be a strongly concentration dependent phenomena. To estimate the magnitude of this effect we plot the final area observed, $\bar{a}_{\max}$, as a function of ϕ. We find that $\bar{a}_{\max} \sim \phi^{-4.6}$ revealing this strong concentration dependence.

The magnetic field dependence, however, is well characterised with this method. In figure 5.25a we show a plot of $\log(B)$ vs $\log(t)$ performing the extraction at different mean areas. Independent of the mean void area chosen, we see a straight line with the same gradient. From this we estimate that the β exponent is $\beta = 1.94$. From a naive point view a value of 2 is to be expected as the force acting between particles scales in this way, section 2.2, and as a consequence so too would an inherent timescale. In figure 5.25, as a visual confirmation, we rescale time to collapse the data from experiments at $\phi = 0.63$ by plotting t^* against $\bar{a}$, where $t^* = B^\beta t$. An excellent collapse is seen at all times indicating that this time scale applies throughout the

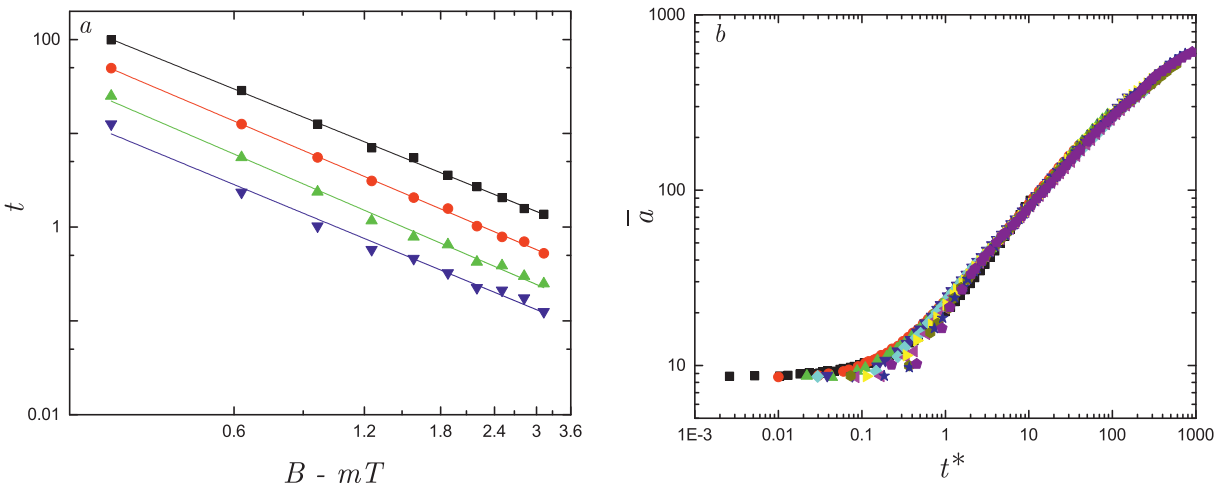

Figure 5.25: (a) Plots of the field strength against the time at which a particular mean void area occurred. Different colours correspond to slices at different void areas. Black - $\bar{a}_{\text{cut}} = 88a^2$, Red - $\bar{a}_{\text{cut}} = 54.6a^2$, Green - $\bar{a}_{\text{cut}} = 34.7a^2$, Blue - $\bar{a}_{\text{cut}} = 23.2a^2$. (b) Mean void area, $\bar{a}$, as a function of a rescaled time $B^{\beta}t$ where $\beta = 1.94$, determined from the slopes of (a).

aggregation process. Fitting with a power law we find that $\bar{a} = 7.05 + 16.4(B^{1.94}t)^{0.56}$.

5.5 Conclusion

We have investigated the structure and dynamics of two dimensional magnetorheological networks. We show that from digital microscopy images quantitative measures of the void areas, radii and orientations can be obtained, as well as measures of the segment lengths, widths and orientations. We interpret these in the light of random fiber theory and find that the probability distributions are in good agreement with theory. Using a combination of random fiber theory and empirically derived relations, we show that all of the network measures are interrelated such that stating any one property is sufficient to derive the others. In the light of this, we investigate the coarsening dynamics of the network in terms of the mean void area and two qualitatively different mechanisms of growth were observed. At long times, we find a power law growth with a time exponent of ≈ 0.5. The physical reason for the empirical relations of network properties is not investigated and a detailed model of the coarsening dynamics remains an open question.

Acknowledgements

This work was carried out in collaboration with William Sampson, and Michael Juniper. We also thank David Robinson and Mark Wilson for many useful discussions.

Chapter 6

Coordination number statistics of network formation

ABSTRACT

In this chapter, we propose a link between random fiber theory and the coordination number statistics of particles that make up a magnetorheological network. We show that the fraction of particles in the network with a coordination number less than 6 is key in quantitatively predicting the area of voids. Also, we show that clusters of 2 and 4 coordinate particles correspond to segments in a random fiber interpretation of the network, while clusters of 6 coordinate particles represent a population of filled voids. Additionally, we show that singly coordinated particles are a sensitive diagnostic tool to probe the initial aggregation mechanism.

6.1 Introduction

To fulfill the goal of exerting some degree of control on the structures of self-assembled materials it is key to understand the interplay of local structure, macroscopic structure and dynamics. One of the key properties that characterises the local structure around an entity is its coordination number [66, 70, 133, 163]. In particular, coordination numbers are used to quantify the local structure in colloidal gels [67, 164–167]. System spanning networks of particles formed due to induced anisotropic interactions have been observed in both electrorheological and mag-

netorheological systems [33, 34] and are another fascinating example of assembly. A detailed investigation of the microscopic properties of these field induced networks in terms of the coordination numbers is lacking. As we show in this chapter, the coordination number analysis of two dimensional networks of paramagnetic provides a quantitative link between the microscopic structure and the mesoscopic structure.

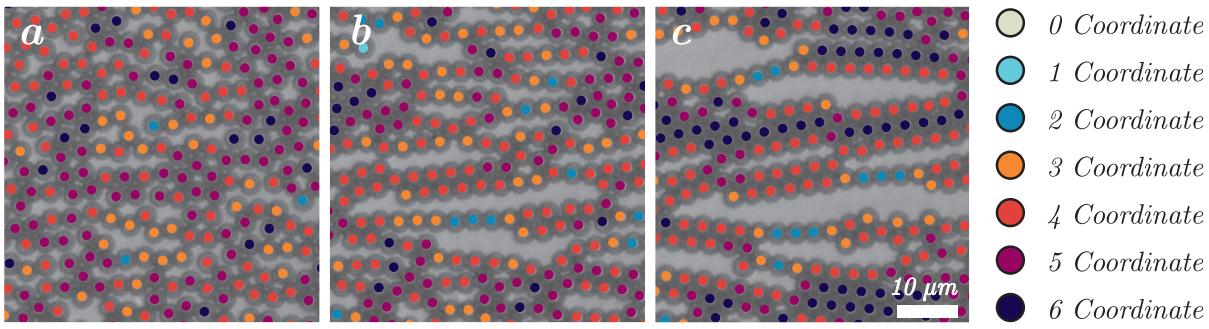

Figure 6.1: Images of the network formation in a sample of paramagnetic particles, surface coverage of $\phi = 0.60$, subject to a uni-axial magnetic field of strength $B = 1.55$ mT. The coordination numbers of particles are shown, and are determined by the image analysis outlined in section 6.3. (a) $t = 0.1$ s after application of the magnetic field. (b) $t = 1$ s. (c) $t = 10$ s.

We investigate the coordination number statistics of networks using the experimental colloidal model system of 3 μm paramagnetic particles introduced in the previous chapters. An example time series is presented in figure 6.1 showing the coordination numbers of a small number of particles during network formation. A clear evolution of coordination number can be seen. We combine the image analysis of particles and networks, and the cluster analysis methods introduced in the preceding chapters. It turns out that the fraction of particles that are not 6 coordinate is a key parameter in quantitatively linking the coordination numbers and the larger scale network properties which were discussed in chapter 5. We also find that the coordination numbers are a sensitive measure of different aggregation mechanisms.

First, we present a theoretical link between the coordination number statistics of particles and random fiber theory, section 6.2. We re-introduce the experimental system and outline the specific alteration we have made for this chapter, section 6.3. We then confirm that the analysis of these experiments is consistent with the previous chapter and go on to discuss the importance of coordination numbers in determining the structure and dynamics of network formation in the results section, section 6.4.

6.2 Theory

Random fiber theory accurately predicts the distributions of pore dimensions and fiber dimensions in two dimensional networks of paramagnetic particles, as shown in chapter 5. The theory presented in chapter 5 is constructed independent of the particles that make up the network. Here we propose a quantitative link between the theory of random fibrous networks and our experimental system in terms of the coordination numbers of the particles.

6.2.1 Random fiber theory and coordination number statistics

In figure 6.2*a* we illustrate a line process with voids randomly filled. Comparing this to figure 6.2*e*, in which we illustrate a network with all of the 6 coordinate particles faded, we see that 6 coordinate particles correspond to the filled voids of a line process. In this analogy all of the particles that are not 6 coordinate particles correspond to the lines in a line process and clusters of 6 coordinate particles are filled voids.

In our experiments we observe that, for a percolating network, only particles with coordination numbers of $c = 2, 3, 4, 5$, and 6 have a significant population. In an idealised scenario these can be split into several categories:

- 2 coordinate particles are primarily in 1 particle wide chains that separate voids, shown in figure 6.2*b*.
- 4 coordinate particles are on the edge of fibers. They will either have 6 coordinate particles on one side and a void on the other or, if the fiber is 2 particles wide, a void on both sides, shown in figure 6.2*c*-*d*.
- 6 coordinate particles form clusters bordered by chains of 4 coordinate particles and by nodes of 3 and 5 coordinate particles, shown in figure 6.2*e*.
- 3 and 5 coordinate particles define nodes - the intersection between chains.

To predict the mean area, we recast equation 5.2 for the number of crossings per unit area,

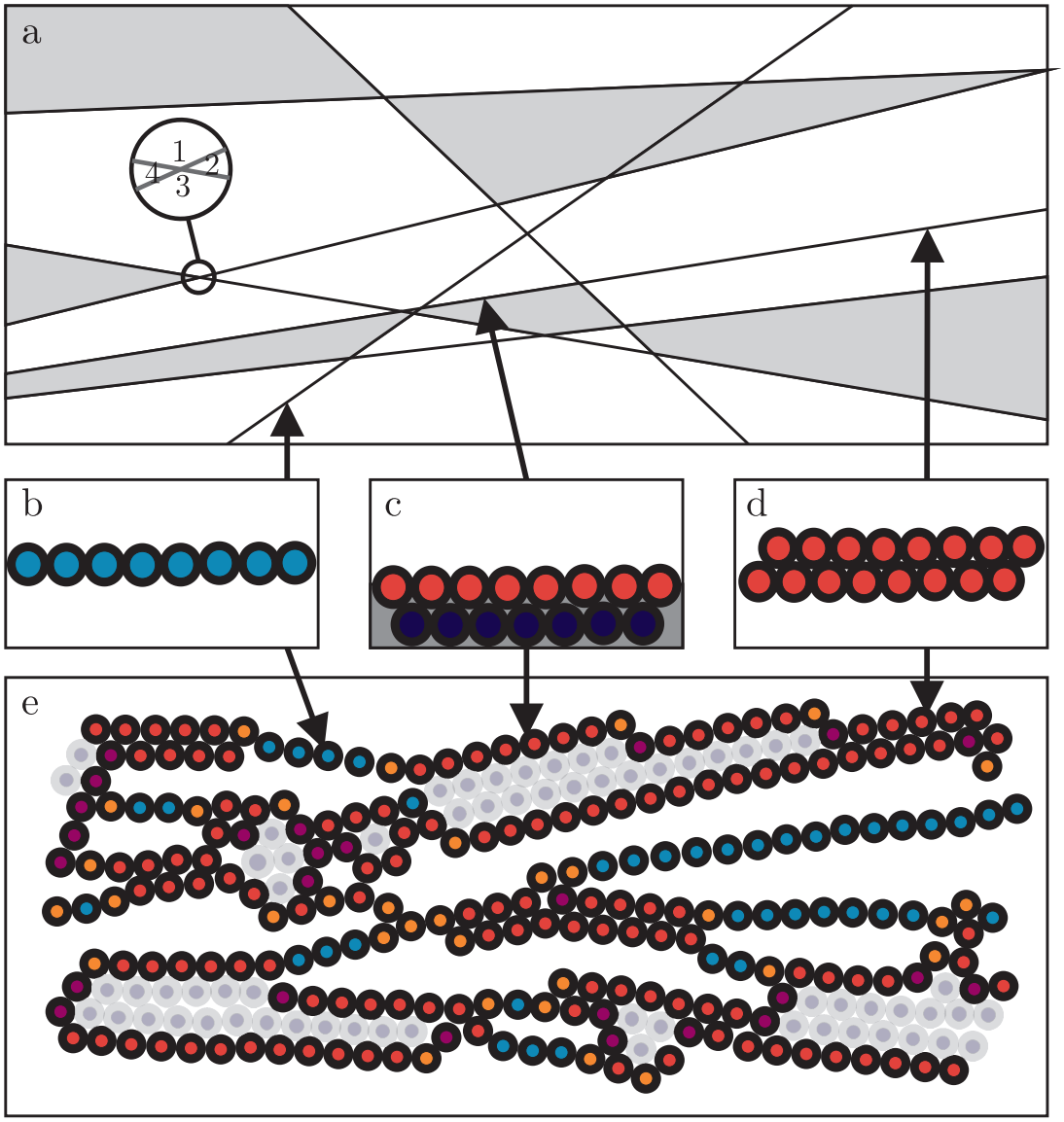

Figure 6.2: (a) A line process defining polygons, which we call voids. A random selection of the voids are greyed out, which we will refer to as filled voids. (b) A chain of 2 coordinate particles with a void above and below. (c) 4 coordinate particles on the edge of a thick fiber. They have a void on one side and 6 coordinate particles on the other. (d) A 2 particle wide chain. In this case all particles are 4 coordinate. (e) An illustrative schematic of a network of particles. Particles with six neighbours are greyed out to highlight the idea that all other particles represent a line process in the plane.

n_{cross}, in terms of τ, the total line length per unit area [162]:

$$n_{\text{cross}} = \frac{\tau^2}{\pi}. \tag{6.1}$$

In figure 6.2*e* we have shown how all non-six coordinate particles contribute to the total line

length. Assuming that all particles contribute a length equal to their diameter, $2a$, to the total line length, then the total line length per unit area will be $2(1 - P(c = 6))an$, where n is the number of particles in a unit area. Noting that, in a unit area, $\phi = n\pi a^2$, we have:

$$\tau = \frac{2\phi}{\pi a}(1 - P(c = 6)). \tag{6.2}$$

In a line process, all intersections contribute 4 verticies to polygonal voids, as shown in figure 6.2*a*. It is known that the mean number of sides of the polygons formed by a line process is also 4 [158, 162]. It follows that $n_{\text{void}} = n_{\text{cross}}$. The mean area, $\bar{a}_{\text{line}}$, is then the area (defined to be a unit area) divided by the number of voids [162]:

$$\bar{a}_{\text{line}} = \frac{1}{n_{\text{void}}} = \frac{\pi}{\tau^2} = \frac{\pi^3 a^2}{4\phi^2(1 - P(c = 6))^2}. \tag{6.3}$$

Equation 6.3 holds true for lines without thickness. The particles that define the line process occupy an area of $\phi(1 - P(c = 6))$. Taking this into account we find the mean area of voids is:

$$\bar{a}_{\text{all}} = \frac{1 - \phi(1 - P(c = 6))}{n_{\text{void}}} = \frac{\pi^3 a^2(1 - \phi(1 - P(c = 6)))}{4\phi^2(1 - P(c = 6))^2}. \tag{6.4}$$

6.3 Methods

We use the colloidal model system of monodisperse paramagnetic spheres with a diameter of 3.0 µm outlined in section 2.3.2. Concentrated suspensions with packing fractions $0.35 < \phi < 0.6$ are confined by gravity to a monolayer at the bottom of a quartz glass sample cell. A uniform external magnetic field with field strengths ranging from $B = 0 - 3.2$ mT is applied throughout the whole sample. The subsequent network formation is captured using video-microscopy, outlined in section 2.4.

Compared to the previous chapter, where we also looked at network formation, we use a 40× objective as opposed to a 4× objective. As a result, single particle detection is now possible as the typical radius of a particle is ~ 10 pixels. However, we can only probe a limited range of network formation due to the limited field of view. To ensure reliable results at all times, we

only probe the first 10 s of network formation.

To measure the coordination numbers of particles in an image, we use the single particle detection outlined in section 2.4.1 and clustering algorithms outlined in section 2.4.3. First, we binarise an image with an intensity threshold. In the resulting binary image both voids and particles are present as white pixels. We then separate the components that correspond to particles and the components that correspond to voids by introducing a size criterion, i.e. we declare all components larger than the typical size of the particles' bright spot as voids. For the particle components we compute their coordinates, and for the voids we count the number of pixels in each component and take this as a measure of their area.

From the particle coordinates we construct an adjacency matrix where neighours are determined by a distance cutoff and from this adjacency matrix we can calculate the coordination numbers of particles using equation 2.25, section 2.4.3. We can then use the clustering algorithm outlined in section 2.4.3 to determine clusters of 6 coordinate particles.

We also use the clustering algorithm outlined in section 2.4.3 to determine chains of particles which are either 2 or 4 coordinate. To ensure that we identify chains of particles we use the criteria that particles must be both within a radius determined by the minimum in the $g(r)$ and within a vertical displacement of $1.5a$ to be considered neighbours. This separates chains that are laterally aggregated and aligned with the applied field (x direction).

6.4 Results and discussion

6.4.1 Void areas

In this chapter we will use the mean void area to characterise the state of a percolating network of paramagnetic particles. In chapter 5, we found that the area weighted mean void area can be used as one of the main statistical parameters that characterise these magnetorheological networks, see section 5.4.3. In chapter 5 we used area weighted statistics due to the presence of small annealed voids. At the relatively short timescales that we probe in this chapter, we do not expect to need to area weight the void distributions as we observe few small annealed voids over these timescales. To confirm that the use of unweighted statistics is applicable here we

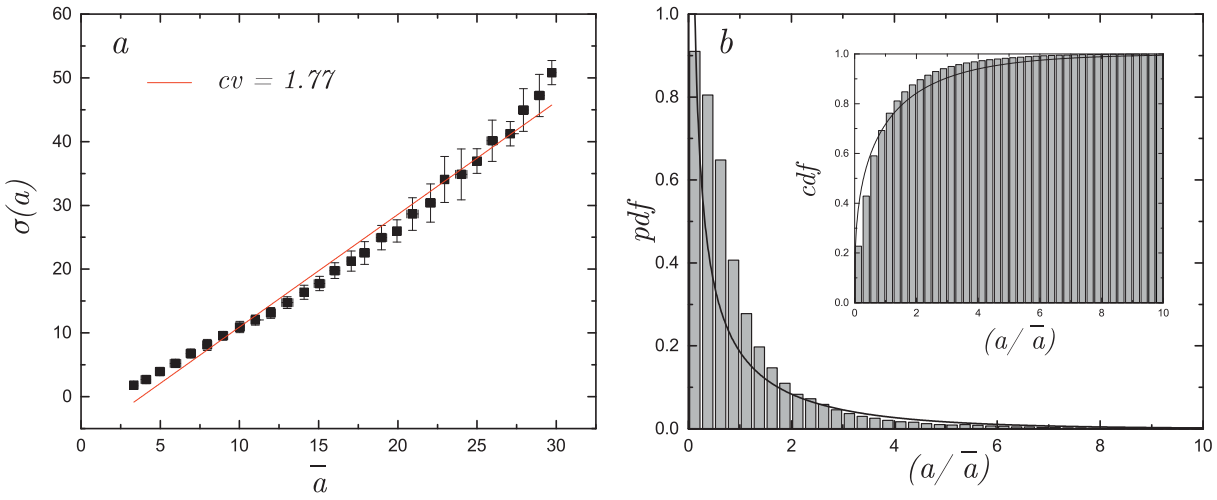

Figure 6.3: (a) The standard deviation of void areas plotted against the mean showing a straight line of gradient 1.77. (b) The pdf of rescaled void areas. In black, a Gamma distribution with a mean of 1 and a coefficient of variation $cv = 1.73$ (equation 5.6). The inset show the cdf.

compare the coefficient of variation, cv, of void areas to the prediction of random fiber theory (see table 5.1 for reference). From figure 6.3*a*, where we plot the mean void area against the standard deviation of the void areas, we find that the coefficient of variation is constant and has a value of 1.7, consistent with the random fiber theory prediction of $cv = 1.73$. From random fiber theory, as outlined in section 5.2.1, we expected the void areas to be Gamma distributed, equation 5.6. To test this we renormalise the experimental void area distributions by the mean void area, plotted in figure 6.3*b*, and find that the resultant distribution is well approximated by a Gamma distribution with the random fiber theory coefficient of variation ($cv = 1.73$). For this analysis we have considered only runs with a concentration greater than $\phi = 0.55$. At these concentrations a percolating network of particles is observed at all times, consistent with the observations made in section 5.4.4 where we found that the crossover between systems that are percolating at all times and those that are not was in the concentration range $0.53 < \phi < 0.59$.

In figure 6.4*a* we plot the void area against time for three samples with concentrations of $\phi = 0.4$, $\phi = 0.5$, and $\phi = 0.6$. In the growth of the mean void area we observe a transition from power law like behaviour, $\phi = 0.6$, to non-monotonic growth, $\phi = 0.4$ and $\phi = 0.5$, as discussed in section 5.4.4. The root cause of this change in growth profile is the transition from a percolating network being present at all times (monotonic pathway) to having an initial period of cluster growth followed by coarsening of a percolating network (non-monotonic pathway).

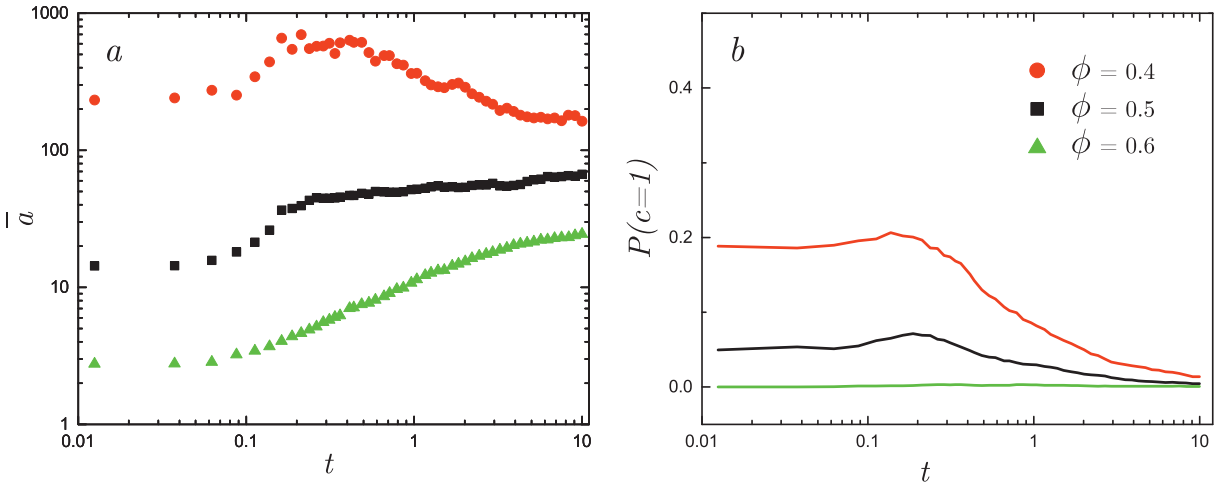

Figure 6.4: (a) Mean void area, $\bar{a}$, as a function of time, t for three samples at surface coverages of $\phi = 0.4, 0.5$, and 0.6 respectively, all subject to a magnetic field $B = 1.55$ mT. (b) The fractions of singly coordinated particles as a function of time for the same sample represented in (a).

6.4.2 Singly coordinated particles

Next, we consider the coordination number statistics of network formation. In particular we will start by focusing on the fraction of 1 coordinate particles, $P(c = 1)$. Singly coordinated particles are of particular interest as they represent the ends of chains. As such they are a key structural feature that distinguishes between the pathways corresponding to monotonic growth of the void area and non-monotonic growth of the void area. We expect the fraction of chain ends to be significant when the low concentration, non-monotonic pathway is present, and insignificant when the high concentration, monotonic pathway is present. In figure 6.4*b* we plot the fraction of 1 coordinate particles, $P(c = 1)$, against time for samples with concentrations of $\phi = 0.4$, $\phi = 0.5$, and $\phi = 0.6$. For $\phi = 0.4$, we see that at short times there is a significant proportion of 1 coordinate particles indicating that the low concentration, non-monotonic pathway is present. At late times, $t \approx 10$ s, the fraction of 1 coordinate particles diminishes to a negligible level as a percolating system is regained and the mean void area starts to grow as a power law, consistent with the higher concentration takes, see figure 6.4*a*. For $\phi = 0.5$, the fraction of one coordinate particles is small but significant, again showing the network formation at this concentration occurs via a non-monotonic pathway. The chain ends aggregate and the fraction of one coordinate particles decays becoming insignificant at a time earlier than for the $\phi = 0.4$ sample. Consistent with this observation we see in figure 6.4*a* that the mean void area regains its power law growth behaviour at a correspondingly earlier time. For $\phi = 0.6$, we expect to

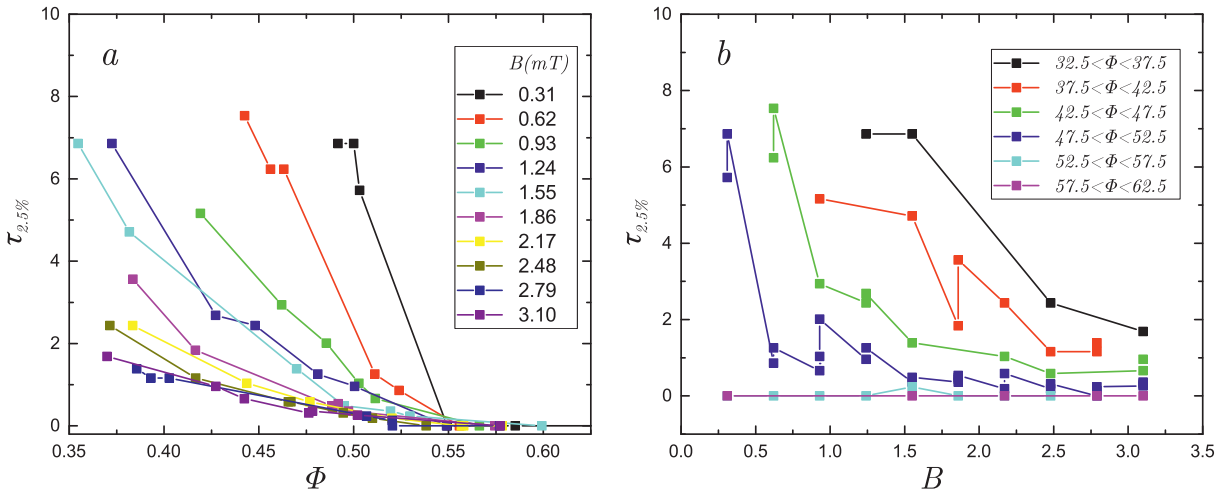

Figure 6.5: (a) ϕ vs $t_{2.5\%}$ for different field strengths. (b) B vs $t_{2.5\%}$, binned into groups of different surface coverages.

observe a percolating network at all times. Accordingly, there is no significant fraction of singly coordinate particles at any time, which confirms that the fraction of 1 coordinate particles is a good microscopic fingerprint of the low-concentration coarsening mechanism. As such it can be used to locate the transition between the two pathways.

To probe the crossover between the pathways corresponding to monotonic growth and non-monotonic growth of the void area, we arbitrarily define the time $\tau_{2.5\%}$ to be the latest time at which we observe $P(c = 1) \geq 0.025$. In light of the observations about the fraction of singly coordinated particles then for high area fractions, for which $P(c = 1)$ is small at all times, $\tau_{2.5\%}$ will be zero. For concentrations where we initially see a significant population of chain ends, i.e. 1 coordinate particles, before crossing over into network behaviour, $\tau_{2.5\%}$ can be interpreted as the crossover time between the two mechanisms. At lower concentrations where significant chain like formations occur at all times, $\tau_{2.5\%}$ will be limited by the length of the experiment ($\approx 10s$).

Figure 6.5 shows the crossover times for 70 experiments with concentrations in the range $0.35 < \phi < 0.6$ and fields in the range $0.3 < B < 3.1$ mT. In the previous chapter we found that this crossover occurred at a concentration between $\phi = 0.53$, and $\phi = 0.59$, section 5.4.4. Considering $\tau_{2.5\%}$ as a function of ϕ, shown in figure 6.5a, we find that all takes at or below $\phi = 0.525$ - 0.55 are chain like for at least some of the experiment. Lower concentration experiments are chain like for longer as the mean distance between chain ends is greater and the onset of lateral aggregation and percolation is delayed. We have measured the area fraction

at which the transition in pathway occurs in two ways, first from the growth of mean void area, figure 5.23*a*, and then through $\tau_{2.5\%}$, figure 6.5. We find that the transition concentrations measured in both are in the same range, confirming the applicability of our arbitrarily defined timescale to the microscopic characterisation of these pathways. The time scale is also strongly field dependent, as shown in figure 6.5*b*, where we plot $\tau_{2.5\%}$ as a function of the magnetic field strength, B. We find that stronger fields accelerate the clustering process due to the larger forces acting between particles. Importantly, the field strength does not affect which pathway occurs, only the timescales are influenced. While this simple analysis is sensitive to the exact definition of the $\tau_{2.5\%}$, it does provide an unambiguous definition of the transition in growth pathway based on the microscopic property of coordination number.

6.4.3 Coordination number distributions

In figure 6.6 we show $P(c)$ as a function of time for the full range of coordination numbers for three samples at surface coverages of $\phi = 0.4, 0.5$, and 0.6, subject to a magnetic field $B = 1.55$ mT. In figure 6.6*a* and *b*, $\phi = 0.4$ and $\phi = 0.5$ respectively, we see a steady rise of 4 coordinate particles with a corresponding decrease in the 2 coordinate particles due to the lateral aggregation of 1 particle thick chains. For the $\phi = 0.5$ sample, figure 6.6*b*, we find that the fraction of 3 coordinate particles decreases but with a slower rate than the increase of 4 coordinated particles. This is evidence of a defect driven mechanism in which the strong interactions of defects generate anchoring points between fibers, leading to the zippering of these chains, consistent with previous observations [22, 88]. For the $\phi = 0.4$ sample, figure 6.6*a*, a decay of 3 coordinate particles is not present. From this we conclude that defects are being created at the same rate as they are being annihilated as a result of the aggregation of chain ends with the sides of fibers. For the higher concentration sample, $\phi = 0.6$, figure 6.6c, the fraction of 2 and 3 coordinate particles decrease but, in contrast to the lower concentration samples, this is matched by a rise in 6 coordinate particles. This is because there are many fibers of at least 2 particles wide so, as 1 particle wide chains laterally aggregate with these, the number of 4 coordinate particles is conserved and 6 coordinate clusters are formed at the expense of 2 coordinate chains.

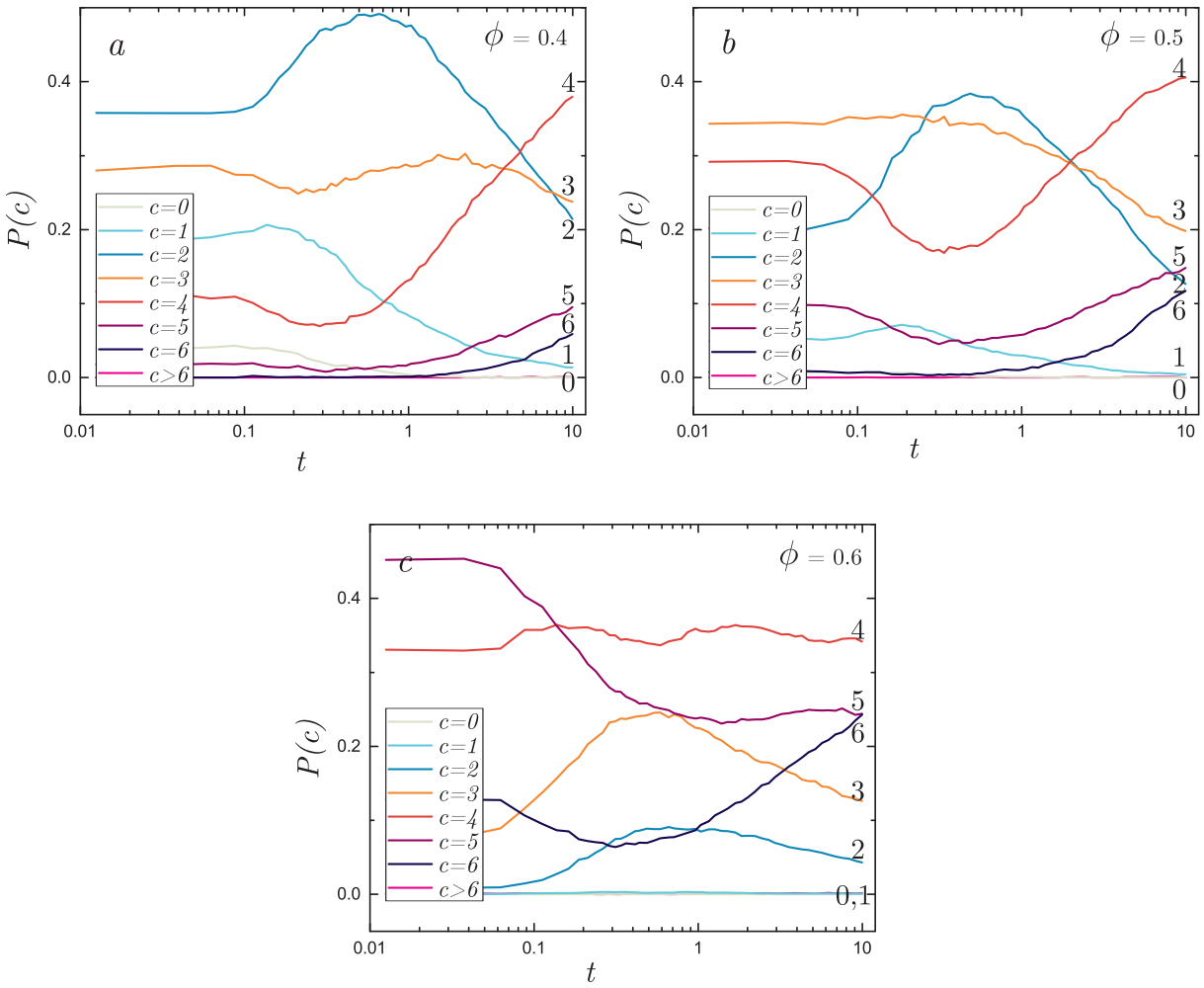

Figure 6.6: Fractions of all coordination numbers as a function of time (a) for a $\phi = 0.4$ sample, (b) for a $\phi = 0.5$ sample, and (c) for a $\phi = 0.6$ sample. All samples are subject to a magnetic field $B = 1.55$ mT. These are the same experiments for which the mean area against time was given in figure 6.4*a*

6.4.4 Links to random fiber theory

In the theory section of this chapter, section 6.2, we described the particle network in terms of a line process in which a random selection of the voids are filled, figure 6.2. In this scheme 6 coordinate particles are filled voids, chains of 2 and 4 coordinate particles are segments, and all other coordination numbers act as nodes and junctions between segments. In figure 6.7*a* we show an example image with particles coloured according to these coordination number classifications. In figure 6.7*b* we show only the 6 coordinate particles where they are coloured according to which cluster they belong to. In figure 6.7*c* we show only the 2 and 4 coordinate particles where different chains are given different colours.

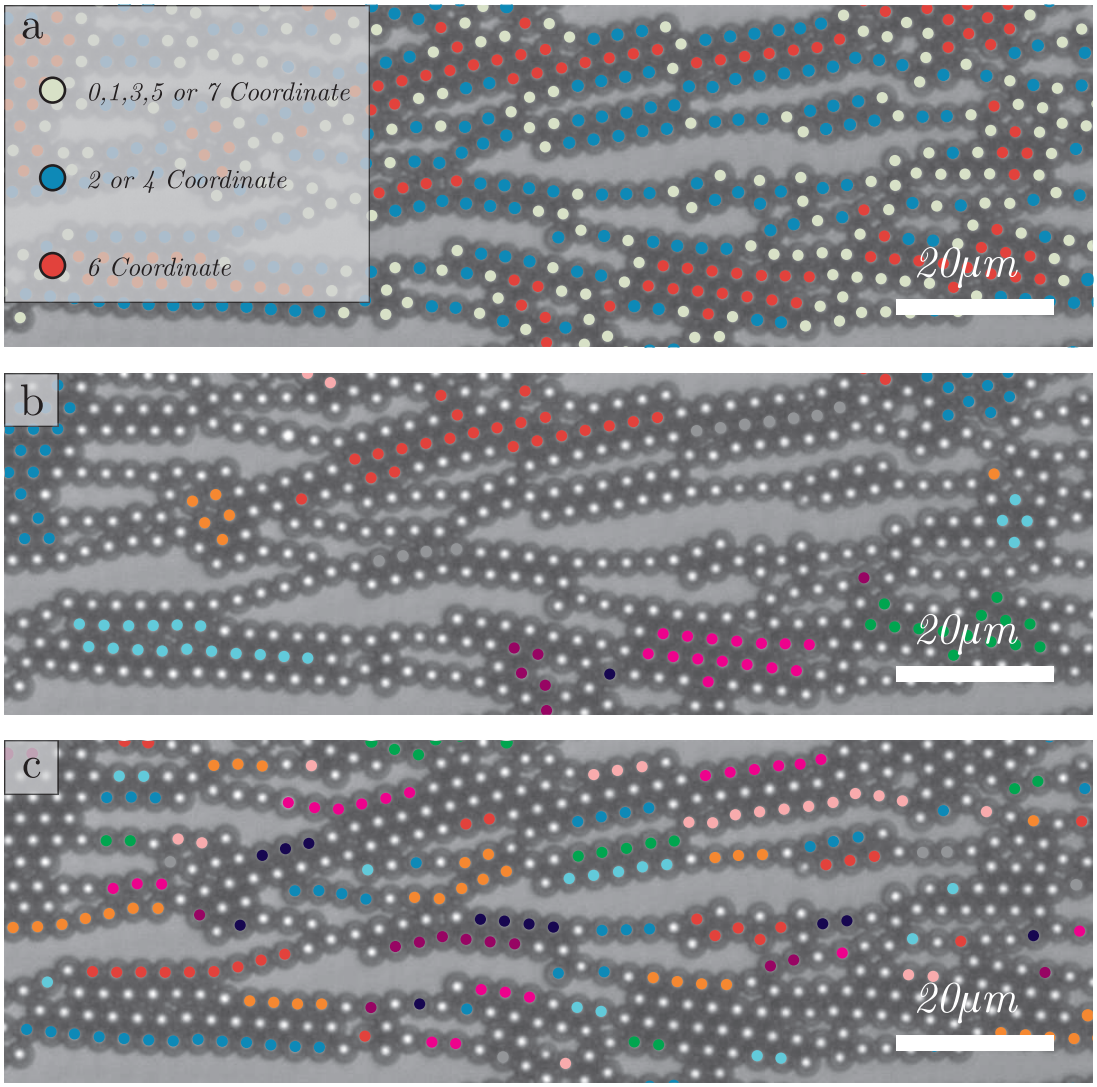

Figure 6.7: A snapshot of a sample with $\phi = 0.63$, $B = 1.55$ mT at a time $t = 10$ s after the application of the magnetic field. (a) Particles are coloured according to the their coordination number. (b) Only the 6 coordinate particles are coloured, the colour is different for particles belonging to different clusters, clusters are identified as outline in section 6.3. (c) Only particles with coordination numbers of 2 or 4 are shown. They are coloured according to which chain they belong to, chains are identified as outline in section 6.3.

Having described clusters of 6 coordinate particles as resulting from randomly filling voids in a line process, figure 6.2*a*, we expect the distribution of areas of $c = 6$ clusters to be drawn from the same distribution as the void areas. We confirm this by plotting the mean $c = 6$ cluster area, $\bar{a}_6$, against the standard deviation, $\sigma(a_6)$, as shown in figure 6.8*a*. We find that the coefficient of variation is constant ($cv = 1.73$) and consistent with both the coefficient of variation for the unfilled void areas ($cv = 1.77$, figure 6.3), and with that predicted by random fiber theory ($cv = 1.73$, table 5.1). The data are averaged over all experiments confirming that

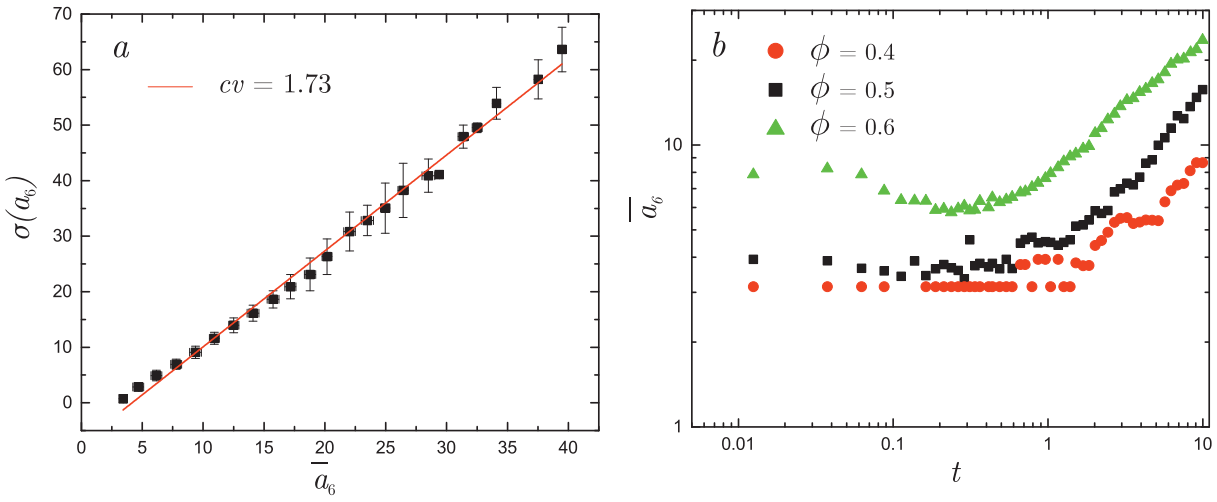

Figure 6.8: (a) The mean area of clusters of $c = 6$ particles, $\bar{a}_6$, against the standard deviation of these areas, $\sigma(a_6)$. (b) The mean area of clusters of $c = 6$ particles, $\bar{a}_6$, against time, t.

in the full range of concentrations and magnetic field strengths both filled and unfilled voids are distributed in the same way. In figure 6.8*b* we plot the mean $c = 6$ cluster area, $\bar{a}_6$, against time for $\phi = 0.4$, 0.5, and 0.6, and find power law growth at late times. At early times the minimum mean area is the area of a single particle, note that the areas are reported in units of the particle radius squared. Unlike the unfilled voids, figure 6.4*a*, we do not see evidence of a monotonic pathway and a non-monotonic pathway since clusters of 6 coordinate particles only evolve with the coarsening of a percolating network.

Next, we consider the structures of the 2 and 4 coordinate particles, which correspond to the segments of a line process. We have described the chains of 2 and 4 coordinate particles as the segments of a line process. In section 5.2.1 we showed that in an ideal random fiber process we expect segment lengths to be distributed according to a Gamma function, equation 5.6, with a coefficient of variation of unity, table 5.1. In section 5.4.1 we experimentally measured the segment length distribution and found the coefficient of variation to be $cv = 1.29$, table 5.2. Here, we plot the mean segment length, $\bar{g}_{2,4}$, against the standard deviation, $\sigma(g_{2,4})$, in figure 6.9*a* and find that the coefficient of variation is $cv = 1.2$. This coefficient of variation is consistent with our experimental observations in chapter 5, indicating that chains of 2 and 4 coordinate particles are indeed a valid measure of the segment lengths of our network. In figure 6.9*b* we plot the mean segment length against time and observe monotonic growth. The highest concentration, $\phi = 0.6$, appears to show only a single growth regime. Lower concentrations, $\phi = 0.4$ and $\phi = 0.5$, exhibit a 2-step growth process. This is consistent with the preceding discussions of

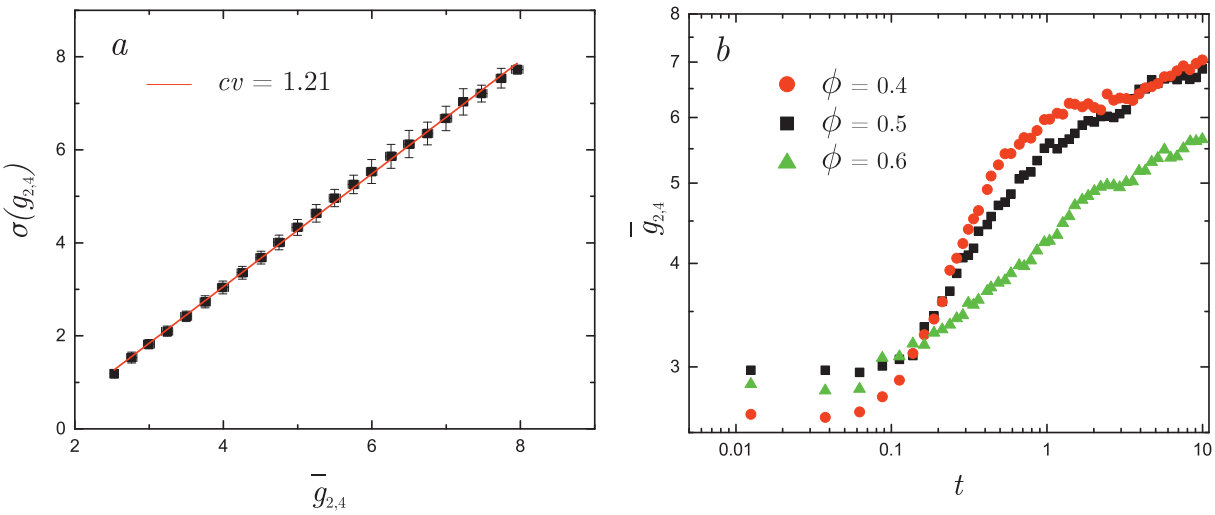

Figure 6.9: (a) The standard deviation of clusters of particles with $c = 2$ and 4, $\sigma(g_{2,4})$, against the mean of these lengths, $\bar{g}_{2,4}$. (b) $\bar{g}_{2,4}$ as a function of time, t.

the crossover between a low concentration pathway of aggregating free chain ends followed by a network coarsening regime, and the high concentration pathway of network coarsening at all times.

We have established that we have two distinct sets of areas, unfilled voids and clusters of 6 coordinate particles, that are defined by the same network of random lines, see figure 6.2 for reference. We can gather these together in a single parameter, $\bar{a}_{\text{all}}$, which is the average area when both filled and unfilled voids are considered together. In equation 6.4 we predict how the area $\bar{a}_{\text{all}}$ depends on $P(c = 6)$, the fraction of 6 coordinate particles. In figure 6.10 we plot the experimental area, $\bar{a}_{\text{all}}$, against the predicted area calculated using equation 6.4, $\bar{a}_{(\text{eq:6.4})}$, with the experimental values of $P(c = 6)$. In figure 6.10 the data are averaged over all times and for all sample with $\phi > 0.55$. Clearly, we find a linear relationship, which confirms that the proposed theory links the microscopic property of coordination numbers and the mesoscopic structural properties of the network indicating that coordination numbers fulfill the structural roles outlined in section 6.2.

There is a short initial period in which the theory breaks down, which corresponds to the early times where a network has not been established yet. Choosing, by eye, to fit only values above a mean area of 12 a^2 with a linear equation, we find that $\bar{a}_{(\text{eq:6.4})} = 0.62\bar{a}_{\text{all}} + 4.3$. The gradient is less than unity indicating that we are underestimating the area of voids, and therefore overestimating the total line length in our system, τ in equation 6.3. A key assumption

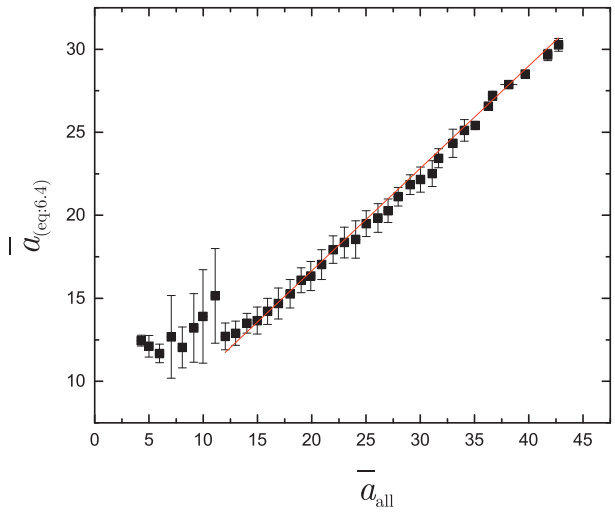

Figure 6.10: $\bar{a}_{\text{all}}$ the average area when both cluster of 6 coordinate particles and voids are considered together against the area predicted from equation 6.4.

that we made in the derivation of equation 6.4 was that all particles that were not 6 coordinate particles contribute the same length to τ. This is not always the case however, in particular 4 coordinate particles exist in two groups as shown in figure 6.2*c* and *d*: (I) 4 coordinate particles can either define the border of a filled void on one side and an unfilled void on the other sider or (II) form 2 particle wide chains that separate unfilled voids on each side. In the case of 4 coordinate particles forming a 2 particle wide chains their contribution to the total line length should be halved. By setting the gradient of the predicted area against the observed area to 1 we find that the contribution of $P(c = 4)$ to the total line length is smaller. In particular we find that $\tau = 2\phi(P(c = 2) + P(c = 3) + 0.76P(c = 4) + P(c = 5))/\pi a$ instead of the expression given in equation 6.2. Nevertheless, this demonstrates the link between coordination numbers and structural features and the interplay of local structure and mesoscopic structure.

6.5 Conclusion

In this chapter we have presented a novel link between the coordination number statistics of networks and the network structural features such as $\bar{a}$. Singly coordinated particles are shown to be a powerful diagnostic tool for the pathway of network growth. A robust timescale, $\tau_{2.5\%}$, is proposed which provides a microscopic signature of the pathways, identified in chapter 5, in which the mean void area transitions from growing as a power law to a non-monotonic growth

profile. Identifying the structural roles of all coordination numbers, we propose a theoretical link between random line processes and the coordination numbers of particles. This theory is confirmed experimentally and thereby provides a quantitative link between the microscopic property of coordination numbers and the mesoscopic property of void area.

Acknowledgements

This work was carried out in collaboration with William Sampson. We also thank David Robinson and Mark Wilson for many useful discussions.

Appendix

$\langle L \rangle$ collapse by theory - Chapter 3

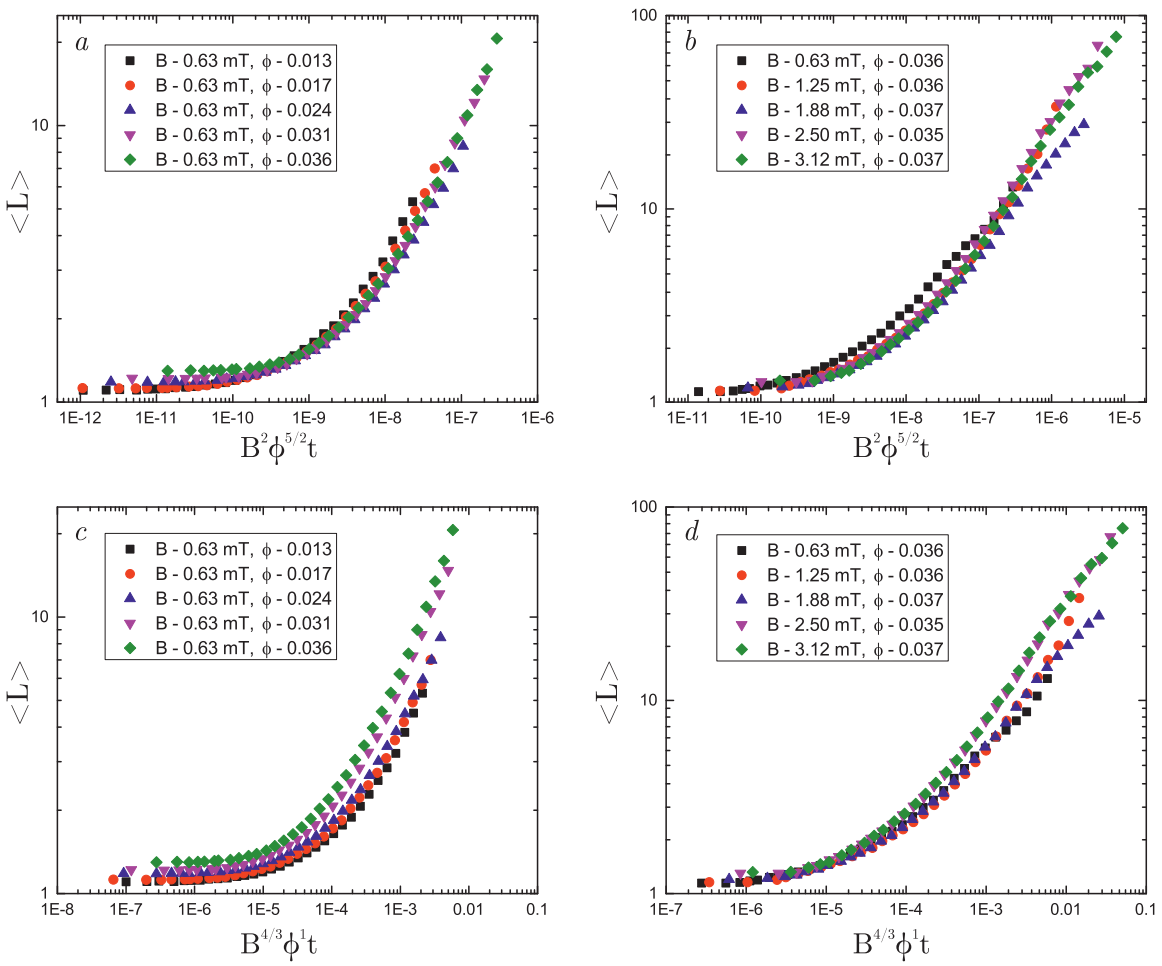

Figure A.1: The mean cluster size, $\langle L \rangle$, as a function of the rescaled time shown on the x axis. (a) and (b) correspond to a deterministic rescaling while (c) and (d) corresponds to a diffusive rescaling. In (a) and (c) the experimental runs are at a constant magnetic field, $B = 0.63$ mT. In (b) and (d) the runs are at a constant packing fraction, $\phi \approx 0.036$. Note that the data presented here is the same as in Figure 3.3, chapter 3.

In chapter 3 we investigated the magnetic field induced formation of chains in low concentration suspensions of gravity confined paramagnetic particles. We outlined a diffusive theory of aggregation and a deterministic theory, section 3.2.2 and section 3.2.3 respectively. From these we predicted a time rescaling that would be expected to cause data collapse in each case, equation 3.5 and equation 3.11 respectively. Here a selection of growth curves are shown rescaled by these theoretical predictions to corroborate the conclusions of chapter 3, in particular that a deterministic mechanism is at play. This is conclusively shown in the concentration dependence but only ambiguously shown in the magnetic field dependence, figure A.1. *a* and *b* correspond to collapse by the deterministic mechanism, $t^*_{\mathrm{DET}} \sim B^{-2}\phi^{-5/2}$. *c* and *d* correspond to the diffusive mechanism, $t^*_{\mathrm{DIF}} \sim B^{-4/3}\phi^{-1}$. Panels *a* and *c* represent experimental runs of constant magnetic field strength, $B = 0.63$ mT, but different surface coverages. Panels *b* and *d* represent experimental runs of constant surface coverage, $\phi \approx 0.036$, but different magnetic field strengths.

Bibliography

[1] Daniel C Mattis. History of magnetism. In *The Theory of Magnetism I*, pages 1–38. Springer, 1981.

[2] William Gilbert. *De magnete*. Courier Corporation, 1958.

[3] Ronald T Merrill. *Our magnetic earth: the science of geomagnetism*. University of Chicago Press, 2010.

[4] Peter Wasilewski and Günther Kletetschka. Lodestone: Natures only permanent magnet-what it is and how it gets charged. *Geophysical Research Letters*, 26(15):2275–2278, 1999.

[5] Derek R Lovley, John F Stolz, Gordon L Nord, Elizabeth JP Phillips, et al. Anaerobic production of magnetite by a dissimilatory iron-reducing microorganism. *Nature*, 330(6145):252–254, 1987.

[6] Richard Blakemore. Magnetotactic bacteria. *Science*, 190(4212):377–379, 1975.

[7] Hervé Cadiou and Peter A McNaughton. Avian magnetite-based magnetoreception: a physiologist's perspective. *Journal of the Royal Society Interface*, 7(Suppl 2):S193–S205, 2010.

[8] Gerrit L Verschuur. *Hidden Attraction: The Mystery and History of Magnetism*. Oxford University Press, USA, 1993.

[9] Denis Le Bihan, Jean-François Mangin, Cyril Poupon, Chris A Clark, Sabina Pappata, Nicolas Molko, and Hughes Chabriat. Diffusion tensor imaging: concepts and applications. *Journal of Magnetic Resonance Imaging*, 13(4):534–546, 2001.

[10] Hyung-Woo Lee, Ki-Chan Kim, and Ju Lee. Review of maglev train technologies. *Magnetics, IEEE Transactions on*, 42(7):1917–1925, 2006.

[11] HP Laqua et al. Commissioning and first plasma operation at the wendelstein 7-x stellarator. In *25th International Toki Conference (ITC 25)*, 2015.

[12] James D Watson. *The double helix: the discovery of the structure of DNA*. Weidenfeld & Nelson, 1968.

[13] Ana C Mendes, Erkan T Baran, Rui L Reis, and Helena S Azevedo. Self-assembly in nature: using the principles of nature to create complex nanobiomaterials. *Wiley Interdisciplinary Reviews: Nanomedicine and Nanobiotechnology*, 5(6):582–612, 2013.

[14] Yadong Yin, Yu Lu, Byron Gates, and Younan Xia. Template-assisted self-assembly: a practical route to complex aggregates of monodispersed colloids with well-defined sizes, shapes, and structures. *Journal of the American Chemical Society*, 123(36):8718–8729, 2001.

[15] Jeffrey Bodycomb, Yoshinori Funaki, Kohtaro Kimishima, and Takeji Hashimoto. Single-grain lamellar microdomain from a diblock copolymer. *Macromolecules*, 32(6):2075–2077, 1999.

[16] Eric M Furst. Directed self-assembly. *Soft Matter*, 9(38):9039–9045, 2013.

[17] Willis M Winslow. Induced fibration of suspensions. *Journal of Applied Physics*, 20(12):1137–1140, 1949.

[18] Jacob Rabinow. Magnetic fluid torque and force transmitting device, November 20 1951.

[19] Seth Fraden, Alan J Hurd, and Robert B Meyer. Electric-field-induced association of colloidal particles. *Physical review letters*, 63(21):2373, 1989.

[20] A. T. Skjeltorp. Ordering phenomena of particles dispersed in magnetic fluids. *Journal of Applied Physics*, 57(8):3285–3290, 1985.

[21] Joanne HE Promislow, Alice P Gast, and Marc Fermigier. Aggregation kinetics of paramagnetic colloidal particles. *The Journal of chemical physics*, 102(13):5492–5498, 1995.

[22] Marc Fermigier and Alice P Gast. Structure evolution in a paramagnetic latex suspension. *Journal of Colloid and Interface Science*, 154(2):522–539, 1992.

[23] Le He, Mingsheng Wang, Jianping Ge, and Yadong Yin. Magnetic assembly route to colloidal responsive photonic nanostructures. *Accounts of Chemical Research*, 45(9):1431–1440, 2012.

[24] Ronald G Larson. *The structure and rheology of complex fluids*, volume 4. Oxford University Press, New York, 1999.

[25] Abdul-Ghani Olabi and Artur Grunwald. Design and application of magneto-rheological fluid. *Materials & design*, 28(10):2658–2664, 2007.

[26] Ioan Bica, Ying Dan Liu, and Hyoung Jin Choi. Physical characteristics of magnetorheological suspensions and their applications. *Journal of Industrial and Engineering Chemistry*, 19(2):394–406, 2013.

[27] Juan de Vicente, Daniel J Klingenberg, and Roque Hidalgo-Alvarez. Magnetorheological fluids: a review. *Soft Matter*, 7(8):3701–3710, 2011.

[28] F Donado, U Sandoval, and JL Carrillo. Kinetics of aggregation in non-brownian magnetic particle dispersions in the presence of perturbations. *Physical Review E*, 79(1):011406, 2009.

[29] Jordi Faraudo, Jordi S Andreu, Carles Calero, and Juan Camacho. Predicting the self-assembly of superparamagnetic colloids under magnetic fields. *Advanced Functional Materials*, 2016.

[30] Pietro Tierno, Ramanathan Muruganathan, and Thomas M Fischer. Viscoelasticity of dynamically self-assembled paramagnetic colloidal clusters. *Physical Review Letters*, 98(2):028301, 2007.

[31] Pietro Tierno, Josep Claret, Francesc Sagués, and Andrejs Cēbers. Overdamped dynamics of paramagnetic ellipsoids in a precessing magnetic field. *Physical Review E*, 79(2):021501, 2009.

[32] James E Martin and Alexey Snezhko. Driving self-assembly and emergent dynamics in colloidal suspensions by time-dependent magnetic fields. *Reports on Progress in Physics*, 76(12):126601, 2013.

[33] G Bossis, O Volkova, S Lacis, and A Meunier. Magnetorheology: fluids, structures and rheology. In *Ferrofluids*, pages 202–230. Springer, 2002.

[34] James E Martin, Judy Odinek, Thomas C Halsey, and Randall Kamien. Structure and dynamics of electrorheological fluids. *Physical Review E*, 57(1):756, 1998.

[35] Joanne HE Promislow and Alice P Gast. Magnetorheological fluid structure in a pulsed magnetic field. *Langmuir*, 12(17):4095–4102, 1996.

[36] Joanne HE Promislow and Alice P Gast. Low-energy suspension structure of a magnetorheological fluid. *Physical Review E*, 56(1):642, 1997.

[37] James W Swan, Jonathan L Bauer, Yifei Liu, and Eric M Furst. Directed colloidal self-assembly in toggled magnetic fields. *Soft Matter*, 10(8):1102–1109, 2014.

[38] James W Swan, Paula A Vasquez, Peggy A Whitson, E Michael Fincke, Koichi Wakata, Sandra H Magnus, Frank De Winne, Michael R Barratt, Juan H Agui, Robert D Green, et al. Multi-scale kinetics of a field-directed colloidal phase transition. *Proceedings of the National Academy of Sciences*, 109(40):16023–16028, 2012.

[39] Jonathan L Bauer, Yifei Liu, Martin J Kurian, James W Swan, and Eric M Furst. Coarsening mechanics of a colloidal suspension in toggled fields. *The Journal of chemical physics*, 143(7):074901, 2015.

[40] VV Ishtchenko, KD Huddersman, and RF Vitkovskaya. Part 1. production of a modified pan fibrous catalyst and its optimisation towards the decomposition of hydrogen peroxide. *Applied Catalysis A: General*, 242(1):123–137, 2003.

[41] Christian Burger, Benjamin S Hsiao, and Benjamin Chu. Nanofibrous materials and their applications. *Annu. Rev. Mater. Res.*, 36:333–368, 2006.

[42] Krishan Kumar Chawla. *Fibrous materials*. Cambridge university press, 2005.

[43] Raul Fangueiro. *Fibrous and composite materials for civil engineering applications*. Elsevier, 2011.

[44] Zuwei Ma, Masaya Kotaki, Ryuji Inai, and Seeram Ramakrishna. Potential of nanofiber matrix as tissue-engineering scaffolds. *Tissue engineering*, 11(1-2):101–109, 2005.

[45] Zheng-Ming Huang, Y-Z Zhang, M Kotaki, and S Ramakrishna. A review on polymer nanofibers by electrospinning and their applications in nanocomposites. *Composites science and technology*, 63(15):2223–2253, 2003.

[46] William Bailey Russel, Dudley Albert Saville, and William Raymond Schowalter. *Colloidal dispersions*. Cambridge university press, 1992.

[47] Wilson Poon. Colloids as big atoms. *Science*, 304(5672):830–831, 2004.

[48] PN Pusey and W Van Megen. Phase behaviour of concentrated suspensions of nearly hard colloidal spheres. *Nature*, 320(6060):340–342, 1986.

[49] Stefano Sacanna, Mark Korpics, Kelvin Rodriguez, Laura Colón-Meléndez, Seung-Hyun Kim, David J Pine, and Gi-Ra Yi. Shaping colloids for self-assembly. *Nature Communications*, 4:1688, 2013.

[50] Yong Wang, Xiaowen Su, Panshuang Ding, Shan Lu, and Huaping Yu. Shape-controlled synthesis of hollow silica colloids. *Langmuir*, 29(37):11575–11581, 2013.

[51] Laura Rossi, Stefano Sacanna, William TM Irvine, Paul M Chaikin, David J Pine, and Albert P Philipse. Cubic crystals from cubic colloids. *Soft Matter*, 7(9):4139–4142, 2011.

[52] Anke Kuijk, Alfons van Blaaderen, and Arnout Imhof. Synthesis of monodisperse, rodlike silica colloids with tunable aspect ratio. *Journal of the American Chemical Society*, 133(8):2346–2349, 2011.

[53] Stefano Sacanna, WTM Irvine, Paul M Chaikin, and David J Pine. Lock and key colloids. *Nature*, 464(7288):575–578, 2010.

[54] Sharon C Glotzer and Michael J Solomon. Anisotropy of building blocks and their assembly into complex structures. *Nature materials*, 6(8):557–562, 2007.

[55] Joost R Wolters, Guido Avvisati, Fabian Hagemans, Teun Vissers, Daniela J Kraft, Marjolein Dijkstra, and Willem K Kegel. Self-assembly of mickey mouse shaped colloids into tube-like structures: experiments and simulations. *Soft matter*, 11(6):1067–1077, 2015.

[56] Qian Chen, Sung Chul Bae, and Steve Granick. Directed self-assembly of a colloidal kagome lattice. *Nature*, 469(7330):381–384, 2011.

[57] Daniela J Kraft, Ran Ni, Frank Smallenburg, Michiel Hermes, Kisun Yoon, David A Weitz, Alfons van Blaaderen, Jan Groenewold, Marjolein Dijkstra, and Willem K Kegel. Surface roughness directed self-assembly of patchy particles into colloidal micelles. *Proceedings of the National Academy of Sciences USA*, 109(27):10787–10792, 2012.

[58] D. Fennell Evans and Hakån Wennerström. *The colloidal domain: Where physics, chemistry, biology, and technology meet. 2nd ed.* Wiley-VCH, 1999.

[59] Ye Yang, Lu Gao, Gabriel P Lopez, and Benjamin B Yellen. Tunable assembly of colloidal crystal alloys using magnetic nanoparticle fluids. *ACS nano*, 7(3):2705–2716, 2013.

[60] Mark Wilson, Avishek Kumar, David Sherrington, and MF Thorpe. Modeling vitreous silica bilayers. *Physical Review B*, 87(21):214108, 2013.

[61] Mary-Jane Gething and Joseph Sambrook. Protein folding in the cell. *Nature*, 355(6355):33–45, 1992.

[62] Stephen Mann. Self-assembly and transformation of hybrid nano-objects and nanostructures under equilibrium and non-equilibrium conditions. *Nature Materials*, 8(10):781, 2009.

[63] Douglas Philp and J. Fraser Stoddart. Self-assembly in natural and unnatural systems. *Angew. Chem. Int. Ed.*, 35(11):1154, 1996.

[64] Jean-Marie Lehn. Toward self-organization and complex matter. *Science*, 295(5564):2400–2403, 2002.

[65] Natalie Arkus, Vinothan N. Manoharan, and Michael P. Brenner. Minimal energy clusters of hard spheres with short range attractions. *Physical Review Letters*, 103:118303, Sep 2009.

[66] Guangnan Meng, Natalie Arkus, Michael P Brenner, and Vinothan N Manoharan. The free-energy landscape of clusters of attractive hard spheres. *Science*, 327(5965):560–563, 2010.

[67] Andrew I Campbell, Valerie J Anderson, Jeroen S van Duijneveldt, and Paul Bartlett. Dynamical arrest in attractive colloids: The effect of long-range repulsion. *Physical Review Letters*, 94(20):208301, 2005.

[68] Matti M van Schooneveld, Volkert W A de Villeneuve, Roel P A Dullens, Dirk G. A. L. Aarts, Mirjam E Leunissen, and Willem K Kegel. Structure, stability, and formation pathways of colloidal gels in systems with short-range attraction and long-range repulsion. *Journal of Physical Chemistry B*, 113(14):4560, 2009.

[69] Barbara Ruzicka, Emanuela Zaccarelli, Laura Zulian, Roberta Angelini, Michael Sztucki, Abdellatif Moussaïd, Theyencheri Narayanan, and Francesco Sciortino. Observation of empty liquids and equilibrium gels in a colloidal clay. *Nature Materials*, 10(1):56–60, 2011.

[70] Olga Markova, Jonathan Alberts, Edwin Munro, and Pierre-François Lenne. Clustering of low-valence particles: Structure and kinetics. *Physical Review E*, 90(2):022301, 2014.

[71] Pablo F Damasceno, Michael Engel, and Sharon C Glotzer. Predictive self-assembly of polyhedra into complex structures. *Science*, 337(6093):453–457, 2012.

[72] Jean-Marie Lehn. *Supramolecular Chemistry: Concepts and Perspectives*. Wiley-VCH, 1995.

[73] Jean Philibert. One and a half century of diffusion: Fick, einstein, before and beyond. *Diffusion Fundamentals*, 4(6):1–19, 2006.

[74] Albert Einstein. Zur theorie der brownschen bewegung. *Annalen der physik*, 324(2):371–381, 1906.

[75] Eric R Weeks. Soft jammed materials. *ER Maruyama, S. & Tokuyama, M.(Eds.), Statistical Physics of Complex Fluids*, pages 243–255, 2007.

[76] BV Derjaguin, L Landau, et al. Theory of the stability of strongly charged lyophobic sols and of the adhesion of strongly charged particles in solutions of electrolytes. *Acta physicochim. URSS*, 14(6):633–662, 1941.

[77] Evert Johannes Willem Verwey, J Th G Overbeek, and Jan Theodoor Gerard Overbeek. *Theory of the stability of lyophobic colloids*. Courier Corporation, 1999.

[78] Jacob N Israelachvili. *Intermolecular and surface forces: revised third edition*. Academic press, 2011.

[79] Jessica A Weiss, Amy E Larsen, and David G Grier. Interactions, dynamics, and elasticity in charge-stabilized colloidal crystals. *The Journal of Chemical Physics*, 109(19):8659–8666, 1998.

[80] David Jeffrey Griffiths and Reed College. *Introduction to electrodynamics*, volume 3. prentice Hall Upper Saddle River, NJ, 1999.

[81] V Blickle, Dušan Babič, and Clemens Bechinger. Evanescent light scattering with magnetic colloids. *Applied Physics Letters*, 87(10):101102, 2005.

[82] Anand Yethiraj. Tunable colloids: control of colloidal phase transitions with tunable interactions. *Soft Matter*, 3(9):1099–1115, 2007.

[83] Jordi Faraudo, Jordi S Andreu, and Juan Camacho. Understanding diluted dispersions of superparamagnetic particles under strong magnetic fields: a review of concepts, theory and simulations. *Soft Matter*, 9(29):6654–6664, 2013.

[84] Eric M Furst and Alice P Gast. Dynamics and lateral interactions of dipolar chains. *Physical Review E*, 62(5):6916–6925, 2000.

[85] Thomas C Halsey and Will Toor. Structure of electrorheological fluids. *Physical review letters*, 65(22):2820, 1990.

[86] Sibani Lisa Biswal and Alice P Gast. Rotational dynamics of semiflexible paramagnetic particle chains. *Physical Review E*, 69(4):041406, 2004.

[87] Georges Bossis, L Iskakova, V Kostenko, and Andrey Zubarev. Kinetics aggregation of magnetic suspensions. *Physica A: Statistical Mechanics and its Applications*, 390(14):2655–2663, 2011.

[88] James E Martin, Kimberly M Hill, and Chris P Tigges. Magnetic-field-induced optical transmittance in colloidal suspensions. *Physical Review E*, 59(5):5676, 1999.

[89] Eric M Furst and Alice P Gast. Micromechanics of magnetorheological suspensions. *Physical Review E*, 61(6):6732–6739, 2000.

[90] Georges Bossis, Pascal Lançon, Alain Meunier, L Iskakova, V Kostenko, and Andrey Zubarev. Kinetics of internal structures growth in magnetic suspensions. *Physica A: Statistical Mechanics and its Applications*, 392(7):1567–1576, 2013.

[91] Brajalal Sinha, S Anandakumar, Sunjong Oh, and CheolGi Kim. Micro-magnetometry for susceptibility measurement of superparamagnetic single bead. *Sensors and Actuators A: Physical*, 182:34–40, 2012.

[92] J. C. Crocker and D. G. Grier. Methods of digital video microscopy for colloidal studies. *Journal of Colloid and Interface Science*, 179(1):298–310, 1996.

[93] P Domínguez-García and MA Rubio. Jchainsanalyser: an imagej-based stand-alone application for the study of magneto-rheological fluids. *Computer Physics Communications*, 180(10):1956–1960, 2009.

[94] Pierre Soille. *Morphological image analysis: principles and applications*. Springer Science & Business Media, 2013.

[95] Hetal J Vala and Astha Baxi. A review on otsu image segmentation algorithm. *International Journal of Advanced Research in Computer Engineering & Technology (IJARCET)*, 2(2):pp–387, 2013.

[96] Raman Maini and Himanshu Aggarwal. Study and comparison of various image edge detection techniques. *International Journal of Image Processing (IJIP)*, 3(1):1–11, 2009.

[97] Laurent Najman and Michel Schmitt. Geodesic saliency of watershed contours and hierarchical segmentation. *Pattern Analysis and Machine Intelligence, IEEE Transactions on*, 18(12):1163–1173, 1996.

[98] Liviu Octavian Mafteiu-Scai. The bandwidths of a matrix. a survey of algorithms. *Annals of West University of Timisoara-Mathematics*, 52(2):183–223, 2014.

[99] Jozef Černák, Geir Helgesen, and Arne T Skjeltorp. Aggregation dynamics of nonmagnetic particles in a ferrofluid. *Physical Review E*, 70(3):031504, 2004.

[100] Jozef Černák and Geir Helgesen. Aggregation of magnetic holes in a rotating magnetic field. *Physical Review E*, 78(6):061401, 2008.

[101] Randall M Erb, Melissa D Krebs, Eben Alsberg, Bappaditya Samanta, Vincent M Rotello, and Benjamin B Yellen. Beyond diffusion-limited aggregation kinetics in microparticle suspensions. *Physical Review E*, 80(5):051402, 2009.

[102] Gergő Pál, Ferenc Kun, Imre Varga, Dóra Sohler, and Gang Sun. Attraction-driven aggregation of dipolar particles in an external magnetic field. *Physical Review E*, 83(6):061504, 2011.

[103] F Martínez-Pedrero, A El-Harrak, JC Fernández-Toledano, M Tirado-Miranda, Jean Baudry, A Schmitt, Jérôme Bibette, and J Callejas-Fernández. Kinetic study of coupled field-induced aggregation and sedimentation processes arising in magnetic fluids. *Physical Review E*, 78(1):011403, 2008.

[104] F Martínez-Pedrero, M Tirado-Miranda, A Schmitt, and J Callejas-Fernández. Formation of magnetic filaments: A kinetic study. *Physical Review E*, 76(1):011405, 2007.

[105] RE Moctezuma, F Donado, and JL Arauz-Lara. Lateral aggregation induced by magnetic perturbations in a magnetorheological fluid based on non-brownian particles. *Physical Review E*, 88(3):032305, 2013.

[106] P Domínguez-García, Sonia Melle, JM Pastor, and MA Rubio. Scaling in the aggregation dynamics of a magnetorheological fluid. *Physical Review E*, 76(5):051403, 2007.

[107] P Domínguez-García, JM Pastor, and MA Rubio. Aggregation and disaggregation dynamics of sedimented and charged superparamagnetic micro-particles in water suspension. *The European Physical Journal E*, 34(4):1–7, 2011.

[108] G Helgesen, AT Skjeltorp, Paulo Machado Mors, Robert Botet, and Remi Jullien. Aggregation of magnetic microspheres: experiments and simulations. *Physical Review Letter*, 61(15):1736, 1988.

[109] Tomofumi Ukai, Hisao Morimoto, and Toru Maekawa. Cluster-cluster aggregations of superparamagnetic particles in a rotational magnetic field. *Physical Review E*, 83(6):061406, 2011.

[110] Sonia Melle, Oscar G Calderón, Miguel A Rubio, and Gerald G Fuller. Microstructure evolution in magnetorheological suspensions governed by mason number. *Physical Review E*, 68(4):041503, 2003.

[111] Martin Hagenbüchle and Jing Liu. Chain formation and chain dynamics in a dilute magnetorheological fluid. *Applied Optics*, 36(30):7664–7671, 1997.

[112] JJM Janssen, JJM Baltussen, AP Van Gelder, and JAAJ Perenboom. Kinetics of magnetic flocculation. i. flocculation of colloidal particles. *Journal of Physics D: Applied Physics*, 23(11):1447, 1990.

[113] F Martínez Pedrero, M Tirado Miranda, A Schmitt, and J Callejas Fernández. Forming chainlike filaments of magnetic colloids: the role of the relative strength of isotropic and anisotropic particle interactions. *The Journal of Chemical Physics*, 125(8):084706, 2006.

[114] Sonia Melle, Miguel A Rubio, and Gerald G Fuller. Time scaling regimes in aggregation of magnetic dipolar particles: scattering dichroism results. *Physical review letters*, 87(11):115501, 2001.

[115] James E Martin, Judy Odinek, and Thomas C Halsey. Evolution of structure in a quiescent electrorheological fluid. *Physical Review Letters*, 69(10):1524, 1992.

[116] James E Martin and Judy Odinek. Light scattering studies of the electrorheological transition. *Journal of non-crystalline solids*, 172:1135–1141, 1994.

[117] Junaid M Laskar, John Philip, and Baldev Raj. Experimental investigation of magnetic-field-induced aggregation kinetics in nonaqueous ferrofluids. *Physical Review E*, 82(2):021402, 2010.

[118] Daewon Sohn. Kinetic studies of magnetic latex particles' self-assembly under applied magnetic field. *Journal of magnetism and magnetic materials*, 173(3):305–313, 1997.

[119] Eric Climent, Martin R Maxey, and George Em Karniadakis. Dynamics of self-assembled chaining in magnetorheological fluids. *Langmuir*, 20(2):507–513, 2004.

[120] D Liu, MR Maxey, and GE Karniadakis. Simulations of dynamic self-assembly of paramagnetic microspheres in confined microgeometries. *Journal of Micromechanics and Microengineering*, 15(12):2298, 2005.

[121] EKO Hellén, TP Simula, and Mikko J Alava. Dynamic scaling in one-dimensional cluster-cluster aggregation. *Physical Review E*, 62(4):4752, 2000.

[122] M Kolb. Unified description of static and dynamic scaling for kinetic cluster formation. *Physical Review Letters*, 53(17):1653, 1984.

[123] Sasuke Miyazima, Paul Meakin, and Fereydoon Family. Aggregation of oriented anisotropic particles. *Physical Review A*, 36(3):1421, 1987.

[124] Robert Botet, Rémi Jullien, and M Kolb. Hierarchical model for irreversible kinetic cluster formation. *Journal of Physics A: Mathematical and General*, 17(2):L75, 1984.

[125] Tamás Vicsek and Fereydoon Family. Dynamic scaling for aggregation of clusters. *Physical Review Letters*, 52(19):1669, 1984.

[126] M-Carmen Miguel and R Pastor-Satorras. Kinetic growth of field-oriented chains in dipolar colloidal solutions. *Physical Review E*, 59(1):826, 1999.

[127] Howard See and Masao Doi. Aggregation Kinetics in Electro-Rheological Fluids. *J. Phys. Soc. Jpn.*, 60(8):2778, 1991.

[128] Paul Meakin. Diffusion-limited aggregation in three dimensions: results from a new cluster-cluster aggregation model. *Journal of Colloid and Interface Science*, 102(2):491–504, 1984.

[129] Jordi S Andreu, Juan Camacho, and Jordi Faraudo. Aggregation of superparamagnetic colloids in magnetic fields: the quest for the equilibrium state. *Soft Matter*, 7(6):2336–2339, 2011.

[130] Alison E Koser, Nathan C Keim, and Paulo E Arratia. Structure and dynamics of self-assembling colloidal monolayers in oscillating magnetic fields. *Physical Review E*, 88(6):062304, 2013.

[131] Jorge González-Gutiérrez, JL Carrillo-Estrada, and JC Ruiz-Suárez. Nucleation, aggregation, annealing, and disintegration of granular clusters. *Physical Review E*, 89(5):052205, 2014.

[132] Ben Amira Wael, Abid Malek, et al. Dynamic scaling in magnetophoretic separation. *Journal of Applied Physics*, 112(9):094910, 2012.

[133] Yufeng Wang, Yu Wang, Dana R Breed, Vinothan N Manoharan, Lang Feng, Andrew D Hollingsworth, Marcus Weck, and David J Pine. Colloids with valence and specific directional bonding. *Nature*, 491(7422):51–55, 2012.

[134] Manigandan Sabapathy, Sam David Christdoss Pushpam, Madivala G Basavaraj, and Ethayaraja Mani. Synthesis of single and multipatch particles by dip-coating method and self-assembly thereof. *Langmuir*, 31(4):1255–1261, 2015.

[135] Daniela J Kraft, Jan Groenewold, and Willem K Kegel. Colloidal molecules with well-controlled bond angles. *Soft Matter*, 5(20):3823–3826, 2009.

[136] Andrea J Liu and Sidney R Nagel. Nonlinear dynamics: Jamming is not just cool any more. *Nature*, 396(6706):21–22, 1998.

[137] PG De Gennes and PA Pincus. Pair correlations in a ferromagnetic colloid. *Phys. kondens. Materie*, 11(3):189–198, 1970.

[138] Tamás Rudas. *Handbook of probability: theory and applications.* Sage Publications, 2008.

[139] Eric M Furst and Alice P Gast. Micromechanics of dipolar chains using optical tweezers. *Physical Review Letters*, 82(20):4130, 1999.

[140] John Frank Charles Kingman. *Poisson processes*, volume 3. Clarendon Press, 1992.

[141] A. Papoulis and S.Unnikrishna Pillai. *Probability, Random Variables and Stochastic Processes. Fourth Edition.* McGraw Hill, Boston, 2002.

[142] Joe W Tavacoli, Pierre Bauër, Marc Fermigier, Denis Bartolo, Julien Heuvingh, and Olivia du Roure. The fabrication and directed self-assembly of micron-sized superparamagnetic non-spherical particles. *Soft Matter*, 9(38):9103–9110, 2013.

[143] Colin P Reynolds, Kira E Klop, François A Lavergne, Sarah M Morrow, Dirk G. A. L. Aarts, and Roel P. A. Dullens. Deterministic aggregation kinetics of superparamagnetic colloidal particles. *J. Chem. Phys.*, 143(21):214903, 2015.

[144] Z Mimouni and JAD Wattis. Similarity solution of coagulation equation with an inverse kernel. *Physica A: Statistical Mechanics and its Applications*, 388(7):1067–1073, 2009.

[145] Sonia Melle, Gerald G Fuller, and Miguel A Rubio. Structure and dynamics of magnetorheological fluids in rotating magnetic fields. *Physical Review E*, 61(4):4111, 2000.

[146] Rebecca W Perry, Miranda C Holmes-Cerfon, Michael P Brenner, and Vinothan N Manoharan. Two-dimensional clusters of colloidal spheres: Ground states, excited states, and structural rearrangements. *Physical review letters*, 114(22):228301, 2015.

[147] Weijia Wen, DW Zheng, and KN Tu. Chain/column evolution and corresponding electrorheological effect. *Journal of applied physics*, 85(1):530–533, 1999.

[148] M Mohebi, N Jamasbi, and Jing Liu. Simulation of the formation of nonequilibrium structures in magnetorheological fluids subject to an external magnetic field. *Physical Review E*, 54(5):5407, 1996.

[149] A Yu Zubarev and VO Kostenko. On the theory of structuring magnetic suspensions. *Colloid Journal*, 75(1):66–72, 2013.

[150] Denis Wirtz and Marc Fermigier. Periodic structures and substructures in magnetic suspensions. *Langmuir*, 11(2):398–400, 1995.

[151] James E Martin, Robert A Anderson, and Chris P Tigges. Thermal coarsening of uniaxial and biaxial field-structured composites. *The Journal of Chemical Physics*, 110(10):4854–4866, 1999.

[152] Junaid M Laskar, John Philip, and Baldev Raj. Experimental evidence for reversible zippering of chains in magnetic nanofluids under external magnetic fields. *Physical Review E*, 80(4):041401, 2009.

[153] Jaime Rodríguez-López, Pedro Castro, Luis Elvira, and Francisco Montero de Espinosa. Study of the effect of particle volume fraction on the microstructure of magnetorheological fluids using ultrasound: transition between the strong-link to the weak-link regimes. *Ultrasonics*, 61:10–14, 2015.

[154] Kinnari Parekh, Jaykumar Patel, and RV Upadhyay. Ultrasonic propagation: A technique to reveal field induced structures in magnetic nanofluids. *Ultrasonics*, 60:126–132, 2015.

[155] O Kallmes and H Corte. The structure of paper, i. the statistical geometry of an ideal two dimensional fiber network. *Tappi J*, 43(9):737–752, 1960.

[156] CTJ Dodson and WW Sampson. The effect of paper formation and grammage on its pore size distribution. *Journal of Pulp and Paper Science*, 22(5):J165, 1996.

[157] Rune Holmstad. Methods for paper structure characterisation by means of image analysis. 2004.

[158] W. W. Sampson. *Modelling Stochastic Fibrous Materials with Mathematica*. Springer-Verlag, 2009.

[159] Delwyn G Fredlund and Anqing Xing. Equations for the soil-water characteristic curve. *Canadian Geotechnical Journal*, 31(4):521–532, 1994.

[160] W Brent Lindquist, Arun Venkatarangan, John Dunsmuir, and Teng-fong Wong. Pore and throat size distributions measured from synchrotron x-ray tomographic images of fontainebleau sandstones. *Journal of Geophysical Research: Solid Earth*, 105(B9):21509–21527, 2000.

[161] Jaime Castro and Martin Ostoja-Starzewski. Particle sieving in a random fiber network. *Applied Mathematical Modelling*, 24(8):523–534, 2000.

[162] R Ev Miles. Random polygons determined by random lines in a plane. *Proceedings of the National Academy of Sciences*, 52(4):901–907, 1964.

[163] Olga Markova, Jonathan Alberts, Edwin Munro, and Pierre-François Lenne. Bond flexibility and low valence promote finite clusters of self-aggregating particles. *Physical Review Letters*, 109(7):078101, 2012.

[164] Matthew A Lohr, Tim Still, Raman Ganti, Matthew D Gratale, Zoey S Davidson, Kevin B Aptowicz, Carl P Goodrich, Daniel M Sussman, and AG Yodh. Vibrational and structural signatures of the crossover between dense glassy and sparse gel-like attractive colloidal packings. *Physical Review E*, 90(6):062305, 2014.

[165] Jun Dong Park, Kyung Hyun Ahn, and Seung Jong Lee. Structural change and dynamics of colloidal gels under oscillatory shear flow. *Soft Matter*, 11(48):9262–9272, 2015.

[166] Jonathan K Whitmer and Erik Luijten. Influence of hydrodynamics on cluster formation in colloid- polymer mixtures. *The Journal of Physical Chemistry B*, 115(22):7294–7300, 2011.

[167] AD Dinsmore and DA Weitz. Direct imaging of three-dimensional structure and topology of colloidal gels. *Journal of Physics: Condensed Matter*, 14(33):7581, 2002.

List of publications

To date the following publications based on work in this thesis have been submitted or are in preparation

Colin P Reynolds, Kira E Klop, François A Lavergne, Sarah M Morrow, Dirk G. A. L. Aarts, and Roel P. A. Dullens. *Deterministic aggregation kinetics of superparamagnetic colloidal particles.* J. Chem. Phys., 143(21):214903, 2015.

Colin P. Reynolds, David Robinson, Dirk G.A.L. Aarts, Mark Wilson, William W. Sampson and Roel P.A. Dullens. *Coordination number statistics of cluster formation*, Submitted (chapter 4)

Colin P. Reynolds, Michael P. N. Juniper, William W. Sampson, Dirk G.A.L. Aarts and Roel P.A. Dullens. *Structural properties of two dimensional magnetorheological networks*, in preparation (chapter 5)

Colin P. Reynolds, William W. Sampson, Dirk G.A.L. Aarts and Roel P.A. Dullens. *Dynamics of two dimensional magnetorheological networks*, in preparation (chapter 5)

Colin P. Reynolds, William W. Sampson, Dirk G.A.L. Aarts and Roel P.A. Dullens. *Coordination number statistics of network formation*, in preparation (chapter 6)

Acknowledgments

I will always owe a great deal to Roel and Dirk, and to all of those who I have worked with in the Aarts-Dullens group since I started here as a masters student nearly 5 years ago. You cannot spend this length of time in the company of such good, decent and talented people and not be touched by it. The words on this page will not do justice to the immense gratitude I feel towards the people who make this group what it is.

Roel. Thank you! For your patience as I tried to find my way as a researcher, your understanding when I struggled, and your honesty throughout, I will always be grateful.

Dirk too, thank you. I'll miss the Mathematica tasks, challenging discussions and the games of squash. You have kept me on track and stopped me from over complicating things.

Bill, I've enjoyed throwing ideas around with you. The meetings we have had here in Oxford and up in Manchester have been some of the most productive.

A special mention has to go to Michael Juniper, who introduced me to magnetic particles and showed me the way in the beginning, and to David Robinson, contemporary and colleague.

Raam, you have been a true friend. You have made the last years some of the best I've had and you know I'll miss them when I'm gone. Arran, thank you for the coffee, bike chat and friendship. François for the rowing chat and company in the final days. Kazem for legitimising more coffee. Mike M for all the lunches, and yes, more coffee. Josh for the cricket chat, rowing chat, banter and support (come on son!!!). Yanyan, Yongxiang and Bo for completing 10-07. And to everyone else: Postdocs of now and then; PhDs young and old; and Part iis past and present, thank you.

Finally I would like to thank my family, friends, and dance partner. I would be lost without you.